# ACCELERATING THE PRINTABILITY OF NEW METAL ADDITIVE MANUFACTURING ALLOYS: A ROBUST CALIBRATION APPROACH

A Thesis

by

BING ZHANG

Submitted to the Office of Graduate and Professional Studies of
Texas A&M University
in partial fulfillment of the requirements for the degree of

DOCTOR OF PHILOSOPHY

| | |
|---|---|
| Chair of Committee, | Alaa Elwany |
| Committee Members, | Huiyan Sang |
| | Ibrahim Karaman |
| | Zhijian Pei |
| Head of Department, | Lewis Ntaimo |

August 2021

Major Subject: Industrial Engineering

# ABSTRACT

Metal additive manufacturing (AM) or metal three-dimensional (3D) printing offers significant benefits for manufacturing parts with features and capabilities that conventional techniques cannot match. Meanwhile, it is widely accepted that metal AM processes come with their own challenges. Metal AM typically suffers from high degrees of variability in the properties of the fabricated parts and high complexity in the fabrication process, particularly due to the lack of understanding and control over the physical mechanisms during fabrication. Simulation models for AM are essential to enable process planning and accelerate qualification and certification of fabricated parts. One important task involves calibrating simulation models to ensure that predictions are in agreement with experimental observations.

Part of my dissertation works on integrating Bayesian model calibration to accelerate the development of metal AM processes such as Laser Powder Bed Fusion (LPBF). A framework is developed includes experimental design, multiscale modeling and simulation, uncertainty quantification, and experimental material characterization for fully characterizing parameter-process-property relations in LPBF for materials design, process standardization, part qualification, and discovery/innovation.

Other parts of this dissertation focus on statistical calibration of a computer simulation model with multiple outputs where experimental observations for one (or more) of the outputs are expensive to acquire. Bayesian multiple imputation method is used in a statistical calibration framework to help estimate calibration parameters in the case of lacking expensive experimental data. The proposed methodology is properly analyzed and validated by an analytical simulation model of melt pool geometry in LPBF process. The insights and understanding achieved by applying these methods advance the development of AM processes.

# DEDICATION

To my parents, for everything they have done and still do for me.

To my daughter, my little princess, mom loves you forever.

# ACKNOWLEDGMENTS

First and most importantly, I want to thank and express my sincere appreciation to my advisor Dr. Alaa Elwany for all his guidance, support, advice, encouragement, professionalism and patience. Thanks for supervising me in my professional career and personal growth.

Second, I want to thank my committee members: Dr. Ibrahim Karaman, Dr. Huiyan Sang and Dr. Zhijian Pei, as well as Dr. Raymundo Arroyave, for their continued suggestions that made possible reaching the objectives of this dissertation.

I would like to thank all my excellent and intelligent colleagues, Dr. Gustavo Tapia, Dr. Mohamad Mahmoudi, David Shoukr, Chen Zhang, Raiyan Seede, Jiahui Ye, Lei Xue and Jacob Mingear for always working extremely hard, while at the same time making work more enjoyable and motivating.

I want to also thank all my very good friends at Texas A&M. I would have not been able to achieve this without you all and the good moments that we had.

Finally, I want to thank my parents and husband for their endless love, support and motivation throughout my PhD study and my life.

CONTRIBUTORS AND FUNDING SOURCES

## Contributors

This work was supervised by a dissertation committee consisting of committee chair, Professor Alaa Elwany of the Department of Industrial and Systems Engineering, and committee members, Professor Ibrahim Karaman of the Department of Materials Science and Engineering, Professor Huiyan Sang of the Department of Statistics and Professor Zhijian Pei of the Department of Industrial and Systems Engineering.

Section 2 of this dissertation was conducted in collaboration with Professor Darren Hartl, Jacob Mingear of the Department of Materials Science and Engineering.

Section 3.24, 3.26, 3.27, 3.3 and 3.4 of this dissertation were conducted in collaboration with Professor Ibrahim Karaman, Dr. Kadri C. Atli, Raiyan Seede, Lei Xue, Austin Whitt of the Department of Materials Science and Engineering and David Shoukr, Chen Zhang of the Department of Industrial and Systems Engineering.

Portions of this dissertation were conducted with the advanced computing resources and consultation provided by Texas A&M High Performance Research Computing.

All other work conducted for the dissertation was completed by the student independently.

## Funding Sources

Portions of this dissertation were supported by National Science Foundation under Grant number No.1846676. Portions of this dissertation were supported by Army Research Office (ARO) under Grant number No. W911NF-18-1-0278.

The contents of this dissertation are solely the responsibility of the authors and do not necessarily represent the official views of Texas A&M University, National Science Foundation (NSF) or Army Research Office (ARO).

# NOMENCLATURE

| | |
|---|---|
| A | Absorptivity of material [dimensionless between 0-1] |
| AM | Additive manufacturing |
| ANOVA | Analysis of variance |
| c | Thermal conductivity [W/(m·K)] |
| $\chi$ | Input domain of interest or study region |
| cov[$\cdot;\cdot$] | Covariance Operator |
| D | Melt pool depth [$\mu$m] |
| D4 | Laser beam size at 4 standard deviations |
| $\mathbb{E}[\cdot]$ | Expectation Operator |
| EDM | Wire Electrical Discharging Machining |
| FEM | Finite Element Method |
| $\Gamma(\cdot)$ | Gamma Function |
| GP | Gaussian Process |
| gPCE | Generalized Polynomial Chaos Expansions |
| GPRM | Gaussian process regression model |
| h | Hatch spacing [$\mu$m] |
| HGPM | Hierarchical Gaussian process model |
| ICME | Integrated Computational Materials Engineering |
| k | Specific heat capacity [J/(kg·K)] |
| K | Kernel function |
| LED | Linear Energy Density [J/mm] |
| LOO | Leave-One-Out Cross Validation |

| | |
|---|---|
| LPBF | Laser powder bed fusion |
| MAE | Mean Absolute Error |
| MAPE | Mean Absolute Percentage Error |
| MARS | Multivariate Adaptive Regression Splines |
| MCMC | Markov Chain Monte Carlo |
| MLE | Maximum likelihood estimation |
| NiNb | Nickel niobium alloy |
| NiTi | Nickel titanium alloy |
| P | Laser power [W] |
| pdf | Probability Distribution Function |
| PSD | Particle Size Distribution |
| QoI | Quantity of Interests |
| $\rho$ | Bulk density [kg/m3] |
| RMSE | Root Mean Squared Error |
| SEM | Scanning Electron Microscopy |
| SMA | Shape-Memory alloy |
| t | Layer thickness [$\mu$m] |
| $T_b$ | Boiling temperature [K] |
| $T_m$ | Melting temperature [K] |
| UQ | Uncertainty Quantification |
| V | Scan speed [m/s] |
| VED | Volumetric energy density [$J/mm^3$] |
| W | Melt pool width [$\mu$m] |
| $\boldsymbol{x}$ | Input vector to the process |
| $\boldsymbol{X}$ | Input data matrix |

| | |
|---|---|
| $x_i$ | ith input to the process |
| Y | Output or QoI of the process |
| $\boldsymbol{Y}$ | Output data vector |
| $\boldsymbol{Y}^P$ | Output prediction |
| $\boldsymbol{Y}^E$ | Output experimental data |
| $y^D$ | Melt pool depth data |
| $y^W$ | Melt pool width data |

TABLE OF CONTENTS

Page

LIST OF FIGURES

FIGURE Page

LIST OF TABLES

TABLE Page

# 1. INTRODUCTION

## 1.1 Additive Manufacturing (AM)

Additive Manufacturing (AM) technologies have already been shown to be of significant relevance to industry since the late 1990s [1, 2]. With the capability of producing direct end-use parts, AM technologies have been well applied across many industries including the aerospace, biomedical, defense, and automotive industries among many others [3, 4, 5]. These industries leverage the attractive capabilities of AM, such as the ability to fabricate parts with complex geometries, the consolidation of multiple parts that would need to be integrated in complex assembly processes into monolithic components, as well as the customization of the designs in order to meet very specific engineering requirements. Laser Powder Bed Fusion (LPBF), as a common AM technology, has attracted great attention with the objective to control and reduce the defects of fabrication [6].

### 1.1.1 Laser Powder Bed Fusion (LPBF)

LPBF process employs a high energy laser beam to selectively fuse fine metallic powder particles in a layer-by-layer fashion [7]. Within each layer, the desired shape is selectively melted by a laser that traces parallel linear paths. This process is repeated over and over again until the entire part has been fused together. LPBF process involves heat transfer, evaporation, melting and solidification, re-melting and re-solidification, shrinkage and other thermophysical behaviors upon successive passes of the laser beam within the same layer or across successive layers.

The complicated LPBF process is the root cause of many technical challenges that have negative impacts on its progress and adoption in mainstream industrial manufacturing. They are mainly printability and quality, indeed, are the microstructural and mechanical properties of fabricated parts. To achieve better understanding of processing parameter-property relationships, careful characterization of parts under various printing settings are necessary [8].

### 1.1.2 Printability

In particular, the challenges are resulted by defects like porosity, residual stress, micro-cracks, etc, due to the very high thermal gradients and cooling rates [9]. In turn, these defects distress the mechanical properties of the end parts making them unsuitable for several industrial applications. Furthermore, the LPBF process involves more than 40 processing parameters, and each of them has direct or indirect impact on the printability, quality and performance attained by the as-printed parts [10, 11].

#### *1.1.2.1 Defects*

Despite significant technological advances, the defect ratios are still high in LPBF process with respect to conventional manufacturing systems.

Porosity is particularly critical for most metal AM applications because it strongly impacts the fatigue performances and the crack growth characteristics of the part [12]. There are three main phenomena that result in porosity; namely lack of fusion, keyholing, and balling. Lack of fusion can occur when the melt pool depth is smaller than powder layer thickness due to an insufficient amount of laser energy being deposited into the powder bed. The lack of fusion boundary line then can be plotted as the line passing through laser power-scan speed combinations that result in a melt pool depth that is equal to the layer thickness. Large laser energy density can lead to the development of vapor cavities resulting from the recoil pressure associated with the rapid evaporation of the molten liquid. This enables the laser beam to "drill" into the material to a larger depth than is the case during the general conduction mode. This can ultimately result in the collapse of the cavity, leaving voids known as keyholing porosity [13]. The balling effect is observed at high laser power and scan speed combinations as the melt pool form into droplets (as opposed to a continuous weld track) due to Plateau-Rayleigh capillary instability [14].

Residual stresses in LPBF have been pointed out to arise from two different mechanisms, including the thermal gradient mechanism and the cool-down phase of molten top layers [15]. As a consequence of a stress relief through fracturing when the tensile stress exceeds the ultimate ten-

sile strength of the solid material at a given point and temperature, cracking phenomena occur [16]. Delamination is a particular case of cracking, where cracks originate and propagate between adjacent layers (inter-layer cracking). When the residual stresses exceed the binding ability between the top layer and the previous one, delamination occurs [17].

The LPBF fabricated parts may exhibit different kinds of dimensional and geometric deviations from the original CAD models [18, 19]. Regarding the size of the part, shrinkage and oversizing have been reported. Warping and elevated edges are the other types of geometrical distortion. This defect strongly impacts the quality and stability of the process for different reasons [20]. First, it deteriorates the surface topology and the dimensional accuracy of the part. Second, it may worsen the stair-stepping effect due to the layer level production. Third, when elevated edges protrude from the powder layer, they may interfere with the recoating system, increasing its wear and negatively affecting the consequent powder bed uniformity.

In LPBF processes, surface roughness has two contributors, i.e. the stair-stepping effect due to the layer-wise production, and some critical features like thin walls, overhang surfaces and acute corners. The surface finishing depends on the surface orientation with respect to the growth direction. In particular, downward- and up-ward surfaces are known to have considerably different roughness properties [21]. In those regions, the melt pool is largely surrounded by loose powder, which has a lower conductivity of the solid material. The diminished heat flux yields local overheating phenomena that may deteriorate the geometric accuracy.

#### *1.1.2.2 New Materials and Alloys*

Despite the notable growth and potential, it is widely accepted that metal AM technologies come with their own challenges such as lack of standards, time and cost intensive qualification and certification processes, and susceptibility to defects that compromise part performance. Some of these challenges are attributed to the fact that most (if not all) of existing commercial raw materials used in AM were originally developed for other manufacturing processes such as casting, forging, and machining. When attempting to process these materials using AM, they undergo different–and typically more complex–physical transformations resulting in defects, microstructural inconsisten-

cies, and high degrees of variability. Most AM researchers and practitioners have recently come to the realization that new materials and alloys need to be developed specifically for AM, with these complex physical phenomena in mind.

Developing new alloys for AM involves yet another set of challenges, the most obvious of which is the fact that there is no systematic procedure to determine the processing recipes (or parameters) for these new materials [22, 23]. One possible approach is through brute force, exhaustive, exploration of the entire parameter space [24, 25]. Such an approach is inefficient when considering the associated materials, fabrication, and characterization costs. Another slightly improved approach is to utilize tools of statistical design of experiments such as factorial design, fractional factorial design, or Taguchi-based designs [26, 27, 28]. These approaches are well-studied and may give acceptable results. However, they still require sufficiently large numbers of experiments (although less than brute force trial and error). Furthermore, they are specific to certain experimental conditions such as the type of AM commercial system or properties of the raw feedstock. When one factor changes, entirely new sets of experiments must be conducted leading to higher experimental costs. A third approach sometimes followed by AM practitioners is to start with the processing parameters that have been successfully used to process a similar class of materials [29, 30]. For example, a newly designed binary nickel niobium (NiNb) alloy may be tested starting with the processing parameters for nickel-based superalloys such as Inconel 718 or Inconel 625 [31, 32]. These starting sets of processing parameters are then adjusted through trial and error until the material can be successfully printed (i.e., with little to no porosity, and showing desirable mechanical properties) [11]. However, there is no guarantee that processing parameters that work for a specific material system will necessarily work for a new material system just because they share some compositional similarities.

Some more elaborate model-based approaches resort to computational models, such as finite element models (FEM) or integrated computational materials engineering (ICME) models in general [33]. Statistical design of experiments is usually utilized in the model-based approaches to make an experimental plan for reducing experimental burden [34]. The benefit of these approaches is the

fact that the models used are based on first principles and are thus, in theory, material-and system-agnostic. However, in reality ICME models need to be tuned and calibrated in order to ensure that their predictions agree with experimental observations, depending on the material being processed or the AM platform being employed. Despite notable recent advances in developing ICME models for AM, there is still much work to be done towards developing models with improved fidelity. Even if we assume that these models already exist and are mature enough, there are no clear guidelines on how to use them to determine processing recipes for new materials. Finally, most of these models are computationally expensive, making them more suitable for understanding process physics than conduct process optimization. They also typically require access to proprietary code that might not be readily available for all AM practitioners.

### 1.1.3 Quality Consistency

In LPBF AM process, from powder bed forming to melting and solidification, various sources of uncertainty are involved in the processes. These sources of uncertainty result in variability in the quality of the manufactured component. The quality variation hinders consistent manufacturing of products with guaranteed high quality. This becomes a major hurdle for the wide application of AM techniques, especially in the manufacturing of metal components. This large microstructure and mechanical property variability in print is one of the predominant barriers to widespread adoption of additively manufactured structural components.

Although, in some cases, post-processing techniques are suitable to mitigate or remove defects from LPBF fabricated parts (e.g. hipping) as well as maintain the same quality level, improving the quality of the as-built parts is fundamental to meet stringent and challenging industrial requirements. Processing parameter optimization, model-based variability and uncertainty analysis are applied to control and improve the quality of LPBF as-built parts while planning and conducting the fabrication process.

### 1.1.4 Process Standardization and Optimization

Most experts agree that the lack of AM standards is a key issue that must be taken into account when barriers to the broad adoption of AM are considered. In relation to this, the existing standards are not suitable for AM. Several factors strongly influence the limited applicability of conventional standards to AM. For example, the layered approach to the additive manufacturing of parts may cause directional dependence in the material properties of that part. Several research studies have reported different mechanical properties when the part is made in the X–Y direction compared to the Z direction. In LPBF, the processing parameters (laser power, scan speed, hatch spacing, layer thickness, etc.) have been shown to influence microstructural and mechanical properties [8]. The interaction effects between processing parameters are more dominant than individual effects. Even the oxygen level while laser sintering, the amount of recycled powder used in printing and the recycled time were observed to have a strong influence on the final dimensions and properties of the part [35, 36, 37]. Further more, two manufacturers of AM parts supplying the same product to final users, even using the same equipment and material, could supply parts with different characteristics, either in terms of mechanical properties or geometric tolerances and roughness.

Therefore, developing processes to increase certification of AM is needed. A protocol that can steamline the development, application, and optimization of any metal alloys in LPBF is urgently required.

## 1.2 Computational and Analytical Methods in AM

### 1.2.1 Computer Models for AM

It is crucial to develop better understanding of the physics mechanisms that drive the thermal history within the part during LPBF processes. In reality, experimental measurement of the thermal field in LPBF is extremely difficult due to a number of challenges such as very high thermal gradients and cooling rates, micro-scale melt pool size, and emissivity variations, among many other challenges. In-situ monitoring can be an approach to capture thermal information while laser sintering [38, 39]. However, the in-situ sensors for LPBF are complicated due to significantly high

noise factors. Nevertheless, the acquired sensors data have to be post-processed before analyzing and predicting the quality of the part. Consequently, computer models are needed to complement experiments in understanding the thermal history of LPBF processes.

Improved model simulations have the capability of mimicking almost any kind of physical processes, saving hours and even days worth of manual calculations [40, 41]. The purpose of these simulations is to model the entire LPBF processes and predict outcomes by varying different processing parameters [42]. However, none of the models is perfect. The disagreement between the experimental results and the model outputs can be attributed to one or more of the following factors: (1) lack of understanding of the physics mechanism in LPBF processes, (2) unknown model parameters, (3) wrong input values for the model, (4) variability resulted by the random behavior of the system, and (5) uncertainties within numerical simulation algorithms [43, 44, 45]. Hence, it is necessary to identify, characterize, and quantify the uncertainties within models in order to strengthen the robustness of model performance. So that the models can be employed to guide the AM processing parameters selection and optimization.

### 1.2.2 The Purpose of Uncertainty Quantification (UQ) for AM

Like we mentioned above, the quality inconsistency is a major hurdle for the wide application of AM techniques, especially in LPBF. To achieve the quality control of the AM process, a good understanding of the uncertainty sources in each step of the AM process and their effects on product quality is needed [46]. Uncertainty quantification (UQ) is a process of investigating the effects of uncertainty sources (aleatory and epistemic) on the quantities of interest (QoIs) [47, 48]. Even though UQ for models of physical hardware has been intensively studied during the past decades and continue to address important research questions, UQ in AM is still at its early stage. Only a few examples have been reported in the AM literature which are mainly based on experiments and are performed at the process level [49, 43]. This will result in excessive material wastage, increased product development cost, and delay in the product development process because UQ usually requires numerous experiments and process optimization and UQ are implemented in a double loop framework (i.e., UQ needs to be performed repeatedly when the process is changed)

[50]. A generic UQ framework built upon the understanding of fundamental principles of the AM will significantly benefit the wider acceptance of the AM process and push the AM techniques for the manufacturing of metal products to the next stage. Systematic UQ of AM will also provide a solid foundation for the uncertainty management of the AM process, thus allowing effective allocation of limited resources to meet quality requirement and robustness targets.

The purpose of UQ is to investigate the effects of uncertainty sources on the variation of the QoIs. In AM, the modeling of model discrepancy and model parameter uncertainty is the major job in modeling of uncertainty sources. Model discrepancy or model form uncertainty comes from the assumptions and simplifications made in various simulation models. For example, the simplification of melting pool models by ignoring the heat radiation and evaporation, and the simplification of Marangoni forces in the finite element thermal model. The model discrepancy can be modeled as a surrogate model by comparing the difference between the simulation model and the experiment at different input settings. On the other hand, since some parameters are unknown due to the model parameter uncertainty and the model form uncertainty is a function of these model parameters, it is very difficult to accurately model these two sources of model uncertainty together. A widely used approach for dealing with this kind of problem is the employment of model calibration approach under the Kennedy and O'Hagan framework, the details of this framework are available in Ref. [51]. More recently, Tapia et al. conduct UQ for a physics-based precipitation model of nickel-titanium shape memory alloys through combining experimental and computer simulation data [52]. Mahmoudi et al. conduct UQ for a 3D finite element thermal model with multiple QoIs through linking the model to experimental observations via a computationally efficient surrogate modeling approach based on multivariate Gaussian processes [53].

### 1.3 Organization of the Dissertation

This dissertation is organized by the following four chapters. This work aims to fill the gaps outlined above, the quality optimization, printability, and AM certification. More specifically, the objective is to establish a unified framework to determine printability maps for a given newly developed material or alloy in LPBF metal AM processes by employing robust modeling and

calibration methods.

In chapter 2, we characterized and optimized the LPBF processing parameters of as-fabricated and electropolished Nitinol Titanium (NiTi) shape memory alloy (SMA) actuators with embedded channels for liquid metal forced fluid convection to increase actuator heat transfer rates. This work utilizes a design of experiments methodology by varying LPBF processing parameters on the as-fabricated surface roughness of the overhangs and walls of interior channels in NiTi. To enable post-process increases in surface quality, the channels are subjected to an electropolishing treatment and further characterized. Analysis of variance (ANOVA) and ain effects plots are utilized to identify the significance of each processing parameter and to further explore the optimal processing parameters.

Next, in chapter 3 we proposed an efficient framework for printability assessment of newly developed alloys or materials that have never been applied in LPBF. The most obvious challenge in fabricating these materials is the fact that there is no systematic procedure to determine the processing recipes (or parameters) for these new materials. An computationally tractable analytical model enhances the accelerated aspect of the proposed framework through a backward UQ step (also known as calibration). In addition the proposed framework guides the microstructural and mechanical characterization of specimens that are printed according to that map. We validate this proposed framework using three different material systems, two of which have not been previously investigated.

In chapter 4, we take the next step toward the printability framework and present methodologies for statistical calibration of a computer simulation model with multiple outputs where experimental observations for one (or more) of the outputs are expensive to acquire. On one hand, a hierarchical Gaussian process methodology is developed to make predictions of the missing outputs by leveraging their inherent correlation. Then the experimental observations together with the predicted data are applied into multivariate statistical calibration framework. On the other hand, bayesian multiple imputation method is directly used to estimate calibration parameters in the case of missing data.

The dissertation is concluded in Chapter 5 where a summary of implications, concluding remarks and potential future extensions are outlined.

# 2. PROCESS OPTIMIZATION ON THE SURFACE ROUGHNESS OF LPBF FABRICATED NiTi INTERIOR CHANNELS*

## 2.1 Background

Nickel Titanium (NiTi) which exhibits shape memory effect has been utilized in many applications, such as biomedical, automotive, aerospace and others. In aerospace, NiTi alloy actuator with embedded channels were designed for liquid metal forced fluid convection to increase actuator heat transfer rates. However, the fabrication of NiTi actuators with complex structures is challenging using traditional manufacturing technologies due to NiTi's difficulty of machining and sensitivity to temperature and composition. As the development of AM, LPBF as one of the popular AM processes has the capability of tailoring the functional response of NiTi, such as phase transformation temperatures, through controlling the manufacturing processing parameters, with minimal to no need for post-heat treatment. However the surface roughness of as-fabricated LPBF interior channel parts are directly influenced by L-PBF manufacturing processing parameters (that have been listed in the previous chapter) and the design of channel diameter, no prior studies have reported the effects of these parameters on interior surface roughness.

In this chapter, I present a work which is the first systematic study to understand the relationships between processing parameters, structure and the surface roughness of as-fabricated NiTi parts, with an application emphasis on interior channels. Second, this work presents one of the first effort on post-processing LPBF NiTi parts using electropolishing to improve surface quality and further establishes a relationship between processing parameters and electropolished surface roughness.

*Reprinted with permission from "Effect of process parameters and electropolishing on the surface roughness of interior channels in additively manufactured nickel-titanium shape memory alloy actuators" by Jacob Mingear, Bing Zhang, Darren Hartl, Alaa Elwany, 2019. Additive Manufacturing, Volume 27, Pages 565-575, Copyright [2019] by Elsevier.

## 2.2 Experimental Method

The interior channel parts were printed by ProX 100 commercial LPBF system by 3D Systems, where the maximum laser power is 50 W. The machine has a Gaussian profile fiber laser with wavelength $\lambda$ = 1070 nm and beam spot size of approximately 80 $\mu$m [54]. The maximum scan speed of our printer is 2.5 m/s. Fabrication was carried out under an inert argon atmosphere with oxygen level set to less than 500 parts per million (ppm). All parts were printed at constant layer thicknesses set equal to the 80th percentile of the powder size distribution ($d_{80}$).

The as-fabricated interior channel parts were subsequently cut from the build substrate using wire electrical discharge machining (EDM). All parts were sectioned along their channel axes using a slow speed diamond precision cutting wheel, exposing their internal surfaces for surface roughness measurements and imaging. Sectioning was needed for two reasons: (1) to enable measurement of surface roughness, and (2) to facilitate electropolishing. After sectioning, channels were sonicated in a 1:1 ethanol/acetone mixture to remove cutting fluid and remove any loose powder from their interior surfaces. The surface roughness was measured over an area of the exposed channels using a Zygo Zegage optical profilometer. Then, electropolishing was performed as a post-processing step based on a procedure by Pohl et al. [55] for NiTi alloys using an acetic/perchlorate acid electrolyte, as depicted in Figure 2.1. A nickel foil anode encompassed the interior of a beaker to ensure equal distance from the channels. The channel parts were adhesively bonded to a copper wire-embedded rubber stopper and acted as the cathode. The electropolishing step took 25 min at 10 V at room-temperature. After electropolishing the channel parts, the specimens were subsequently reevaluated for surface roughness measurement and imaging.

To enable further increases in performance, it is critical to characterize and control the surface quality of fully interior channels which have higher surface roughness compared to exterior top surfaces. A two-level $2^{5-1}$ fractional factorial design of experiments was employed to study the relationship between five LPBF processing parameters and the surface roughness of interior channels in as-fabricated NiTi. The processing parameters include: laser power 45 or 50 [W], scan speed 80 or 120 [mm/s], hatch space 35 or 120 [$\mu m$], scan pattern [rasting angle of $\pm 45^{\circ}$

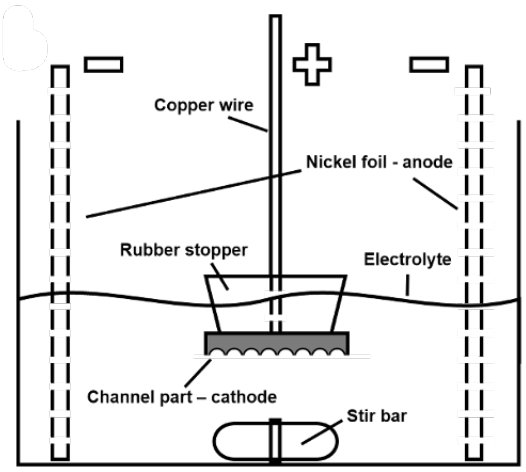


Figure 2.1: Schematic of the electropolishing experimental setup.

and $0°/90°$, displayed as Figure 2.2], and channel orientation [horizontal (H) or vertical (V)]. A L16 experimental design matrix for two levels (low and high) of each channel was developed, as shown in Table 3.4. Channels with horizontal and vertical build orientation are denoted by H1-H8 and V1-V8, respectively. Further, the design matrix was repeated independently to consider a total of three channel diameters 1, 1.5, and 2 [mm]. The fabrication process and as-fabricated channel samples are displayed in Figure 2.3. The experimental results of root-mean-square surface roughness, $S_q$ and profile skewness, $S_{sk}$ were analyzed by the analysis of variance (ANOVA) to elucidate the effects of the processing parameters on the channel surface roughness.

## 2.3 Results and Discussion

### 2.3.1 As-Fabricated Channel Analysis

A representative group of SEM micrographs of the as-fabricated channels decreasing in channel diameter is presented in Figure 2.4, with the top and bottom rows representing horizontal channel overhangs and vertical channel walls, respectively. Micrographs further detail that the surfaces of vertical channel walls are speckled with partially fused powder feedstock while the horizontal channel overhangs contain a similar appearance but with additional large stalactites.

Table 2.1: The L16 design of experiments matrix.

| Channel | Laser Power (W) | Scan Speed (mm/s) | Hatch Spacing ($\mu m$) | Scan Pattern | Channel Orientation |
|---|---|---|---|---|---|
| Low-level: | 45 | 80 | 35 | $\pm 45°$ | Horizontal (H) |
| High-level: | 50 | 120 | 120 | $0°/90°$ | Vertical(V) |
| H1 | 45 | 80 | 35 | $\pm 45°$ | Horizontal |
| H2 | 50 | 120 | 35 | $\pm 45°$ | Horizontal |
| H3 | 50 | 80 | 120 | $\pm 45°$ | Horizontal |
| H4 | 45 | 120 | 120 | $\pm 45°$ | Horizontal |
| H5 | 50 | 80 | 35 | $0°/90°$ | Horizontal |
| H6 | 45 | 120 | 35 | $0°/90°$ | Horizontal |
| H7 | 45 | 80 | 120 | $0°/90°$ | Horizontal |
| H8 | 50 | 120 | 120 | $0°/90°$ | Horizontal |
| V1 | 50 | 80 | 35 | $\pm 45°$ | Vertical |
| V2 | 45 | 120 | 35 | $\pm 45°$ | Vertical |
| V3 | 45 | 80 | 120 | $\pm 45°$ | Vertical |
| V4 | 50 | 120 | 120 | $\pm 45°$ | Vertical |
| V5 | 45 | 80 | 35 | $0°/90°$ | Vertical |
| V6 | 50 | 120 | 35 | $0°/90°$ | Vertical |
| V7 | 50 | 80 | 120 | $0°/90°$ | Vertical |
| V8 | 45 | 120 | 120 | $0°/90°$ | Vertical |

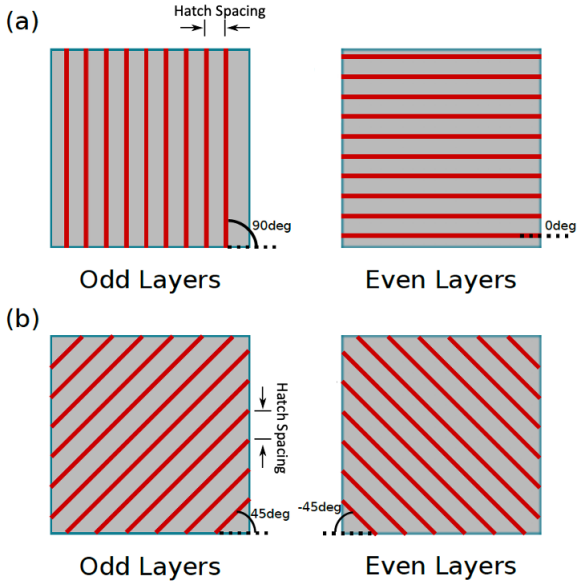


Figure 2.2: Graphical description of scanning strategy settings specified by the rastering angle relative to the build-plane coordinate axis for successive odd and even layers. (a) Rastering angle of 90° and 0°. (b) Rastering angle of 45° and -45°.

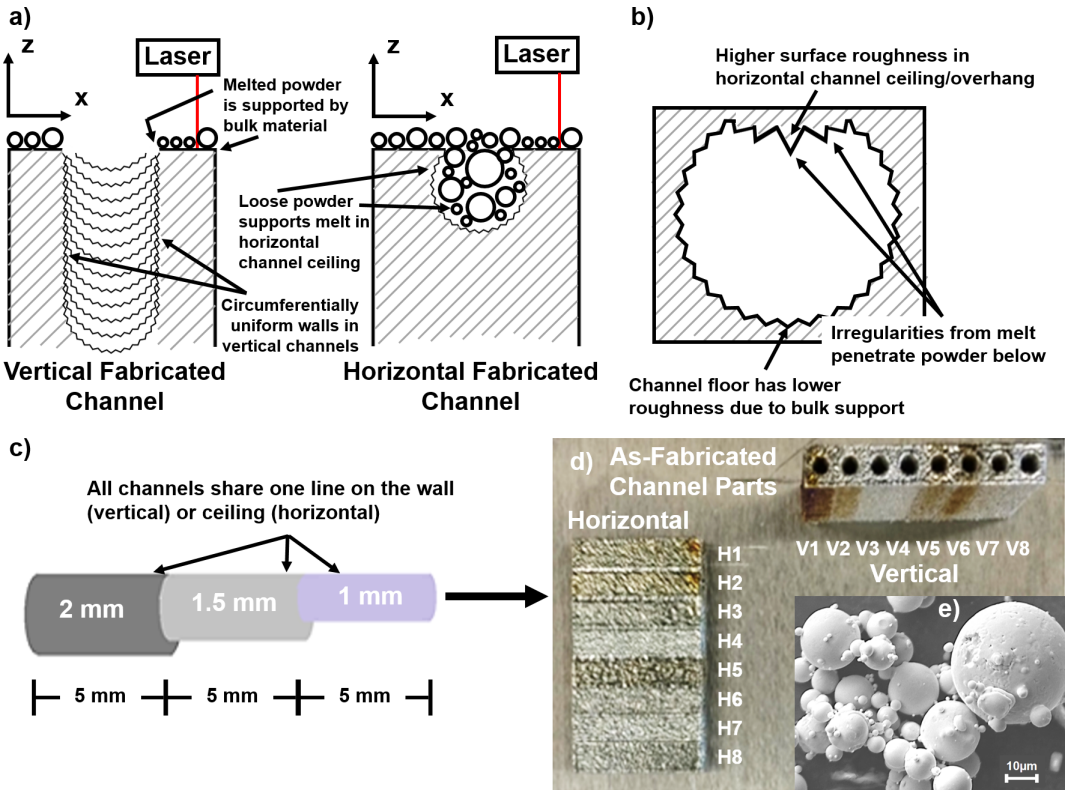


Figure 2.3: (a) Diagram depicting the layer-by-layer fabrication routes for horizontal and vertical channels; vertical channels build new layers upon a previously solidified layer while horizontal channels build ceilings upon powder beds; (b) Horizontal channel cross-section schematic depicting the result of a melt pool penetrating into porous powder during ceiling fabrication leading to higher roughness. (c) All three diameters in a given channel lie on a single line for facile measurement; channel diameters step every 5 mm. (d) Finished channel parts with their respective parameter sets (e) Scanning electron microscope (SEM) image of NiTi powder.

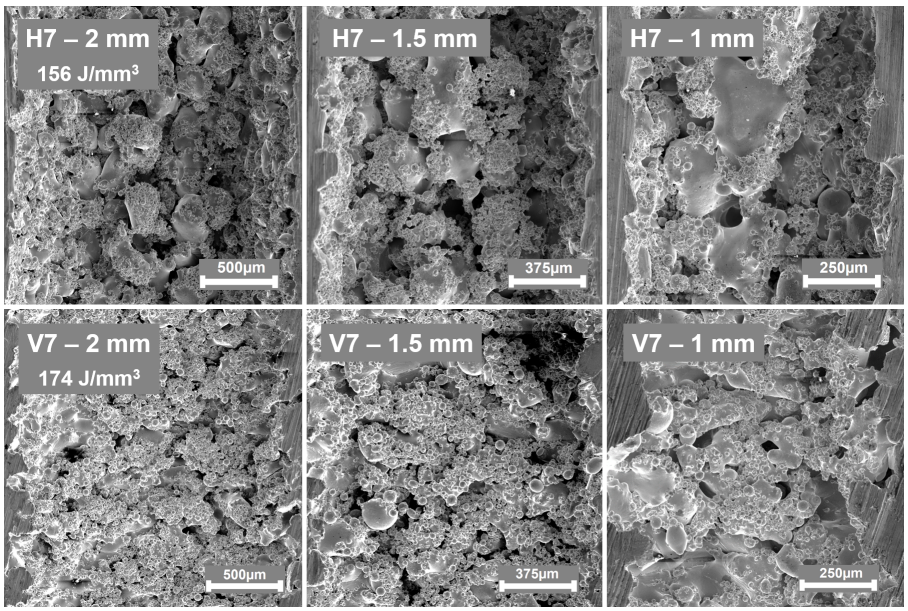


Figure 2.4: Representative SEM micrographs of the as-fabricated horizontal channel overhangs (top three images) and the vertical channel walls (bottom three images) over the three channel diameters. Both orientations contain partially fused powder feedstock on their surfaces. The stalactite structures on the overhangs are a prominent feature and increase surface roughness. The vertical channels are more circumferentially uniform.

Volumetric energy density (VED) in LPBF is a metric that combines laser power ($P$), scan speed ($V$), and hatch space ($h$), and layer thickness ($t$) through the following relationship:

$$\text{VED [J/mm}^3\text{]} = \frac{P}{Vht} \tag{2.1}$$

When comparing channels of the same size and ordering in terms of VED as shown in the SEM micrographs in Figure 2.5, qualitatively, there appears to be a trend regarding surface quality.

As a first observation, the higher VED channels seem to be more densely covered in partially fused powder feedstock than lower VED channels. Specifically in the horizontal channels, the size of the stalactites are also much larger at higher energy densities. In vertical channels, the underlying surface where the melt pool solidified for each layer is more easily observed as VED decreases (look for a fish scale-like morphology and notice the increase of the underlying melt surface from V5 to V8, including V7 from Figure 2.4, as VED decreases). The underlying surface is less notice-

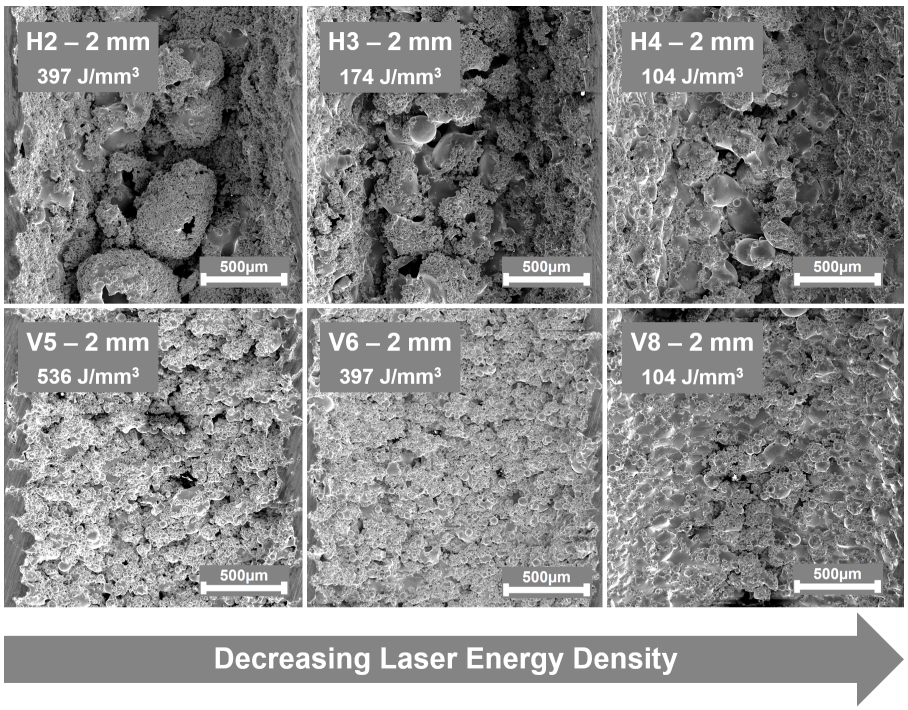


Figure 2.5: SEM micrographs displaying interior channel morphology with respect to VED. The lower VED channels have less partially fused powder feedstock on their respective surfaces. Further, for the horizontal channel overhangs, the size of the stalactite structures are smaller for lower VED.

able in the horizontal channels as the stalactites are the main feature. These observations are also seen in the smaller channel diameters, 1.5 mm and 1 mm, which are not displayed in Figure 2.5. A suitable physical explanation for such features may stem from increased VED leading to larger melt pools which consequently result in more melt pool runoff into adjacent non-melted powder feedstock creating larger stalactites and/or partially fusing to more powder feedstock. When compiling the quantitative $S_q$ data in regards to VED, however, this observation is not as obvious; more accurate profilometry techniques could better reveal such a trend.

Surface profile data was processed to produce p-values from ANOVA, shown in Table 2.2, to assist in clarifying which processing parameters are significant in determining as-fabricated $S_q$ and $S_{sk}$. A p-value of less than 0.05 is considered significant with 95% confidence. Thus, based on these calculations, it can be stated that channel orientation has the most significant effect on $S_q$. For $S_{sk}$, it can be suggested that scan pattern for only 1 mm channels play an important role compared

Table 2.2: p-values from ANOVA of as-fabricated channels corresponding to the main effect plots; bold-face denotes significance.

| Roughness | Channel Diameter | Laser Power (W) | Scan Speed (mm/s) | Hatch Spacing ($\mu m$) | Scan Pattern | Channel Orientation |
|---|---|---|---|---|---|---|
| $S_q$ | 2mm | 0.0909 | 0.0859 | 0.3313 | 0.5566 | **0.0002** |
| | 1.5mm | 0.5083 | 0.2792 | 0.4280 | 0.4309 | **0.0002** |
| | 1mm | 0.8381 | 0.7806 | 0.6255 | 0.3766 | **0.0062** |
| $S_{sk}$ | 2mm | 0.3910 | 0.3826 | 0.5348 | 0.3175 | 0.0816 |
| | 1.5mm | 0.7180 | 0.8280 | 0.5070 | 0.1170 | 0.2330 |
| | 1mm | 0.9189 | 0.3678 | 0.7056 | **0.0313** | 0.3072 |

to other factors.

The main effect plots of Figure 2.6 correspond to the ANOVA results by the high slopes associated with channel orientation for $S_q$, in addition to scan pattern for $S_{sk}$. Comparing horizontal channel walls against vertical channel overhangs, the mean of horizontal channel $S_q$ values are nearly twice that of the the mean of vertical channel $S_q$ values. The remaining parameters are overshadowed by the influence of channel orientation for $S_q$.

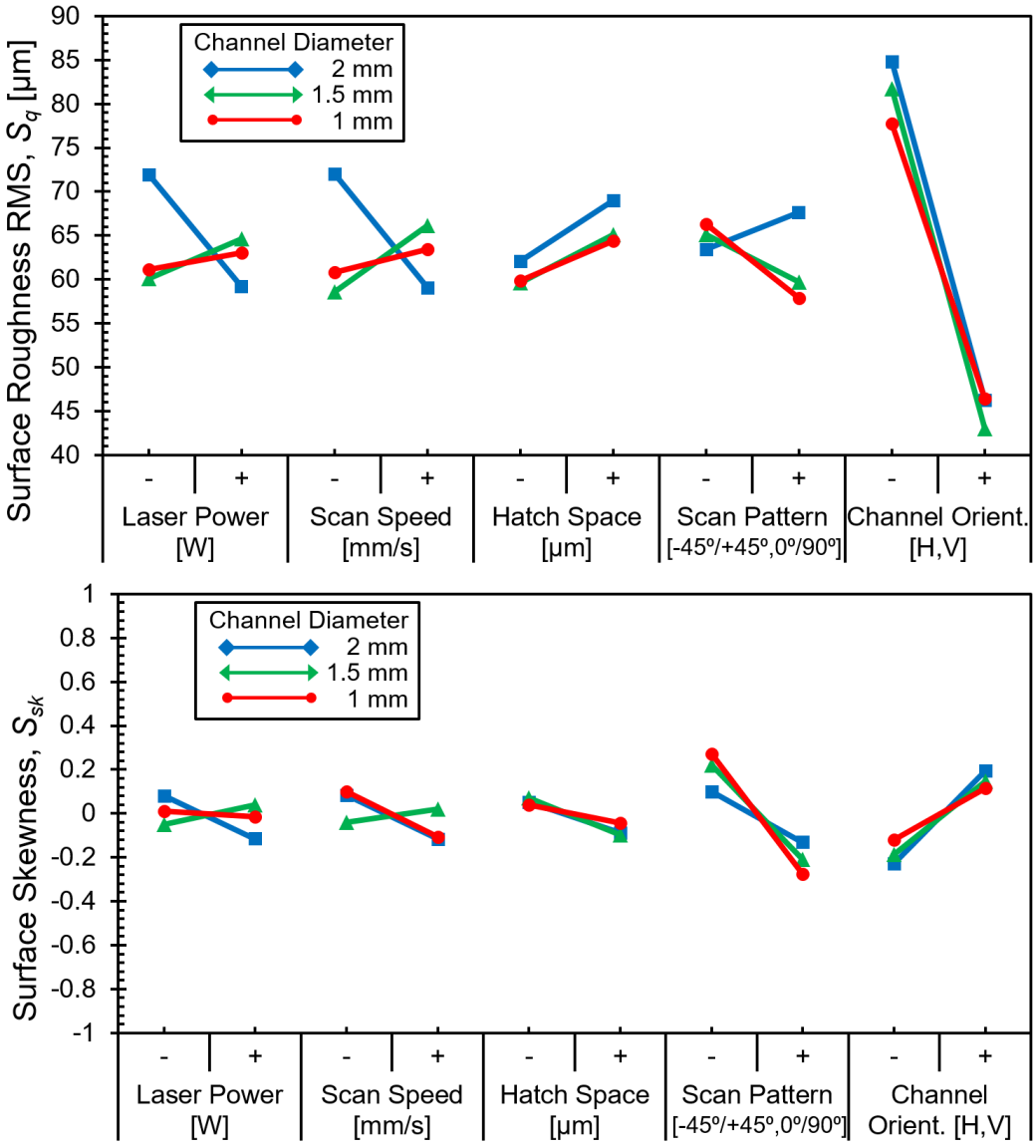


Figure 2.6: Main effects plots for as-fabricated channels showing the mean value of $S_q$ and $S_{sk}$ with each level and factor. Channel orientation dominates the resultant $S_q$, while only 1 mm channels are dependent on scan pattern for $S_{sk}$, based on the ANOVA results from Table 2.2.

The effect of channel orientation on surface roughness is consistent with expectations. Channel orientation is an important design consideration in AM. It is not uncommon to encounter a situation where flexibility in setting a specific channel orientation is not feasible. For example, a complex vascular part may inevitably require some channels to be fabricated in the horizontal orientation, or the layout of support structures in the part may necessitate building in a specific

orientation. Therefore, it is important to consider the surface of the channel ceiling will inevitably have high roughness, seemingly indifferent to other processing parameters when producing horizontally oriented channels.

### 2.3.2 Electropolished Channel Analysis

Electropolishing was performed as a post-processing step to improve surface roughness. Before electropolishing the samples, an initial experiment was conducted to quantify the mass loss of small features on as-fabricated surfaces. After 25 min of electropolishing, all pillars lost approximately 0.25 mm of material circumferentially. Thus, a consistent mass loss rate of approximately 0.01 mm/min occurred, regardless of processing parameters used; this does not necessarily suggest that each channel had the same reduction in surface roughness, however. In practice, this procedure would result in a 1.5 mm diameter channel losing enough material to become a 2 mm diameter channel, an important consideration when designing channels or similarly sized features.

As discussed before, the existence of a trend in the as-fabricated surface morphology with respect to laser energy density was observed qualitatively. It was suggested that this trend originated from higher energy densities producing more melt runoff which could create larger stalactites and/or partially fuse more non-melted adjacent powder located in the channel. This trend seems to persist after electropolishing. For both horizontal and vertical channels, an inverse correlation is observed between the effectiveness of electropolishing (reducing surface roughness) and laser energy density, as presented in Figure 2.7.

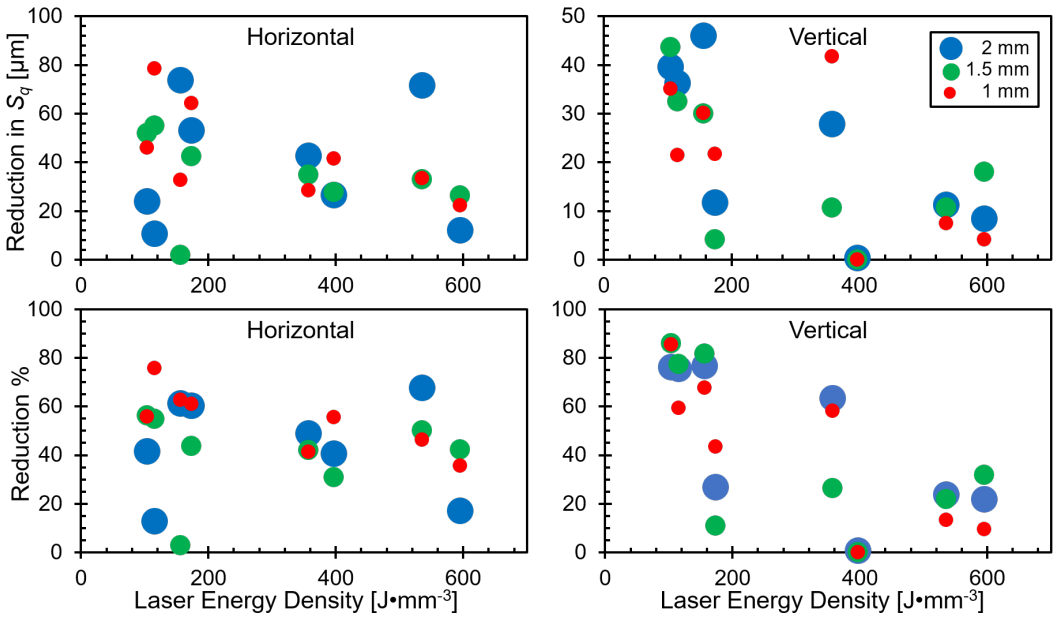


Figure 2.7: As VED decreases during fabrication, the reduction and reduction percentage of surface roughness from electropolishing step increases, displayed for horizontal and vertical channels.

SEM micrographs of the electropolished surfaces are shown in Figure 2.8. Channel H2 clearly has more remnant features after electropolishing than the lower energy density channel, H4; these features include the remnants of stalactites and fused powder boundaries. For the vertical channels, V6 presents many fused powder boundaries while V8 has a relatively clean surface finish. Optical profilometry data highlights such a distinction with V6 having over three times the $S_q$ value than V8. These observations are also found for channel diameters not displayed in Figure 2.8. It seems that more penetrating melt pools and partially fused particle interfaces, associated with high laser energy density, result in a less effective electropolish; a lower energy density would lead to less melt pool runoff into supporting powder and less partial fusion with powder.

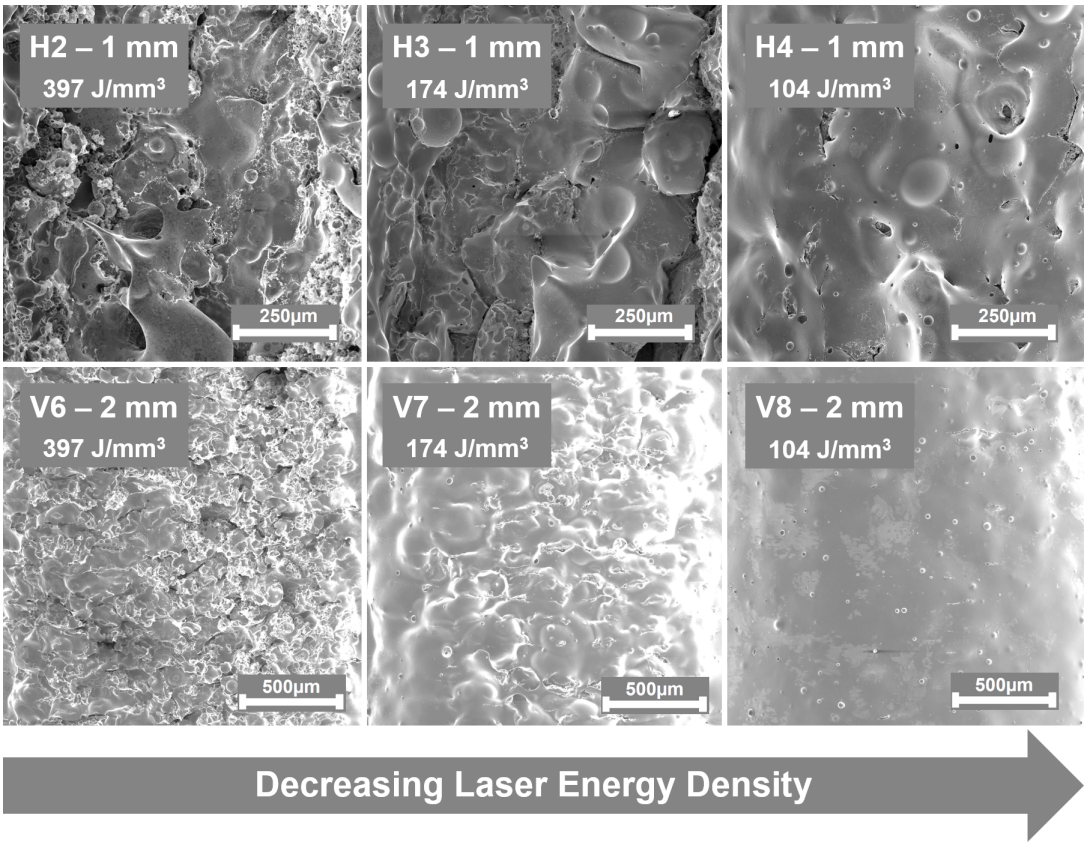


Figure 2.8: SEM micrographs displaying electropolished interior channel morphology with respect to energy density. The lower energy density channels have visibly smoother surface. There is a higher density of particle edge remnants from partially fused powder feedstock in the higher energy density channels. There are also some remnants of the stalactite structures in the electropolished horizontal channel overhangs.

Captured by the ANOVA p-value results and main effect plots in Table 2.3 and Figure 2.9, there appears to be multiple significant parameters in determining electropolished $S_q$, unlike the as-fabricated channels. For $S_q$, channel orientation remains the most significant parameter for 2 mm and 1.5 mm channels but not 1 mm channels; this further supports the notion that some factors become more or less impactful based on the channel size. Laser power and scan pattern are also significant for only 2 mm channels. Hatch space is significant for only 1 mm channels and the $35\mu m$ hatch space leads to higher roughness, a similar result for overhanging surfaces has beed observed [56]. This result could stem from lower hatch spacing corresponding to increased melt overlap interactions between laser scans. Ultimately, including the step of electropolishing

Table 2.3: p-values from ANOVA of electropolished channels corresponding to the main effect plots; bold-face denotes significance.

| Roughness | Channel Diameter | Laser Power (W) | Scan Speed (mm/s) | Hatch Spacing ($\mu m$) | Scan Pattern | Channel Orientation |
|---|---|---|---|---|---|---|
| $S_q$ | 2mm | **0.0400** | 0.5030 | 0.2521 | **0.0031** | **0.0003** |
| | 1.5mm | 0.2921 | 0.5714 | 0.3694 | 0.4659 | **0.0134** |
| | 1mm | 0.5530 | 0.1954 | **0.0076** | 0.9020 | 0.1348 |
| $S_{sk}$ | 2mm | 0.2230 | 0.1760 | 0.7670 | 0.7020 | 0.3020 |
| | 1.5mm | 0.1039 | 0.0644 | 0.1915 | **0.0251** | 0.5989 |
| | 1mm | 0.8245 | 0.2211 | 0.3794 | **0.0032** | 0.5393 |

provides a method to control $S_q$ by decisively altering LPBF processing parameters rather than being confined by the design constraint, channel orientation, in as-fabricated channels.

For $S_{sk}$, the tendency of channels to be dominated by troughs or peaks is dependent on scan pattern; the 45°/ -45° leads to peaks while the 90° and 0° leads to troughs. The main effects plot of Figure 2.9 also indicate that, on average, 1 mm channels remain strictly dominated by troughs after electropolishing.

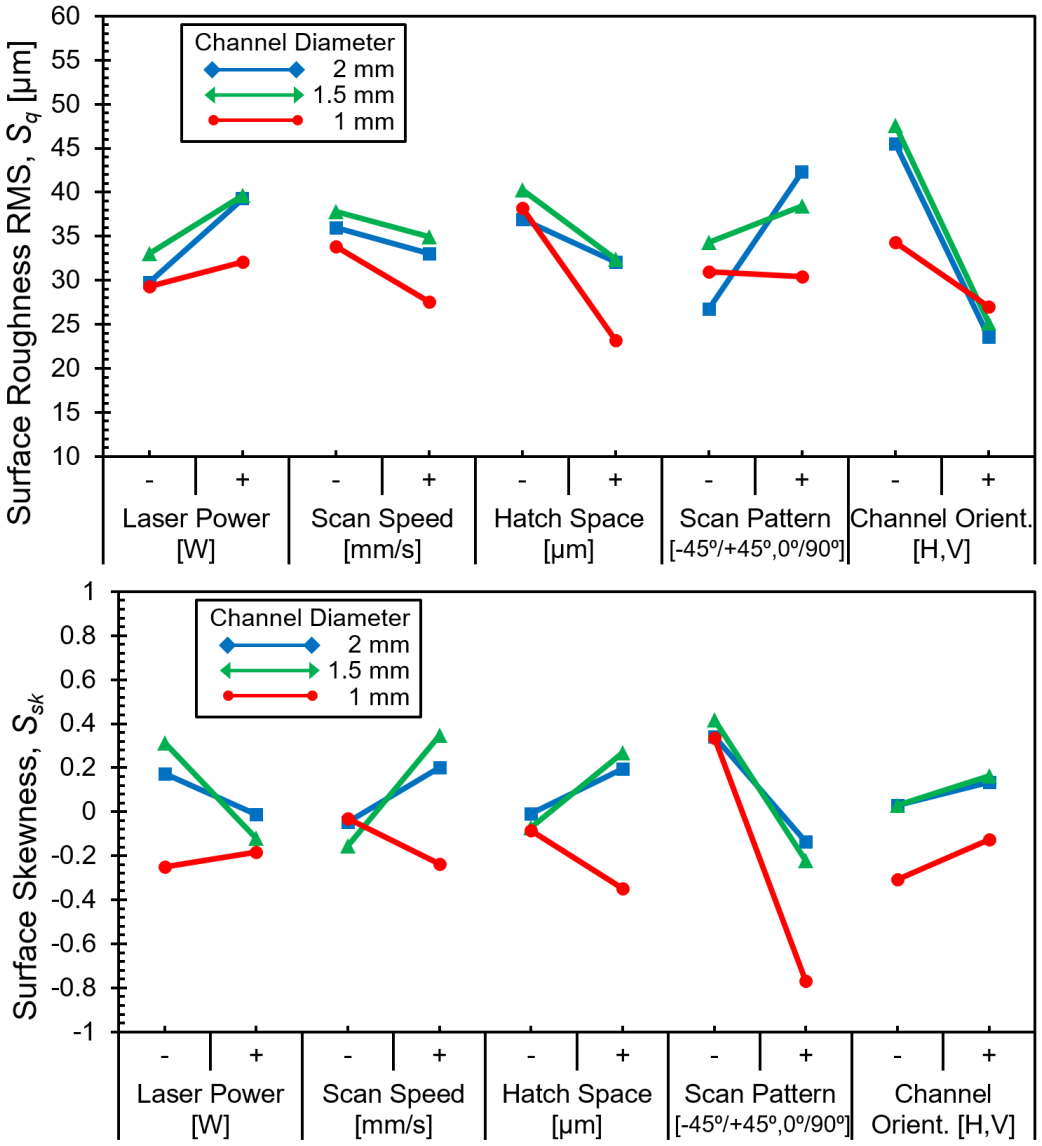


Figure 2.9: Main effects plots for electropolished channels showing the mean value of $S_q$ and $S_{sk}$ with each level and factor. Based on the ANOVA from Table 2.3, it can be identified that channel orientation again dominates the resulting $S_q$ for 2 mm and 1.5 mm channels; as channel diameter decreases, channel orientation becomes less dominant. $S_{sk}$ is most affected by scan pattern for 1.5 mm and 1 mm channels.

In conclusion, as-fabricated $S_q$ values range between 30-100 $\mu m$ which are orders of magnitude higher than the typical $S_q$ values associated with machined metallic parts (0.5-5 $\mu m$ [57]), and also several times higher than the $S_q$ values of the top flat exposed surfaces of additively manufactured parts (10 $\mu m$ [58]). Between channel diameters, no significant trend is observed in regards to

the overall $S_q$ values. The mean of as-fabricated $S_{sk}$ values across all channels is slightly negative, indicating a slight bias towards troughs on the surface. When the mean is taken across horizontal overhangs and vertical channel wall separately, there is a clear distinction between horizontal channels overhangs tending to be dominated by troughs and vertical channel walls tending to be dominated by peaks.

After electropolishing, we observe a reduction in $S_q$ values, which are further shown to increase in intensity inversely proportional to parameters that relate to laser energy density. However, it is evident that electropolishing is an effective post-process procedure for the reduction in $S_q$. Post-electropolish $S_{sk}$ indicates a bias for peaks for 2 mm and 1.5 mm channels and a bias for troughs for 1 mm channels, generally indifferent to channel orientation.

Overall, significant improvement in surface quality after electropolishing can be observed. The horizontal channel surfaces originally contained stalactites covered in powder feedstock; after electropolishing, these features were almost completely removed, leaving behind thin bridge-like features and some circular topology. The vertical as-fabricated surfaces were originally speckled with partially fused precursor powder, which subsequently yielded a visibly smooth surface with sporadically positioned particles-like features remaining after the electropolish.

# 3. AN EFFICIENT FRAMEWORK TO ACCESS THE PRINTABLE PROCESS SPACE IN LPBF*

## 3.1 Background

Additive manufacturing (AM) is a well-established manufacturing technology capable of producing parts with complex geometries and intricate features, among many other benefits it offers [59, 60]. To unlock AM's full potential, however, more developments are yet to be conducted especially in the areas of materials design and process optimization to enable successful printing of defect-free parts and reduce variability in the properties of fabricated parts [61, 62, 63].

Determining processing recipes for newly designed AM materials can be time-and cost-intensive before a successful print (i.e., a part with near-full density and the minimal amount of macroscopic defects) is realized [64]. In contrast to the experimental-based or modeling-based approaches that have been introduced in chapter 1, some recent studies in the literature indicate that AM processing parameters can be determined via single-track experiments and/or melt pool modeling approach. Bosio et al. developed laser power-scan speed processing maps using single-track experiments for the laser powder bed fusion (LPBF) process [28]. A simplified analytical melt pool model and single-track samples of the LPBF process are used to create a novel density control algorithm [34]. In that paper, an energy density-build rate processing map is numerically generated and experimentally calibrated to support the optimization of printed samples' density.

The current work aims to fill the gaps outlined above to access the printability of new metal alloys in LPBF. More specifically, the objective is to establish a unified framework to determine printability maps for a given newly developed material or alloy in Laser Powder Bed Fusion (LPBF) metal AM processes. In this context, a printability map refers to windows of processing parameters space within which parts free of macroscopic defects can be produced in good region. An

*Reprinted with permission from "An efficient framework for printability assessment in Laser Powder Bed Fusion metal additive manufacturing" by Bing Zhang, Raiyan Seede, Lei Xue, Kadri C Atli, Chen Zhang, Austin Whitt, Ibrahim Karaman, Raymundo Arroyave, Alaa Elwany, 2021. Additive Manufacturing, Volume 46, Pages 102018, Copyright [2021] by Elsevier.

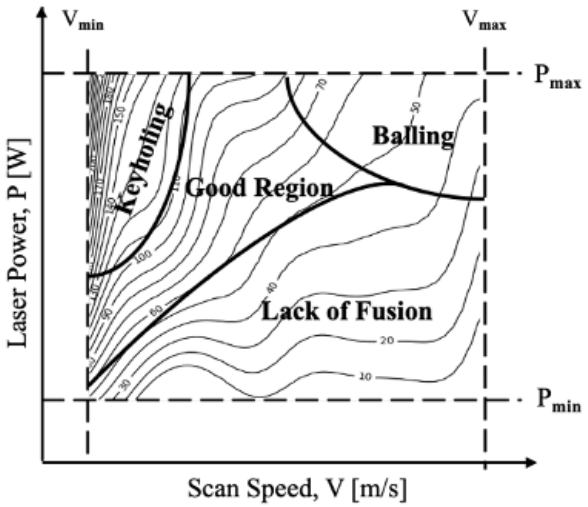


Figure 3.1: An example of a printability map showing processing windows corresponding to different modes or regimes. The contour lines represent maximum hatch spacing that is to be used with a given speed-power combination.

example of such a printability map is depicted in Figure 3.1. The maps proposed in this work are distinguished from processing maps developed by Bosio et al., which work for single-track experiments not in contract to full parts [28]. For the purpose of this work, we focus on three processing parameters shown to have significant influence on the quality of the printed part: laser power, P [W], scan speed, V [m/s], and hatch spacing, h [$\mu$m] [65, 66, 67]. The physical phenomena or regimes that are to be mitigated in order to minimize macroscopic defects (such as pores, cracks, and delamination) are: keyholing [68, 69, 70], lack of fusion [69, 71, 72], and balling [73, 74, 75]. Mechanical properties such as ultimate tensile strength (UTS) and tensile ductility are also tested of the as-printed parts [76].

## 3.2 Methodology

### 3.2.1 Nickel-niobium Alloy ($NiNb_5$)

To simplify the modeling of Nb segregation during rapid solidification of Ni-based alloys, a newly developed binary $NiNb_5$ alloy has been proposed as a surrogate in previous works [77, 33]. In this study, gas atomized $NiNb_5$ powder produced by Nanoval GmbH & Co. KG is used.

[a] 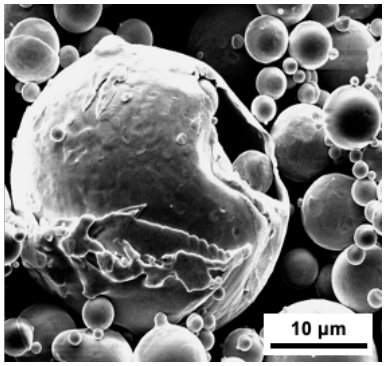

[b] 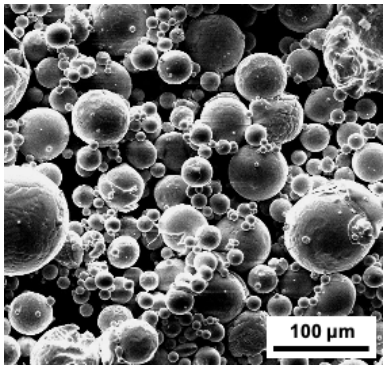


Figure 3.2: SEM micrographs of $NiNb_5$ powder particles. (a) A high magnification image showing the surface morphology of a characteristic powder particle. (b) A low magnification image showing the powder size distribution.

The exact composition of this powder was determined using inductively coupled plasma atomic emission spectroscopy (ICP-AES) for 5.08 ($\pm$ 0.91) wt.% of Nb, the remaining is Ni. $NiNb_5$ powder particles were characterized using a scanning electron microscope (SEM), as shown in Figure 3.2. The particle size distribution and density of the alloy were determined by the supplier, reporting that 80% of the powder particles were smaller than or equal to 30 $\mu m$ ($d80 = 30\mu m$) and that the bulk density '$\rho$' of the material was 8909 $kg/m^3$ (at room temperature). The melting temperature of this alloy is $T_m = 1703\ K$.

Other unknown material properties were estimated as follows: thermal conductivity '$k$', specific heat capacity '$c$', and boiling temperature '$T_b$' were approximated using the rule of mixture for Ni and Nb, and computed as 70.4 $W/(m * K)$, 636.19 $J/(kg * K)$, 3103 $K$, respectively [78, 79, 80]. These properties were selected at the melting temperature in the solid-state as an approximate reference point. The absorptivity '$A$' of the material was approximated using the calculated value for a Gaussian distributed laser beam with 1 $\mu m$ wavelength melting of Ni powder which has an average powder particle radius of 13.5 $\mu m$, and the value is 0.51 [81].

### 3.2.2 Analytical thermal model

The first step in constructing a printability map is through establishing a relationship between AM processing parameters and melt pool geometry. This can then be used to define sub-regions in

the processing parameters space that correspond to different defect criteria (lack of fusion, keyholing, and balling) and to good prints. To generate such a map, a full sweep within the parameters space must be performed. To achieve this, a relatively low fidelity analytical model Eagar-Tsai (E-T) developed by T. W. Eagar and N. S. Tsai is utilized to simulate melt pool geometry across the '$P - V$' parameter space [82]. Although the model was generated with simplifying assumptions to exclude some physics relating to convection and keyhole modes, it represents a reasonable approximation for a starting step. Furthermore, statistical calibration will help adjust the model predictions such that they agree with experiments which will be described later in section [83].

The input parameters of the E-T model include $NiNb_5$ thermo-physical material properties, processing parameters (in particular, laser power and scan speed), and laser beam size. E-T model simulations are used to define sub-regions in the printability map according to defect criteria that are discussed in the next section.

### 3.2.3 Criteria for Establishing the Printable Region

By using the above analytical thermal model, we can get melt pool width and depth simulations for any processing parameter combinations. Our first goal is to reduce this parameter space from a theoretically infinite space in the positive quadrant to a finite space. So, we establish upper and lower bounds on the laser power and scan speed, respectively. The upper bound on the scan speed, '$V_{max}$', is set to the maximum attainable speed by the laser optics on the AM system while the lower bound, '$V_{min}$', is set to an arbitrarily small value slightly above the theoretical minimum (i.e. zero). Because the E-T model requires a moving heat source. 0.05 $m/s$ is taken as the lower bound on the laser speed. The upper bound on the laser power, '$P_{max}$', is set as the maximum power attainable by the AM system (i.e. a machine limitation). The lower bound on the laser power, '$P_{min}$', is set as the minimum laser power that will cause melting at a speed of '$V_{min}$'. This value can be computed using the E-T model. Therefore, we have $P_{min}$ = 65 $W$, $P_{max}$ = 260 $W$, $V_{min}$ = 0.05 $m/s$, and $V_{max}$ = 2.5 $m/s$.

Next, the E-T model is used to further split this space into sub-regions corresponding to phenomena that result in porosity; namely lack of fusion (LOF), keyholing, and balling, as depicted

in Figure 3.3. Lack of fusion porosity is due to voids that create among unmelted or incompletely melted powder particles. Theoretically, LOF occurs when melt pool depth is smaller than powder layer thickness, $\frac{D}{t} < 1$. To be more conservative, the threshold of $\frac{D}{t} < 1.5$ is also considered for our study. Keyhole porosity happens when the deposited laser power is sufficient to cause evaporation of the metal and formation of plasma which leads to the development of a vapor cavity. This enables the laser beam to "drill" to a far deeper depth forming a key shape than is possible in general conduction mode [84]. Literature reported that keyhole mode can be characterized by an aspect ratio of $\frac{W}{D}$ which is material dependent [68]. Here, two thresholds for determining keyholing $\frac{W}{D} < 2.5$ and $\frac{W}{D} < 2.2$ are considered. Balling is a phenomenon where the molten track shrinks and breaks up into a row of discontinuous balls to reduce the surface energy by the surface tension if the molten material does not wet the underlying substrate [85]. When the melting-solidification process takes place under low energy density and very fast scan speed, the balling could happen [73, 86]. In order to classify the balling sub-region, a machine learning algorithm, support vector machine (SVM), is used to fit the characterized balling singles based on their morphology.

Except for the above three defects, as displayed in Figure 3.3, two more temperature-based criteria are considered in the initial printability map to indicate a server condition in metal AM which is unmelting and general condition evaporation. E-T simulations for $NiNb_5$ with its maximum melt pool temperature $T_{max}$ less than $T_m = 1703K$ means that these input processing parameter combinations' energy are too low to melt any powder particle. By plotting another curve with $T_{max}$ equal to $T_b = 3103K$, we get a new sub-region within the finite space. The boiling phenomenon happens outside of it, while within it is roughly treated as the region without material evaporation. These two criteria are only included in the initial printability map as guidance of the design of experiments. For example, few single tracks need to be conducted within the unmelting sub-region.

### 3.2.4 Single Track Experiments

Recall that the E-T has parameter and model uncertainties. For example, those unknown physical material properties. Before finalizing the printability map, it is important to ensure that these

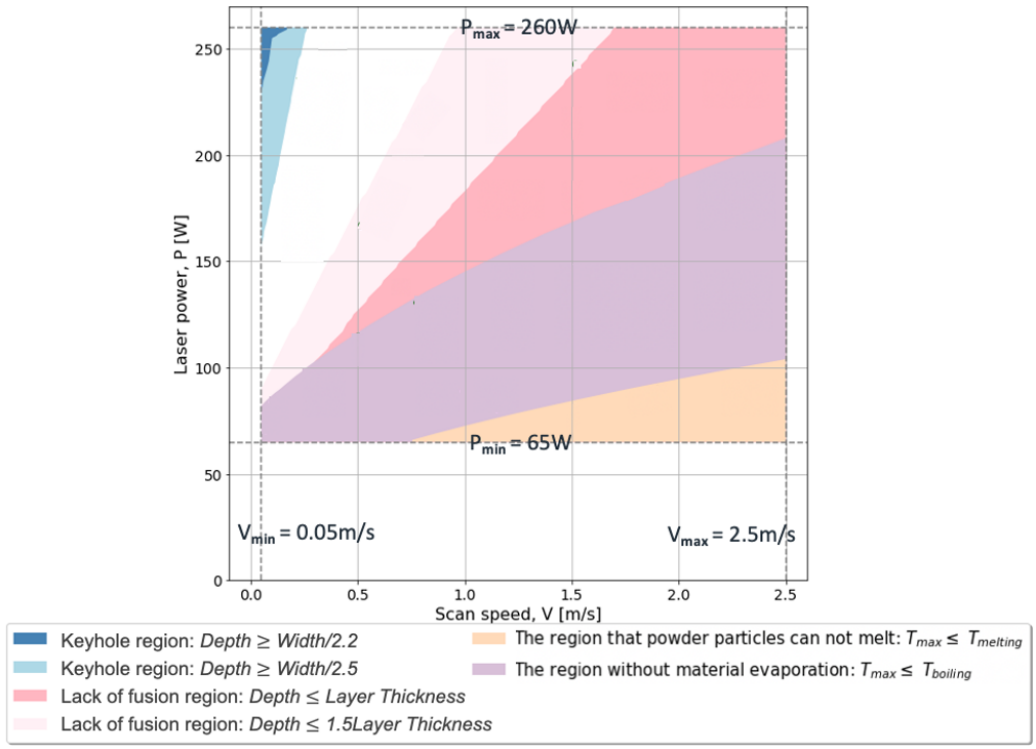


Figure 3.3: The initial printability map of $NiNb_5$.

uncertainties are quantified and accounted such that model predictions of melt pool width and depth are in agreement with experimental characterization. This is a process formally known as statistical calibration which will be described in the next section 2.5. Single-track experiments are conducted to obtain experimental characterization. To initialize the experiment, 40 processing parameter combinations were selected based on the initial printability map. To effectively achieve the three purposes of doing single-track experiments: 1) to calibrate the model predictions agree with experimental characterization; 2) to characterize the relationship between melt pool dimensions and LOF, keyholing, and balling formation mechanisms for $NiNb_5$; 3) to save experimental effort. Both Latin hypercube sampling (LHS) and grid sampling methods were utilized to design the experiments, as shown in Figure 3.4. LHS was implemented in the region ending with $\frac{D}{t} = 1.5$ criteria which is the area having the best experimental results. In that area, as many processing parameter combinations as possible are sampled randomly to evenly spread across the area. LHS can also avoid the "collapsing" property, which means no two design points share the same values

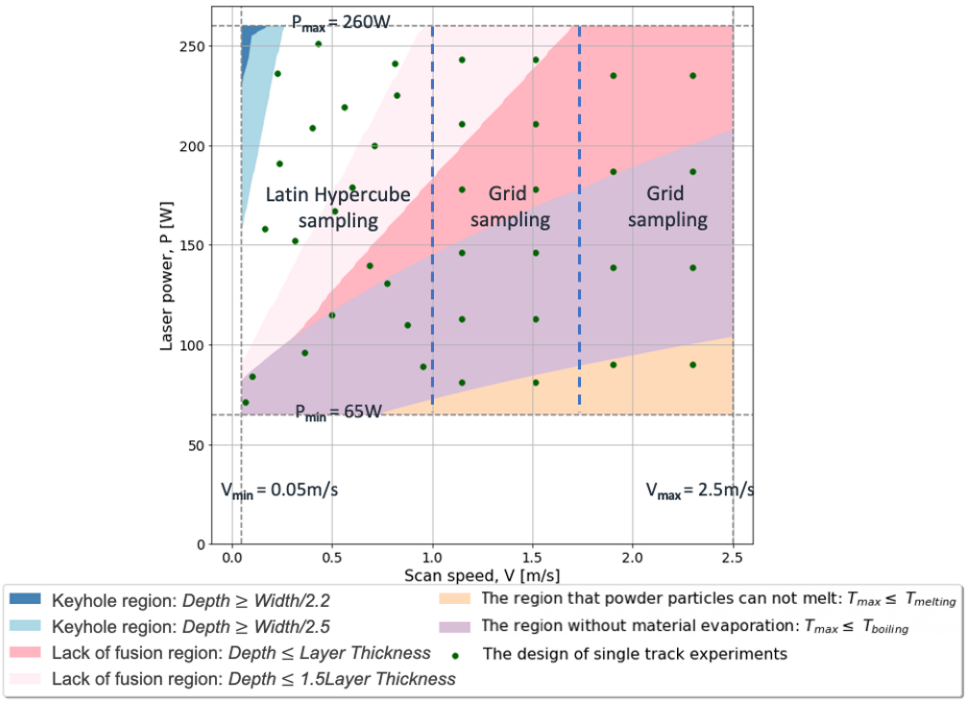


Figure 3.4: The initial printability map of $NiNb_5$ with 40 selected single track experiments.

for any parameter. Grid sampling was applied to the other two areas with different sparse levels split by the ending point of another LOF criteria $\frac{D}{t} = 1$, as depicted in Figure 3.4. Grid sampling is the simplest design method, and require no expert judgment other than the parameter ranges and ensemble size.

In this study, we used the following procedure for conducting single-track experiments. A $NiNb_5$ 70 mm $\times$ 40 mm $\times$ 3 mm dimension stage was printed using 200 W laser power, 1 m/s scan speed, and 120 $\mu m$ hatch spacing. This stage was normalized under industrial-grade argon at 1100 °C for 1 hour and air-cooled. Next, forty tracks were printed following the experimental methodology described in Section 3.4.2.

### 3.2.5 Statistical Calibration of the Thermal Model

Statistical calibration is the process of refining the prior distributions of such uncertain parameters (also called calibration parameters) and model uncertainties by matching model simulations with experimental characterization [87, 51]. We follow a two-step multivariate Bayesian calibra-

tion framework proposed by Mahmoudi and Tapia, details refer to the literature [53, 51]. Here, we mainly present how to reasonably apply this framework to calibrate and estimate uncertain parameters of $NiNb_5$.

Three material properties: thermal conductivity '$k$', specific heat capacity '$c$' and absorptivity '$A$'. which are greatly sensitive to the melt pool morphology were selected as calibration parameters. All possible values of these parameters need to be considered in the model simulation pool for selecting their best estimation. Since the E-T model assumes only conduction mode, heat transfer does not take melt pool convection into account. The optimal effective thermal conductivity value for the E-T model will be inflated compared to the initially assumed value. For this similar reason, the estimated three material property parameters after calibration may not be meaningful in science. Therefore, a large sampling range of these parameters was selected for calibration accuracy(the degree of agreement of the calibrated model predictions with experimental characterization). The sampling ranges of '*k, c, A*' are [10, 100], [450, 650], (0, 1), respectively. Then the mode of each calibration parameter posterior distribution, 42.03 $W/(m * K)$, 457.89 $J/(kg * K)$, and 0.77 were taken as the estimated material properties. As part of the calibration process, a discrepancy function accounts for model uncertainty and a measurement error term is also estimated. Then the calibration accuracy of the E-T model was computed for the mean average error (MAE) of melt pool width and depth: 1.37 $\mu m$ and 1.53 $\mu m$. As well as the mean absolute percentage error (MAPE) of width and depth, which are 1.6% and 4.05%. Less than 5% error is completely acceptable for melt pool characterization. The calibrated E-T model can now be used to update the initial printability map.

### 3.2.6 Finalizing the Printability Map

A new printability map is depicted in Figure 3.5 using the calibrated E-T model predictions. Multiple keyholing regions were classified in this map with different criterion ratios. Forty single tracks were labeled on the map according to the observed melt pool morphology (from top-view and cross-sectional imaging), then utilized to help justify the correct keyholing criteria for this $NiNb_5$ material. The balling region can be classified using the SVM method. An SVM classifier

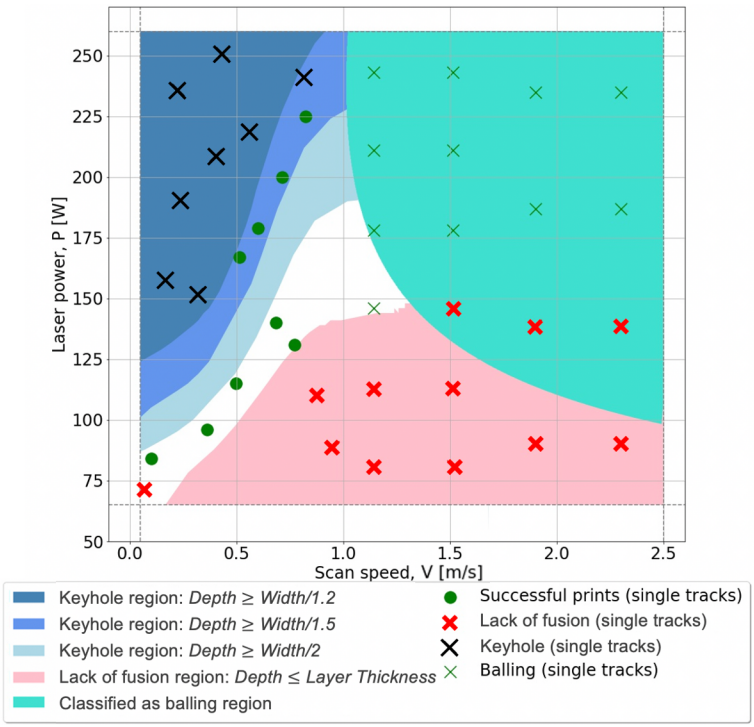


Figure 3.5: The revised printability map of $NiNb_5$ with classified single track characterizations.

with a 3rd degree polynomial kernel that matches the best of the balled tracks is used to split out the balling region. As depicted in Figure 3.5, some of the tracks are missed, misclassified, or exist in two different defect regions. The keyholing criterion $\frac{W}{D} < 1.2$ provides the best fit for classifying keyholing single tracks, only misclassifying 1 track, and does not misclassify any tracks as having undergone keyholing. However, the criteria $\frac{W}{D} < 1.5$ and $\frac{W}{D} < 2$ each misclassified 4 single tracks as having undergone keyholing. Thus, the keyholing region was finalized by $\frac{W}{D} < 1.2$ criterion, as shown in Figure 3.6. The revised printability map in Figure 3.6 is limited to $P - V$ combinations, which are sufficient to print single tracks. To print coupons (and ultimately parts), one needs to determine the hatch spacing parameter '$h$', which is defined as the distance between two adjacent passes of the laser beam within the same layer. Recently, a new approach of computing the maximum allowable hatch spacing is proposed by Seede et al [21]. This hatch spacing criterion is geometrically derived to promote full fusion for a given melt pool width '$W$', melt pool depth '$D$', and layer thickness '$t$'. The maximum hatch spacing '$h_{max}$' for all processing

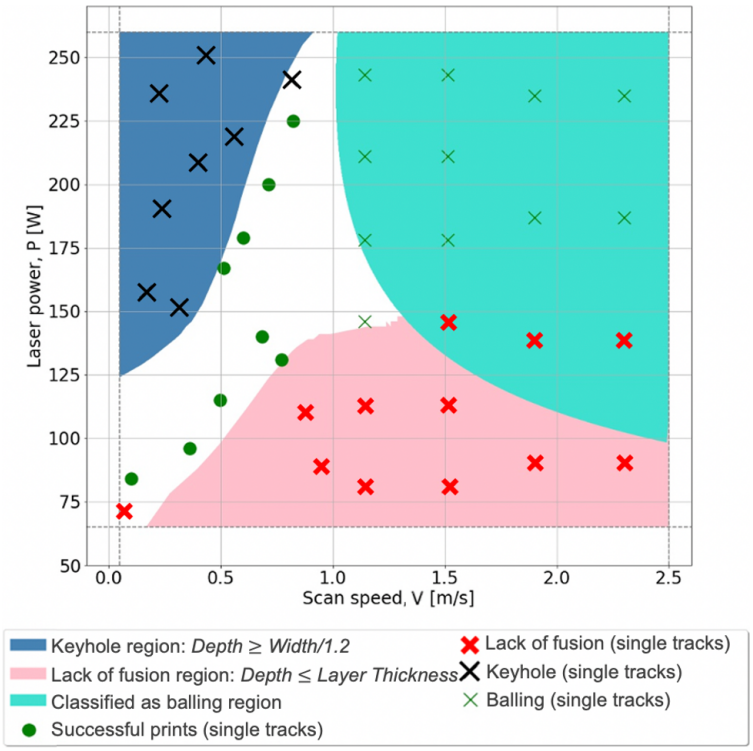


Figure 3.6: The revised printability map of $NiNb_5$ with the finalized criterion for each defect.

parameter combinations in the printability map using the calibrated E-T model predictions of width and depth can be computed by equation:

$$h_{max} = W\sqrt{1 - \frac{t \times D}{D(t+D)}}$$

Figure 3.7 incorporates maximum hatch spacing contour in the revised printability map. In this study, the computed maximum hatch distance is rounded down to the nearest multiple of five for each processing parameter.

### 3.2.7 Printing Coupons and Tensile Testing Specimens

Upon finalizing the printability map, the final step is to print coupons and test specimens guided by the map. These parts were printed on a pure Ni substrate. The process of printing parts is an accumulation from melting multiple single-tracks with the calculated hatch spacing to a single layer, then built up layer upon layer with selected scanning pattern until finish. All parts were

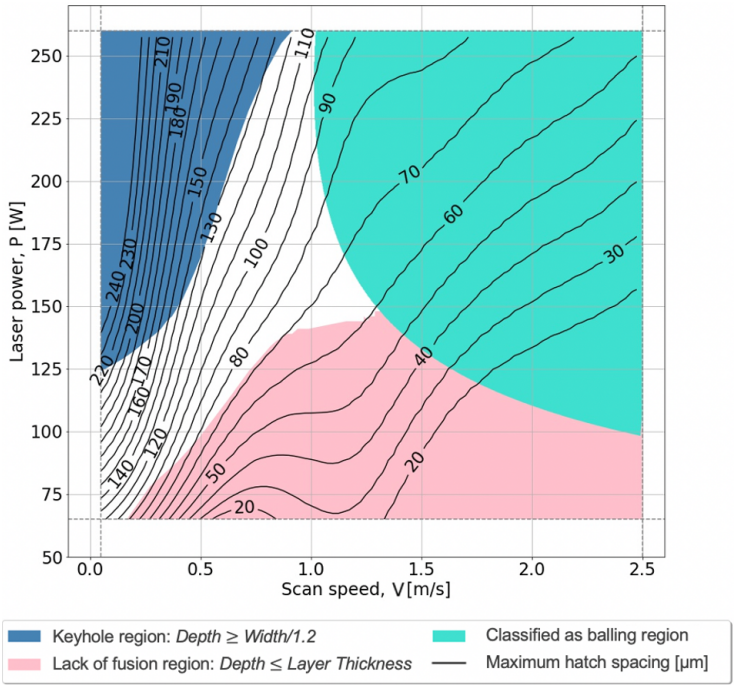


Figure 3.7: The finalized printability map of $NiNb_5$ generated using $\frac{W}{D} < 1.2$ keyholing criterion, $\frac{D}{t} < 1$ lack of fusion criterion, and SVM classifier for balling. The printabiliy map is overlaid with a geometrically based maximum hatch spacing criteria.

printed at a constant layer thickness 30 $\mu m$ following the experimental methodology described in Section 3.4.2.

First, fifteen coupons were printed by the selected processing parameter combinations within and around the good printability region as illustrated in Figure 3.8(a). These 10 mm $\times$ 10 mm $\times$ 10 mm coupons as you can see in Figure 3.8(b) were then cut off from the substrate by EDM for density (or porosity) analysis and compression test.

Next, five processing parameter combinations were selected from the near full density coupons (coupons 3, 7, 8, 13, and 15) to print tensile testing specimens marked in Figure 3.9(a). Five 10 mm $\times$ 10 mm $\times$ 34 mm block specimens were first printed in the horizontal orientation (with respect to the building direction) as depicted in Figure 3.9(b). Three 1 mm thick flat tensile samples were then cut with 26 mm overall length, 7 mm overall width, 8 mm gauge length, and 3 mm gauge width from each block by wire EDM, as shown in Figure 3.10.

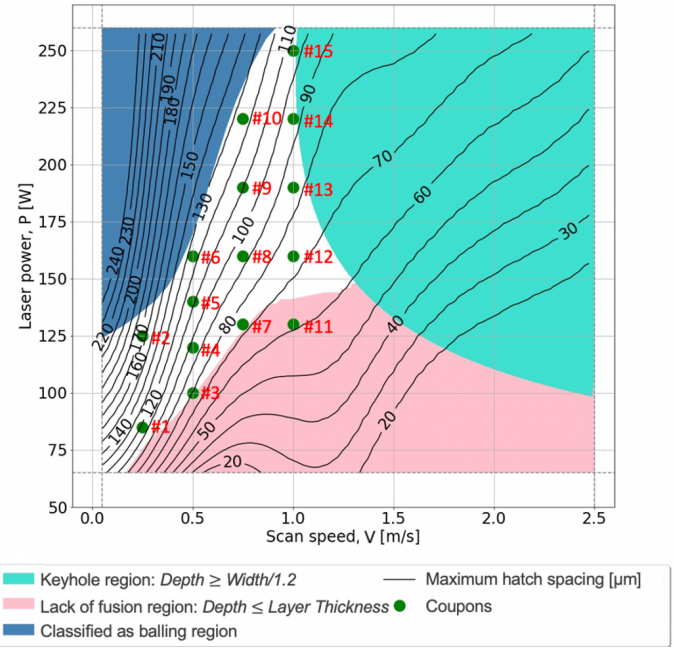


[a]

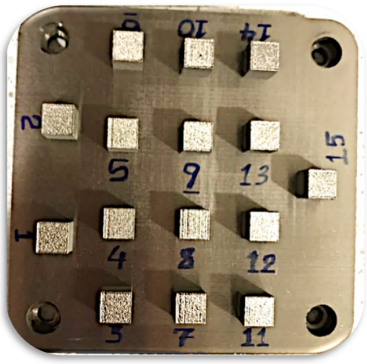

[b]

Figure 3.8: (a)The fifteen selected processing parameter combinations from the finalized printability map for printing $NiNb_5$ coupons. (b)Image of the as-printed coupons for density and microstructure study.

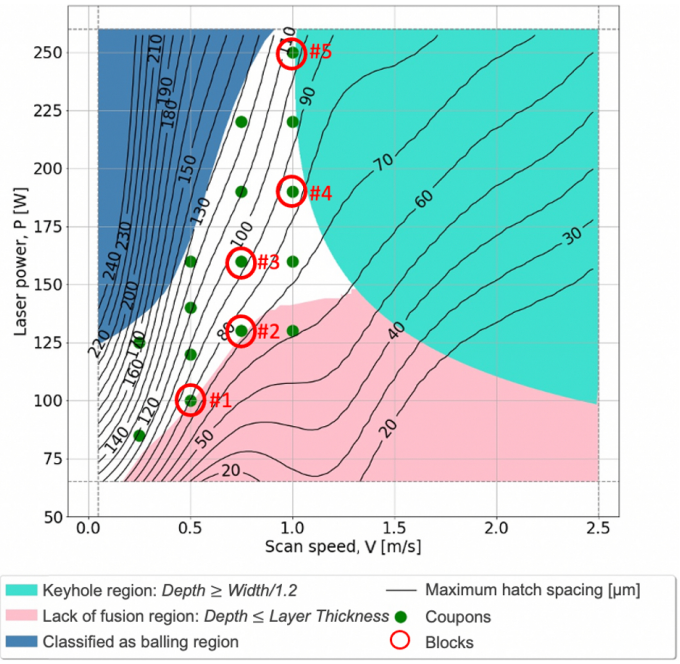


[a]

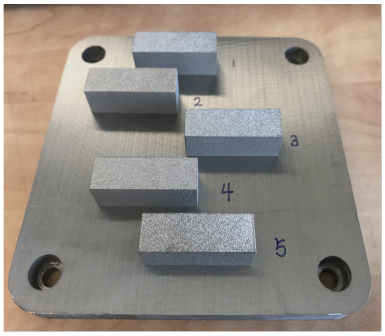

[b]

Figure 3.9: (a) The selected five processing parameter combinations from fifteen coupons. (b) Image of the as-printed block specimens.

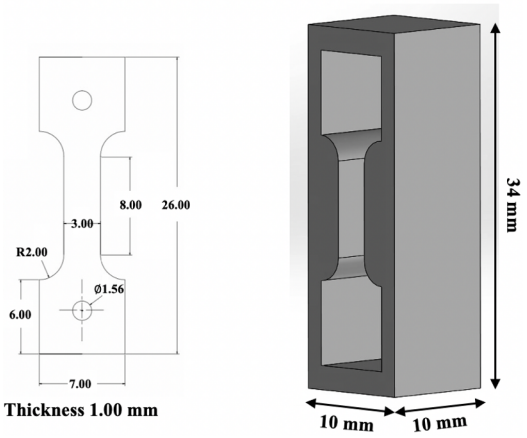


Figure 3.10: The schematic of the block and the mechanical test sample cut from it.

Room temperature monotonic loading tests for compression and tensile samples were conducted with an MTS 810 servo-hydraulic test frame at a strain rate of $5 \times 10^{-4}$ ($s^{-1}$). And an extensometer with ceramic extension rods indirect contact with the gauge section of the samples recording axial strain. Grips equipped with WC platens were utilized to load and unload the samples.

## 3.3 Results and Discussion

### 3.3.1 Density Analysis

The averaged density measurement of each coupon by the OM methods are listed in Table 3.1. Figure 3.11 shows OM images of the polished coupon cross-sections displaying the porosity measurements for the fifteen coupons. 14 out of 15 coupons have OM density above 99%. Even coupon 11 that selected from the lack of fusion region displays an OM density above 99%. Pores are visible in the adjacent tracks of coupons 2 and 10 from Figure 3.11 which correspond to their relatively low OM density 94.45% and 99.03%. This may because of the proximity of the processing parameter combinations to the keyhole region, and possibly due to melt pool morphology prediction error. Since the equation for computing the maximum hatch spacing depends on accurate melt pool dimensions. Prediction errors can result in larger hatch spacing parameter values being used for printing in terms of causing porosity formation in the as-printed coupons.

Table 3.1: The processing parameter combinations and density measurement results of $NiNb_5$ coupons.

| Coupon # | Laser Power (W) | Scan Speed (m/s) | Hatch Spacing ($\mu m$) | Layer Thickness ($\mu m$) | LED (J/m) | OM Density (%) |
|---|---|---|---|---|---|---|
| 1 | 85 | 0.25 | 100 | 30 | 340 | 99.40 |
| 2 | 125 | 0.25 | 165 | 30 | 500 | 94.45 |
| 3 | 100 | 0.5 | 70 | 30 | 200 | 99.83 |
| 4 | 120 | 0.5 | 95 | 30 | 240 | 99.78 |
| 5 | 140 | 0.5 | 110 | 30 | 280 | 99.68 |
| 6 | 160 | 0.5 | 125 | 30 | 320 | 99.42 |
| 7 | 130 | 0.75 | 65 | 30 | 173 | 99.85 |
| 8 | 160 | 0.75 | 90 | 30 | 213 | 99.91 |
| 9 | 190 | 0.75 | 110 | 30 | 253 | 99.78 |
| 10 | 220 | 0.75 | 125 | 30 | 293 | 99.03 |
| 11 | 130 | 1.0 | 55 | 30 | 130 | 99.82 |
| 12 | 160 | 1.0 | 70 | 30 | 160 | 99.79 |
| 13 | 190 | 1.0 | 80 | 30 | 190 | 99.84 |
| 14 | 220 | 1.0 | 95 | 30 | 220 | 99.87 |
| 15 | 250 | 1.0 | 105 | 30 | 250 | 99.80 |

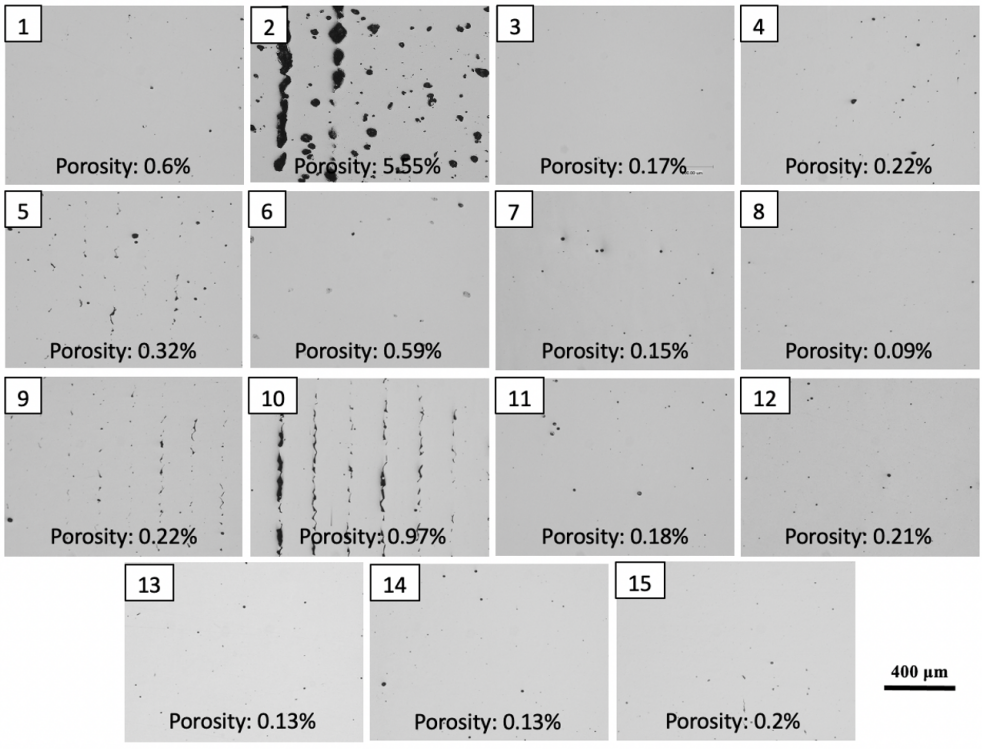


Figure 3.11: OM images of the polished coupon cross-sections displaying the porosity measurements for the fifteen coupons

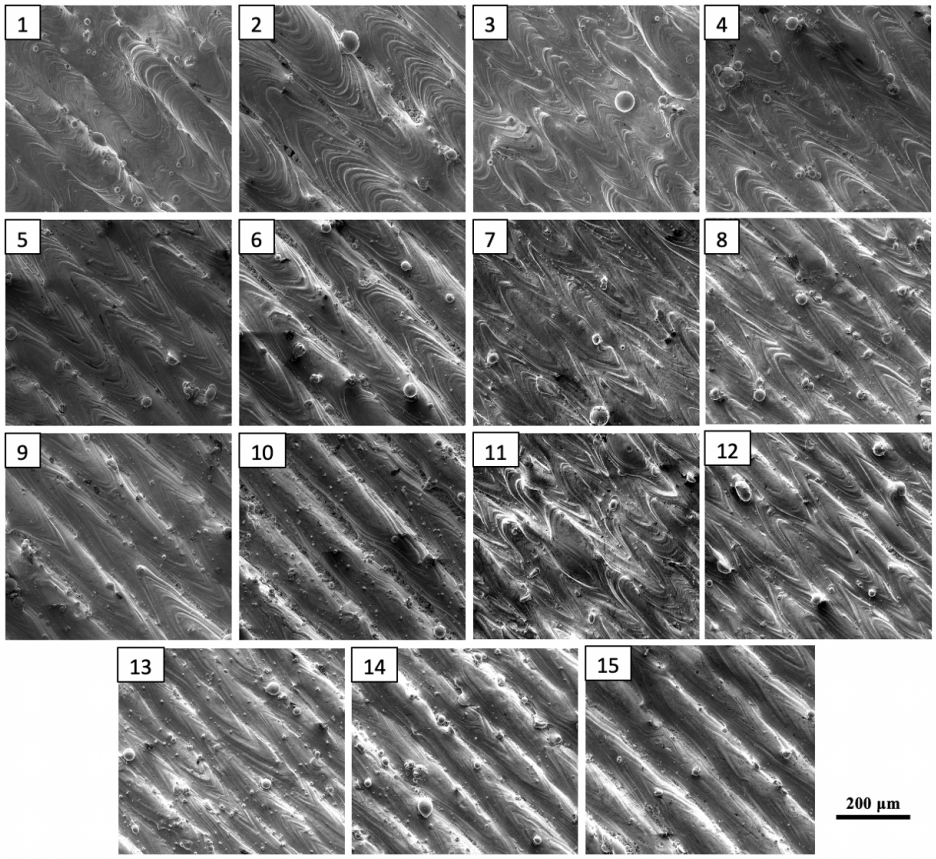


Figure 3.12: SEM micrographs of top surfaces for Coupons 1-15.

### 3.3.2 Microstructure Analysis

Figure 3.12 shows SEM micrographs of the $NiNb_5$ coupons' top surfaces. All fifteen coupons exhibit flat surfaces with low roughness. As shown in this figure, coupon 2 has obvious gaps between tracks with powder particles inside which agrees with the OM density result. Then we took 10 measurements of track width from the top surface for coupon 2 and got an average of 149.83 $\mu m$, which is much smaller than its hatch spacing parameter 165 $\mu m$. For coupon 11, it is difficult to distinguish the tracks at the top surface. This indicates low deposited energy within each track, refers to the LED in Table 3.1.

Figure 3.13 shows the optical micrographs of each polished and etched vertical cross-section (with respect to the building direction) displaying the grain structure. Long and thin columnar

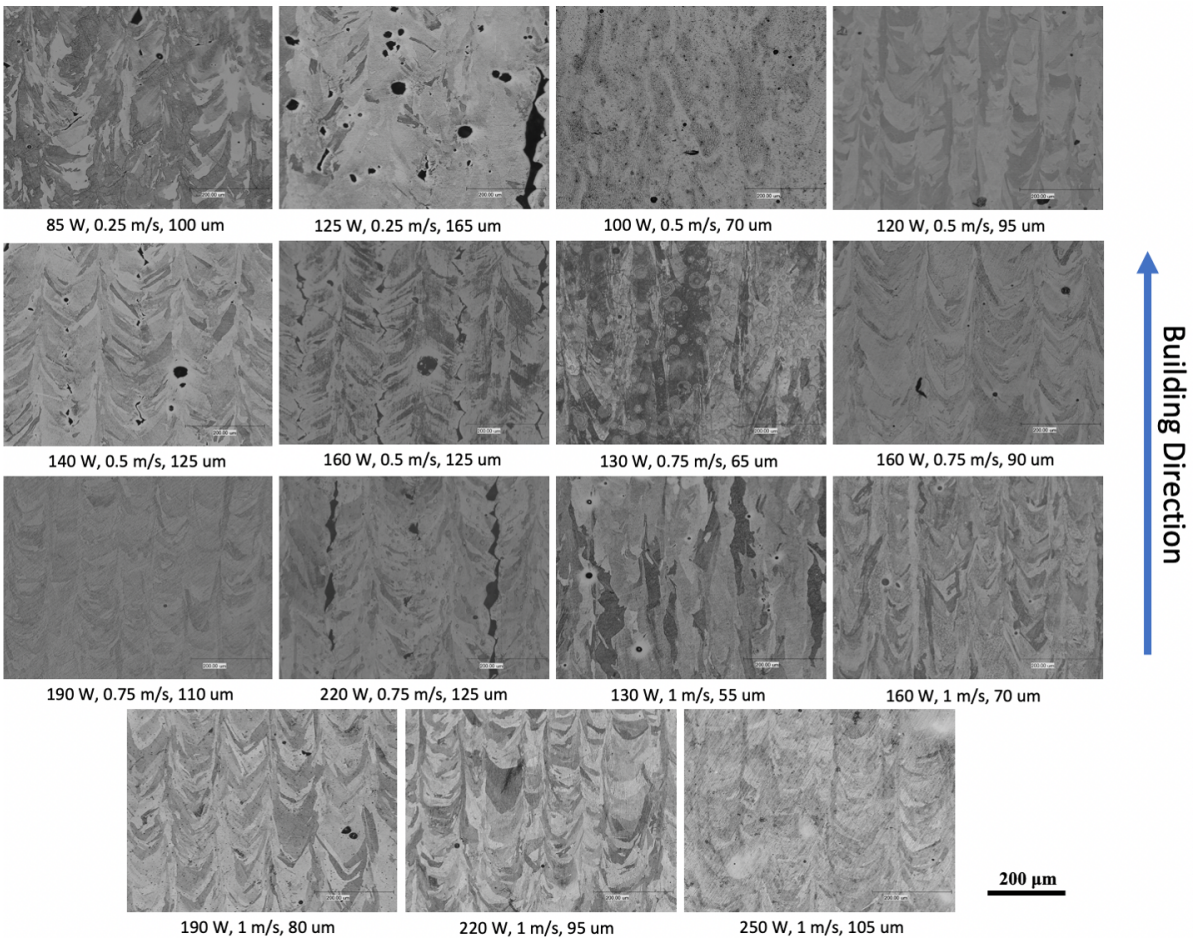


Figure 3.13: OM images of each polished and etched $NiNb_5$ coupon vertical cross-section displaying the grain structure.

grains are dominated with mixed small equiaxed grains in the as-printed coupons. The grain size of each coupon was calculated by taking the average of six measurements at the bottom, middle, and top vertical cross-sections using the intercept method. Due to the relatively high cooling rates at the bottom of the vertical cross-section, grains are stretched towards the cooling direction. The average grain size is larger at the bottom of the vertical section than at the middle which is close to the top. For example, coupon 4 has the average grain size 42 $\mu m$, 31 $\mu m$, and 29 $\mu m$ at the bottom, middle, and top section, respectively. We also observe a larger grain size at higher scan speed when laser power is the same. For example, coupons 6, 8, and 12 with the same laser power and increasing scan speed, having an increasing grain size 26 $\mu m$, 32 $\mu m$, and 35 $\mu m$.

Table 3.2: The compression testing results of horizontal and vertical samples for $NiNb_5$ coupons.

| | Horizontal Compression Sample ‖‖‖ Vertical Compression Sample | | | | | |
|---|---|---|---|---|---|---|
| Coupon # | Elastic Modulus (Mpa) | Yield stress (MPa) | Yield Strain (%) | Elastic Modulus (Mpa) | Yield stress (MPa) | Yield Strain (%) |
| 1 | 86590.14 | 573.88 | 0.86 | 73344.69 | 544.24 | 0.97 |
| 2 | 79971.41 | 463.89 | 0.78 | 72063.43 | 520.34 | 0.92 |
| 3 | 86519.50 | 584.95 | 0.88 | 85954.67 | 567.12 | 0.86 |
| 4 | 116365.94 | 628.12 | 0.74 | 119016.62 | 593.92 | 0.70 |
| 5 | 119456.90 | 614.40 | 0.71 | 120739.98 | 576.05 | 0.68 |
| 6 | 100731.86 | 583.53 | 0.78 | 109265.36 | 553.97 | 0.71 |
| 7 | 114987.34 | 616.22 | 0.74 | 125612.73 | 559.33 | 0.65 |
| 8 | 125954.77 | 625.90 | 0.70 | 124153.98 | 560.76 | 0.65 |
| 9 | 118828.53 | 604.32 | 0.71 | 90860.96 | 582.54 | 0.84 |
| 10 | 118697.41 | 582.00 | 0.69 | 94658.33 | 573.37 | 0.81 |
| 11 | 125194.34 | 604.98 | 0.68 | 101140.89 | 525.65 | 0.72 |
| 12 | 129512.16 | 628.68 | 0.69 | 118604.22 | 561.88 | 0.67 |
| 13 | 129116.18 | 612.02 | 0.67 | 117183.81 | 583.69 | 0.68 |
| 14 | 107177.32 | 608.22 | 0.77 | 99875.00 | 564.70 | 0.77 |
| 15 | 97895.69 | 622.53 | 0.84 | 98247.88 | 569.28 | 0.78 |

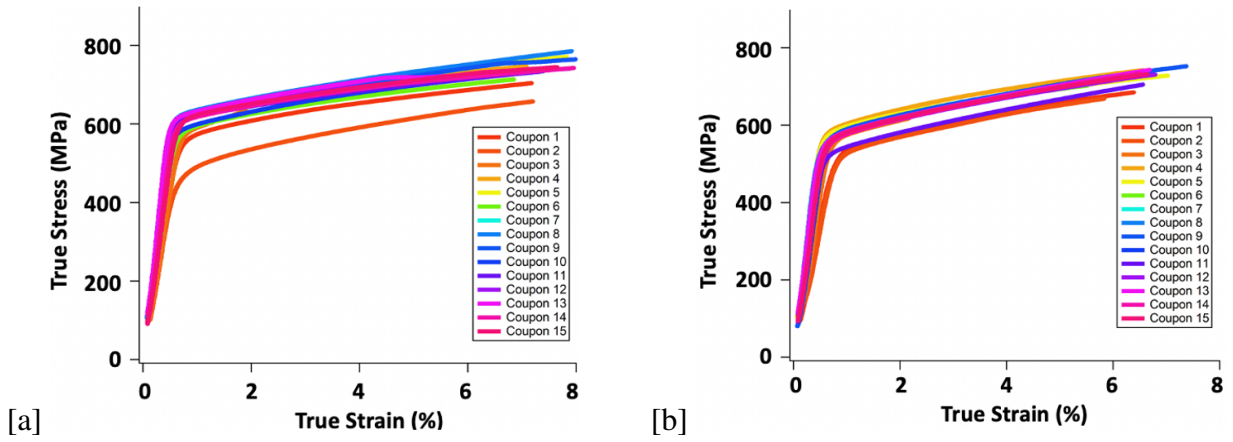


Figure 3.14: (a) Compression testing results of 15 coupons tested in the horizontal direction. (b) Compression testing results of 15 coupons tested in the vertical direction.

### 3.3.3 Mechanical Properties

The fifteen horizontal and vertical specimens (with respect to the building direction) as described in section 2.7 were tested to failure under compression at room temperature. The testing results are listed in Table 3.2 and the strain-stress curves are plotted in Figure 3.14. There is minor difference between these 15 coupons when testing in the same direction. The difference between the testing results in the horizontal and vertical direction is oriented by microstructure and porosity.

Table 3.3: Mechanical property values of $NiNb_5$ block specimens via tensile testing.

| Specimen # | Laser Power (W) | Scan Speed (m/s) | Hatch Spacing ($\mu m$) | Layer Thickness ($\mu m$) | UTS (MPa) | Elongation (%) |
|---|---|---|---|---|---|---|
| 1 | 100 | 0.5 | 70 | 30 | 652.2±4.0 | 24.8±1.0 |
| 2 | 130 | 0.75 | 65 | 30 | 646.8±2.6 | 22.8±0.6 |
| 3 | 160 | 0.75 | 90 | 30 | 662.4±3.2 | 24.9±0.5 |
| 4 | 190 | 1.0 | 80 | 30 | 656.7±2.7 | 25.4±0.2 |
| 5 | 250 | 1.0 | 100 | 30 | 652.6±1.6 | 22.7±1.0 |

Tensile testing was performed at room temperature to characterize the fundamental mechanical properties of the as-printed $NiNb_5$ block specimens, such as ultimate tensile strength (UTS) and tensile ductility [32]. Tensile testing was conducted with an MTS 810 servohydraulic test frame, and an extensometer with ceramic extension rods in direct contact with the gauge section of the specimens recording axial strain. Samples were loaded at a strain rate of $5 \times 10^{-4}$ ($s^{-1}$) until fracture. Three tensile samples were tested in each block and the average mechanical property values are listed in Table 4.3. In addition to a higher average ultimate tensile strength (UTS) of 654 MPa and a greater average tensile ductility of 24% elongation observed in the specimens than the LPBF fabricated pure Ni [88]. The test results indicate low variability in these properties across different block specimens. And similar ductility level to additively manufactured Inconel 718. Through utilizing the printability framework, we got 20% larger strain than the results stated in literature. Figure 3.15 shows the almost same strain-stress relationships recorded under deformation.

From these mechanical testing results, it is reasonable to conclude that by avoiding lack of fusion, keyholing, and balling to achieve printing near full density, the changes in $P, V$, and $h$ are not influential in varying the mechanical properties of the as-printed $NiNb_5$ parts. Through employing the printability framework, $NiNb_5$ parts with a high degree of quality and consistency were successfully produced.

### 3.4 Application of the Printability Framework to Other Alloys

The proposed printability framework has been validated by two other alloys, one is an ultra-high strength martensitic steel (AF9628), and the other one is Nickel Titanium ($Ni_{50.8}Ti_{49.2}$(at.%)). In this section, I will talk about the porosity and mechanical properties of LPBF fabricated samples

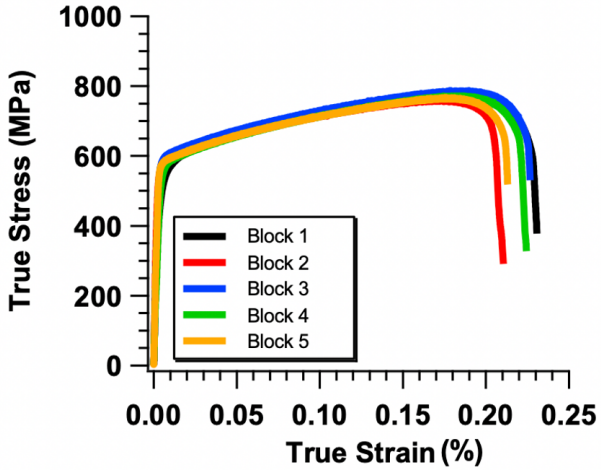


Figure 3.15: The strain-stress curves of tensile samples printed in the horizontal direction (with respect to the building direction).

using the proposed printability framework.

### 3.4.1 Ultra-high Strength Martensitic Steel

Thirteen coupons were fabricated, including one coupon selected from the lack of fusion region as shown in Figure 3.16. Table 3.4 lists the values of processing parameters and corresponding densities measured. Coupons 1-3 with relatively lower density values had excessive spattering during fabrication. Coupon 9 which selected from the lack of fusion region (expected to have a low-density value) achieved 99.78% density. This coupon was printed using a rounded down hatch spacing (to the nearest multiple of five) smaller than the computed maximum value. Four coupons were selected (circled out in Figure 3.16 (b)) as an example to visually compare their different porosity (density) levels from the optical micrographs of the coupon cross-sections.

For mechanical testing, four parameter combinations were selected from the density coupons (coupon 5, 7, 11, and 13) to print block specimens (the same size as $NiNb_5$) in the horizontal and vertical orientations with respect to the building direction, as shown in Figure 3.17 (a). Then 2-3 tensile samples were cut from each block using wire EDM for tensile testing similar to $NiNb_5$. The average mechanical property values are listed in Table 3.5 and the stress-strain curves are displayed in Figure 3.17 (b) and (c). It is interesting to observe that as-printed AF9628 specimens,

[a] 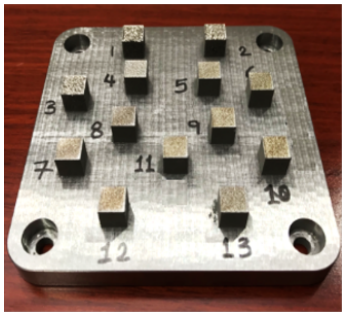


[b] 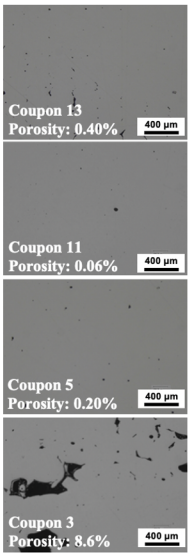


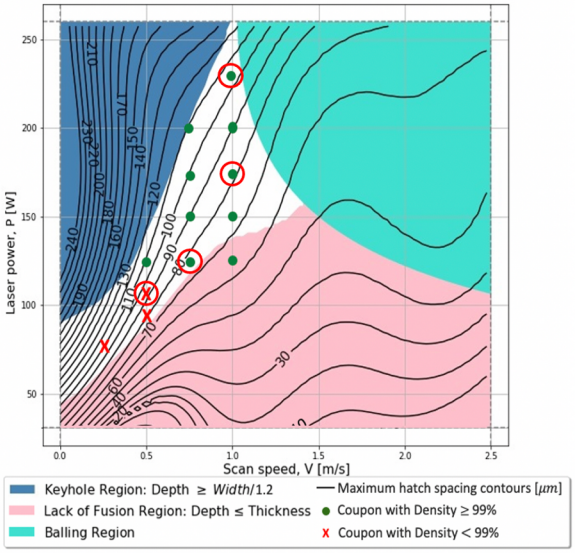


Figure 3.16: (a) Thirteen as-printed AF9628 coupons, and (b) porosity (density) comparison of coupon 13, 11, 5 and 3 from optical micrographs of the polished coupon cross-sections, corresponding to the four circled locations in the processing space from top to bottom.

Table 3.4: The processing parameter combinations and density measurement results of AF9628 coupons.

| Coupon # | Laser Power (W) | Scan Speed (m/s) | Hatch Spacing ($\mu m$) | Layer Thickness ($\mu m$) | Density (%) |
|---|---|---|---|---|---|
| 1 | 73 | 0.25 | 90 | 37 | 79.40 |
| 2 | 93 | 0.5 | 65 | 37 | 81.10 |
| 3 | 105 | 0.5 | 80 | 37 | 91.40 |
| 4 | 125 | 0.5 | 100 | 37 | 99.27 |
| 5 | 125 | 0.75 | 75 | 37 | 99.80 |
| 6 | 150 | 0.75 | 90 | 37 | 99.83 |
| 7 | 175 | 0.75 | 100 | 37 | 99.75 |
| 8 | 200 | 0.75 | 115 | 37 | 99.22 |
| 9 | 125 | 1.0 | 55 | 37 | 99.78 |
| 10 | 150 | 1.0 | 60 | 37 | 99.91 |
| 11 | 175 | 1.0 | 70 | 37 | 99.94 |
| 12 | 200 | 1.0 | 80 | 37 | 99.92 |
| 13 | 233 | 1.0 | 105 | 37 | 99.60 |

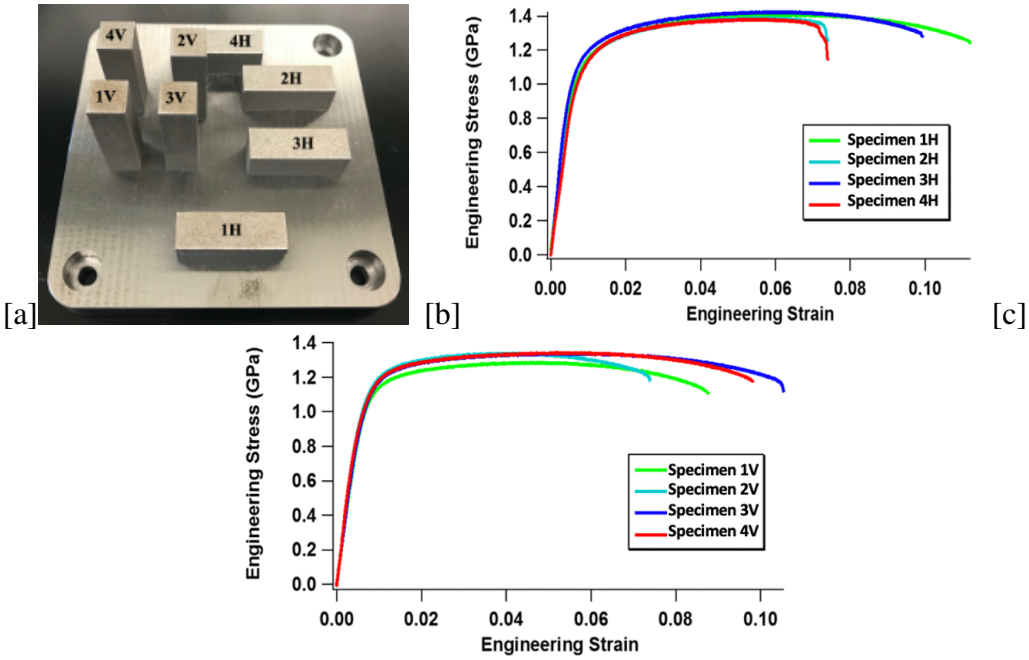


Figure 3.17: The histograms and kernel density estimates of the posterior distributions for the calibration parameters $\boldsymbol{\theta}$.

without any post-process heat treatment, exhibit UTS of up to 1.4 GPa and elongations to fracture of up to 10.9%. UTS values for different specimens with the same build orientation exhibit small degrees of variability across different processing parameter combinations. We also observe that of all the specimens, specimen 3V showed the highest tensile ductility in the vertical direction (10.9% elongation). Specimen 1H showed the highest tensile ductility in the horizontal direction (10.2% elongation). These two parameter combinations have the highest density among the selected four as referred to coupon 11 and 5 in Table 3.4 with a density of 99.94% and 99.8%, respectively. Except for the difference in parameter combinations, different mechanical properties can also be explained by the different microstructure of tensile samples that printed in the horizontal or vertical direction.

### 3.4.2 Nickel Titanium Alloy

Eight processing parameter combinations were selected to fabricate density coupons and the corresponding density results are summarized in Table 3.6. Five of the eight as-printed coupons

Table 3.5: Mechanical property values of as-printed AF9628 specimens. H and V denote horizontal and vertical build orientations.

| Specimen # | Laser Power (W) | Scan Speed (m/s) | Hatch Spacing ($\mu m$) | Layer Thickness ($\mu m$) | UTS (MPa) | Elongation (%) |
|---|---|---|---|---|---|---|
| 1H | 125 | 0.75 | 75 | 37 | $1.40 \pm 0.00$ | $10.16 \pm 1.04$ |
| 1V | 125 | 0.75 | 75 | 37 | $1.31 \pm 0.02$ | $8.95 \pm 0.15$ |
| 2H | 175 | 0.75 | 100 | 37 | $1.41 \pm 0.02$ | $8.38 \pm 0.88$ |
| 2V | 175 | 0.75 | 100 | 37 | $1.34 \pm 0.00$ | $7.40 \pm 0.00$ |
| 3H | 175 | 1.0 | 70 | 37 | $1.43 \pm 0.00$ | $9.79 \pm 0.14$ |
| 3V | 175 | 1.0 | 70 | 37 | $1.32 \pm 0.01$ | $10.89 \pm 0.34$ |
| 4H | 233 | 1.0 | 105 | 37 | $1.42 \pm 0.04$ | $7.71 \pm 0.32$ |
| 4V | 233 | 1.0 | 105 | 37 | $1.38 \pm 0.03$ | $9.51 \pm 0.29$ |

Table 3.6: The processing parameter combinations and density measurement results of NiTi coupons.

| Coupon # | Laser Power (W) | Scan Speed (m/s) | Hatch Spacing ($\mu m$) | Layer Thickness ($\mu m$) | Density (%) |
|---|---|---|---|---|---|
| 1 | 80 | 0.33 | 80 | 40 | 98.73 |
| 2 | 120 | 0.33 | 130 | 40 | 97.16 |
| 3 | 160 | 0.58 | 110 | 40 | 98.50 |
| 4 | 160 | 0.83 | 80 | 40 | 99.92 |
| 5 | 200 | 0.83 | 100 | 40 | 99.81 |
| 6 | 160 | 1.08 | 70 | 40 | 99.98 |
| 7 | 200 | 1.08 | 80 | 40 | 100.00 |
| 8 | 240 | 1.33 | 80 | 40 | 99.97 |

have density values larger than 99%. The as-printed eight coupons are displayed in Figure 3.18 (a). Four coupons were selected (circled out in Figure 3.18 (b)) as an example to visually compare their different porosity (density) levels from the optical micrographs of the polished coupon cross-sections.

Similar to $NiNb_5$, four coupon parameter combinations with density greater than 99.9% were selected to print 10 mm × 10 mm × 30 mm block specimens in the horizontal direction with respect to the building direction as shown in Figure 3.19 (a). One tensile sample of each block with gauge dimensions of 8 mm × 2 mm × 1 mm was tested at room temperature and the mechanical property values are listed in Table 3.7. Stress-strain curves of the as-printed NiTi specimens are displayed in Figure 3.19 (b). Reasonable mechanical properties were achieved by printing tensile blocks with near full density parameters.

The framework has been validated by three alloys, parameter combinations that result in parts with good density and mechanical properties are obtained. Two key benefits are: (1) the ability

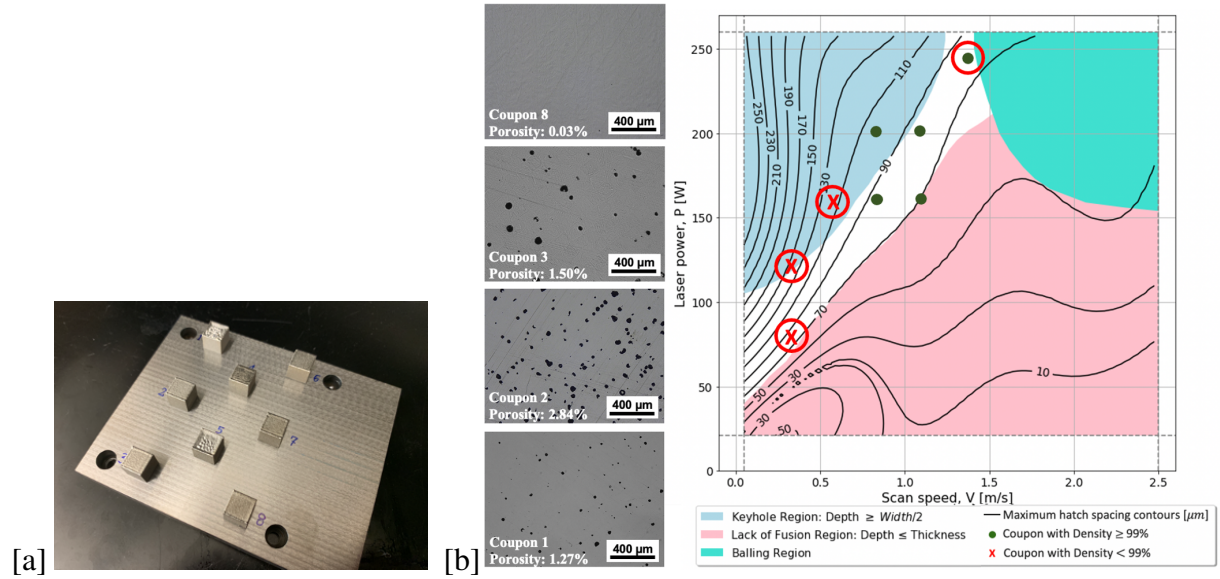


Figure 3.18: (a) Eight as-printed NiTi coupons, and (b) porosity (density) comparison of coupon 8, 3, 2 and 1 from optical micrographs of the polished coupon cross-sections, corresponding to the four circled locations in the processing space from top to bottom.

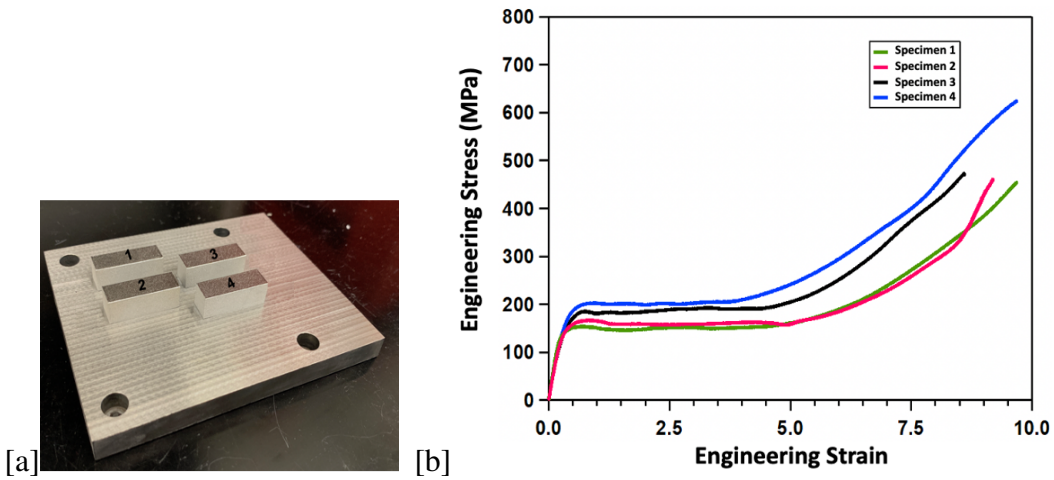


Figure 3.19: (a) Four as-printed NiTi tensile blocks in horizontal building orientation, and (b) representative stress-strain curves of the as-printed NiTi specimens. Refer to Table 3.7 for the corresponding parameter combinations.

Table 3.7: Mechanical property values of as-printed NiTi specimens via tensile testing.

| Specimen # | Laser Power (W) | Scan Speed (m/s) | Hatch Spacing ($\mu m$) | Layer Thickness ($\mu m$) | UTS (MPa) | Elongation (%) |
|---|---|---|---|---|---|---|
| 1 | 240 | 1.33 | 80 | 40 | 454 | 9.7 |
| 2 | 200 | 1.08 | 80 | 40 | 461 | 9.2 |
| 3 | 160 | 0.83 | 80 | 40 | 471 | 8.6 |
| 4 | 160 | 1.08 | 70 | 40 | 623 | 9.7 |

to determine good printability regions in an accelerated fashion, eliminating the need for cost- and time-intensive processing parameter sweeps, and (2) the accessibility of the framework to practitioners since it does not rely on the use of proprietary codes for the thermal model utilized.

# 4. ROBUST CALIBRATION OF MULTIVARIATE MODEL WITH MISSING DATA

## 4.1 Background

Microstructural or mechanical characterization is an essential procedure to quantify the quality of a fabricated part through experimental test. However, not all of the experimental results of additively manufactured parts can be measured due to: (1) destructive testing process while collecting data, (2) limited human effort, or (3) expensive measurement cost. While developing the printability framework, we find that the measuring process of melt pool depth is expensive and destructive which causes difficulties in conducting the calibration work of E-T model. The problem of statistical calibration with "unobservable" experimental results or missing data is proposed and described in Figure 4.1. Where we have control inputs $\boldsymbol{x}$, such as laser power and laser scan speed. Calibration parameters $\boldsymbol{\theta}$, such as the unknown material properties. And the QoIs $\boldsymbol{y}^E$ which is split into $\boldsymbol{y}_{mis}$ and $\boldsymbol{y}_{obs}$, such as the observed melt pool geometries.

In calibrating the analytical thermal model in the proposed framework, or in conducting uncertainty quantification of computer model in ICME, experimental results are the ground truth to tune the distribution of calibration parameters (the unknown parameters of model, for example, the material properties of newly developed alloys). The literature on statistical calibration

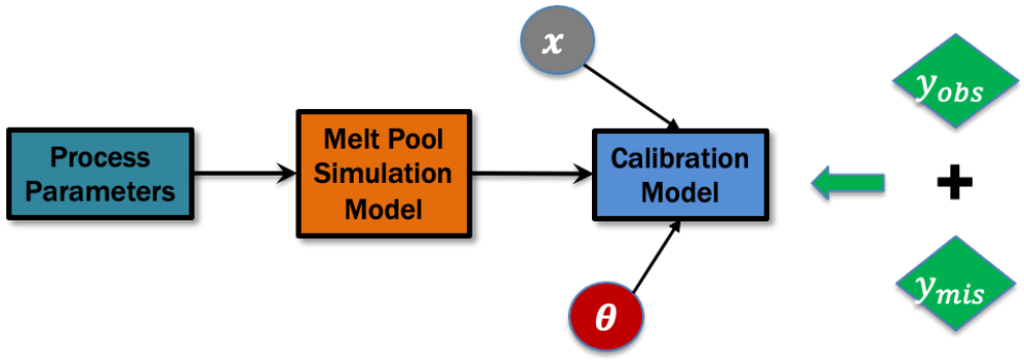


Figure 4.1: Graph of the statistical calibration problem with "unobservable" experimental results or missing data.

of a computer model is rich, many of them use the so-called two-stage framework developed by Kennedy and O'Hagan (known as KOH framework) [51]. In the KOH framework, a surrogate model of the computer model is generated in the first stage to effectively generate simulations. Then a calibration model is formed to have the surrogate model predictions match experimental results. Recently, Mahmoudi et al. explored Kennedy and O'Hagan's framework to handle a computer model with multiple outputs in AM via multivariate Gaussian processes. We will name this method as MVCalib for short. In mathematical notation, the calibration model is denoted as the following equation:

$$\boldsymbol{y}^E(\boldsymbol{x}) = \boldsymbol{y}^S(\boldsymbol{x}, \boldsymbol{\theta}) + \boldsymbol{\delta}(\boldsymbol{x}) + \boldsymbol{\epsilon}(\boldsymbol{x}) \tag{4.1}$$

Where the q-dimensional QoIs $\boldsymbol{y}^E$ of the real process observed at a finite set of control inputs $\boldsymbol{x}$ is equal to the summation of the surrogate model simulation $\boldsymbol{y}^S$, a discrepancy function $\boldsymbol{\delta}$, and a measurement error term $\boldsymbol{\epsilon}$, and the objective is to estimate the values of the calibration parameters $\boldsymbol{\theta}$. With approximation, the calibration model resulting from Equation 4.1 is a multivariate q-dimensional GP given by $\boldsymbol{y}^E(\cdot)|\boldsymbol{\phi} \sim GP_q(m^*(\cdot, \boldsymbol{\theta}), C_{sur}^{cal}(\cdot,\cdot)\hat{\boldsymbol{\Sigma}} + C_{\delta}^{cal}(\cdot,\cdot)\boldsymbol{\Sigma}_{\boldsymbol{\delta}} + C_{\epsilon}^{cal}(\cdot,\cdot)\boldsymbol{\Sigma}_{\boldsymbol{\epsilon}})$. Where $\boldsymbol{\phi} = \boldsymbol{\theta}, \boldsymbol{r}_{\delta}, \boldsymbol{\sigma}_{\delta}, \boldsymbol{\psi}$ is the set of calibration parameters and hyperparameters that will be estimated. Next, the distribution is rearranged by stacking each vector $\boldsymbol{y}^E(\boldsymbol{x}_i^E)$ to follow a multivariate

normal distribution (MVN).

$$P(\boldsymbol{Y}^E|\boldsymbol{\phi}, \boldsymbol{X}^E, \boldsymbol{X}^S, \boldsymbol{Y}^S) \sim MVN_{n\cdot q}(\boldsymbol{m^*}, \boldsymbol{\Sigma}_{cal})$$

where

$$\begin{aligned}
\boldsymbol{Y}^E &= [Y^E_{1,1}, ..., Y^E_{1,q}, ..., Y^E_{n,1}, ..., Y^E_{n,q}]^T \in \mathbb{R}^{n\cdot q,1} \\
\boldsymbol{Y}^S &= [Y^S_{1,1}, ..., Y^S_{1,q}, ..., Y^S_{N,1}, ..., Y^E_{N,q}]^T \in \mathbb{R}^{N\cdot q,1} \\
\boldsymbol{X}^E &= [\boldsymbol{x}^E_1, ..., \boldsymbol{x}^E_n] \in \mathbb{R}^{n\cdot p,1} \\
\boldsymbol{X}^S &= [(\boldsymbol{x}, \boldsymbol{\theta})_1, ..., (\boldsymbol{x}, \boldsymbol{\theta})_N] \in \mathbb{R}^{N,p+t} \\
\boldsymbol{m^*} &= [m^*(\boldsymbol{x}^E_1, \boldsymbol{\theta}), ..., m^*(\boldsymbol{x}^E_n, \boldsymbol{\theta})]^T \in \mathbb{R}^{n\cdot q,1} \\
\boldsymbol{\Sigma}_{cal} &= \boldsymbol{C}^{cal}_{sur} \otimes \hat{\boldsymbol{\Sigma}} + \boldsymbol{C}^{cal}_{\delta} \otimes \boldsymbol{\Sigma}_{\delta} + \boldsymbol{C}^{cal}_{\epsilon} \otimes \boldsymbol{\Sigma}_{\epsilon} \in \mathbb{R}^{n\cdot q,n\cdot q} \\
\boldsymbol{C}^{cal}_{sur} &= [c^*((x^E_i, \theta), (x^E_i, \theta))]_{i,j=1:n} \in \mathbb{R}^{n,n} \\
\boldsymbol{C}^{cal}_{\delta} &= [c_\delta(x^E_i, x^E_j)]_{i,j=1:n} \in \mathbb{R}^{n,n} \\
\boldsymbol{C}^{cal}_{\epsilon} &= [c_\epsilon(x^E_i, x^E_j)]_{i,j=1:n} = \boldsymbol{I}_{n,n} \in \mathbb{R}^{n,n}
\end{aligned} \tag{4.2}$$

The Kronecker matrix product ($\otimes$) is employed to calculate cross-covariance matrix $\boldsymbol{\Sigma}_{cal}$ which represents spatial dependence between inputs and outputs.

Where,

$$\boldsymbol{m}^{*}(x_1^E, \boldsymbol{\theta}) = \hat{\boldsymbol{B}}^T h(\boldsymbol{x}, \boldsymbol{\theta}) + (\boldsymbol{Y}^S - \boldsymbol{H}\hat{\boldsymbol{B}})^T \boldsymbol{A}^{-1} \boldsymbol{t}(\boldsymbol{x}, \boldsymbol{\theta})$$

$$c^{*}((\boldsymbol{x}, \boldsymbol{\theta})_i, (\boldsymbol{x}, \boldsymbol{\theta})_j) = c((\boldsymbol{x}, \boldsymbol{\theta})_i, (\boldsymbol{x}, \boldsymbol{\theta})_j) - \boldsymbol{t}^T(\boldsymbol{x}, \boldsymbol{\theta})_i \boldsymbol{A} \boldsymbol{t}(\boldsymbol{x}, \boldsymbol{\theta})_j$$

$$+[h(\boldsymbol{x}, \boldsymbol{\theta})_i - \boldsymbol{H}^T \boldsymbol{A}^{-1} \boldsymbol{t}(\boldsymbol{x}, \boldsymbol{\theta})_i]^T$$

$$\times (\boldsymbol{H}^T \boldsymbol{A}^{-1} \boldsymbol{H})^{-1}$$

$$\times [h(\boldsymbol{x}, \boldsymbol{\theta})_i - \boldsymbol{H}^T \boldsymbol{A}^{-1} \boldsymbol{t}(\boldsymbol{x}, \boldsymbol{\theta})_i]$$

$$\hat{\boldsymbol{\Sigma}} = (N - m)^{-1} (\boldsymbol{Y}^S - \boldsymbol{H}\hat{\boldsymbol{B}})^T \boldsymbol{A}^{-1} (\boldsymbol{Y}^S - \boldsymbol{H}\hat{\boldsymbol{B}})$$

$$c_\delta(\boldsymbol{x}_i, \boldsymbol{x}_j) = exp[-(\boldsymbol{x}_i - \boldsymbol{x}_j)^T R_\delta (\boldsymbol{x}_i - \boldsymbol{x}_j)]$$

$$\boldsymbol{\Sigma}_\delta = diag(\boldsymbol{\sigma}_\delta)$$

$$c_\epsilon(\boldsymbol{x}_i, \boldsymbol{x}_j) = \begin{cases} 1 \; if \boldsymbol{x}_i = \boldsymbol{x}_j \\ 0 \; if \boldsymbol{x}_i \neq \boldsymbol{x}_j \end{cases}$$

$$\boldsymbol{\Sigma}_\epsilon = diag(\boldsymbol{\psi})$$

With

$$\boldsymbol{H}^T = [h(\boldsymbol{x},\boldsymbol{\theta})_1, ..., h(\boldsymbol{x},\boldsymbol{\theta})_N] \in \mathbb{R}^{m,N}$$

$$\boldsymbol{A} = [c(\boldsymbol{x},\boldsymbol{\theta})_i, ..., (\boldsymbol{x},\boldsymbol{\theta})]_{i,j=1:N} \in \mathbb{R}_+^{N,N}$$

$$\boldsymbol{t}^T(\boldsymbol{x},\boldsymbol{\theta})_i = [c((\boldsymbol{x},\boldsymbol{\theta})_i, (\boldsymbol{x},\boldsymbol{\theta})_1), ..., ((\boldsymbol{x},\boldsymbol{\theta})_i, ..., (\boldsymbol{x},\boldsymbol{\theta})_N)] \in \mathbb{R}^N$$

$$\hat{\boldsymbol{B}} = (\boldsymbol{H}^T\boldsymbol{A}^{-1}\boldsymbol{H})^{-1}\boldsymbol{H}^T\boldsymbol{A}^{-1}\boldsymbol{Y}^S$$

$$c((\boldsymbol{x},\boldsymbol{\theta})_i, (\boldsymbol{x},\boldsymbol{\theta})_j) = exp[-((\boldsymbol{x},\boldsymbol{\theta})_i, (\boldsymbol{x},\boldsymbol{\theta})_j)^T R((\boldsymbol{x},\boldsymbol{\theta})_i, (\boldsymbol{x},\boldsymbol{\theta})_j)]$$

$$R = diag(\boldsymbol{r})$$

$$\boldsymbol{r} = [r_1, ..., r_p, r_{p+1}, ..., r_{p+t}] \in \mathbb{R}_+^{p+t}$$

$$R_\delta = diag(\boldsymbol{r}_\delta)$$

$$\boldsymbol{r}_\delta = [r_1^\delta, ..., r_p^\delta] \in \mathbb{R}_+^p$$

$$\boldsymbol{\sigma}_\delta = [\sigma_1, ..., \sigma_q] \in \mathbb{R}_+^q$$

$$\boldsymbol{\psi} = [\psi_1, ..., \psi_q] \in \mathbb{R}_+^q$$

Details of this method can be referred to Mahmoudi et al.'s paper [53]. The next step is to estimate the posterior distributions for the calibration parameters $\boldsymbol{\theta}$ and hyperparameters $\boldsymbol{r}_\delta, \boldsymbol{\sigma}_\delta, \boldsymbol{\psi}$ to match the values of experimental results.

Two different method are developed to handle the case of statistical calibration with "unobservable" experimental results or missing data. The first method is to predict the missing data by a proposed hierarchical Gaussian process model (HGPM). Then the depth predictions are combined with experimental results to conduct calibration by MVCalib method. The other method is to directly estimate the calibration parameters and hyperparameters of statistical calibration model in the MVCalib method by a calibrated Bayesian multiple imputation (CBMI) method. So that the calibrated parameters can be used in the predictive distribution of model outputs

$P[\boldsymbol{Y}^P|\boldsymbol{X}^P, \boldsymbol{X}^E, \boldsymbol{Y}^E, \boldsymbol{X}^S, \boldsymbol{Y}^S, \boldsymbol{\phi}]$ with the following parameters:

$$
\begin{aligned}
E[\boldsymbol{Y}^P|\boldsymbol{Y}^E] &= E[\boldsymbol{Y}^P|\boldsymbol{X}^P, \boldsymbol{X}^E, \boldsymbol{Y}^E, \boldsymbol{X}^S, \boldsymbol{Y}^S, \boldsymbol{\phi}] \\
&= \boldsymbol{m}_{pred} + \boldsymbol{\Sigma}^{PE}{\boldsymbol{\Sigma}_{cal}}^{-1}(\boldsymbol{Y}^E - \boldsymbol{m}^*) \\
&\text{where} \\
\boldsymbol{X}^P &= [\boldsymbol{x}_1^P, ..., \boldsymbol{x}_s^P] \in \mathbb{R}^{s\cdot p,1} \\
\boldsymbol{m}_{pred} &= [m^*(\boldsymbol{x}_1^P, \boldsymbol{\theta}), ..., m^*(\boldsymbol{x}_s^P, \boldsymbol{\theta})]^T \in \mathbb{R}^{s\cdot q,1} \\
\boldsymbol{\Sigma}^{PE} &= \boldsymbol{C}_{sur}^{PE} \otimes \hat{\boldsymbol{\Sigma}} + \boldsymbol{C}_{\delta}^{PE} \otimes \boldsymbol{\Sigma}_{\delta} \in \mathbb{R}^{s\cdot q, s\cdot q} \\
\boldsymbol{C}_{sur}^{PE} &= [c^*(\boldsymbol{x}_i^P, \boldsymbol{x}_i^E, \theta^*)] = [c^*(\boldsymbol{x}_i^P, \boldsymbol{\theta}), (\boldsymbol{x}_i^E, \boldsymbol{\theta})]_{i=1:s, j=1:n} \in \mathbb{R}^{s,n} \\
\boldsymbol{C}_{\delta}^{PE} &= [c_{\delta}(\boldsymbol{x}_i^P, \boldsymbol{x}_j^E)]_{i=1:s, j=1:n} \in \mathbb{R}^{s,n}
\end{aligned}
\tag{4.3}
$$

and

$$
\begin{aligned}
Var[\boldsymbol{Y}^P|\boldsymbol{Y}^E] &= Var[\boldsymbol{Y}^P|\boldsymbol{X}^P, \boldsymbol{X}^E, \boldsymbol{Y}^E, \boldsymbol{X}^S, \boldsymbol{Y}^S, \boldsymbol{\phi}] \\
&= \boldsymbol{\Sigma}_{pred} - \boldsymbol{\Sigma}^{PE}\boldsymbol{\Sigma}_{cal}^{-1}(\boldsymbol{\Sigma}^{PE})^T \\
&\text{where} \\
\boldsymbol{\Sigma}_{pred} &= \boldsymbol{C}_{sur}^{pred} \otimes \hat{\boldsymbol{\Sigma}} + \boldsymbol{C}_{\delta}^{pred} \otimes \boldsymbol{\Sigma}_{\delta} + \boldsymbol{C}_{\epsilon}^{pred} \otimes \boldsymbol{\Sigma}_{\epsilon} \in \mathbb{R}^{s\cdot q, s\cdot q} \\
C_{sur}^{pred} &= [c^*((\boldsymbol{x}_i^P, \boldsymbol{\theta}), (\boldsymbol{x}_i^P, \boldsymbol{\theta})]_{i,j=1s} \in \mathbb{R}^{s,s} \\
\boldsymbol{C}_{\delta}^{pred} &= [c_{\delta}(\boldsymbol{x}_i^P, \boldsymbol{x}_j^P)]_{i,j=1:s} \in \mathbb{R}^{s,s} \\
\boldsymbol{C}_{\epsilon}^{pred} &= [c_{\epsilon}(\boldsymbol{x}_i^P, \boldsymbol{x}_j^P)]_{i,j=1:s} = \boldsymbol{I}_{s,s} \in \mathbb{R}^{s,s}
\end{aligned}
\tag{4.4}
$$

## 4.2 Experiments

The analytical thermal model Eagar-Tsai (E-T) is used for melt pool width (W) and depth (D) simulations in the proposed printability framework. A representative output of the E-T melt pool model that shows W and D is shown in Figure 4.2. As this model was originally developed for laser welding process, it misses physics specific in LPBF processes such as keyholing formation. Since there is no powder layer in welding process, we assume that laser directly melt the solid metal alloy. Due to these facts, the simulations of E-T model is unable to mimic the real melt

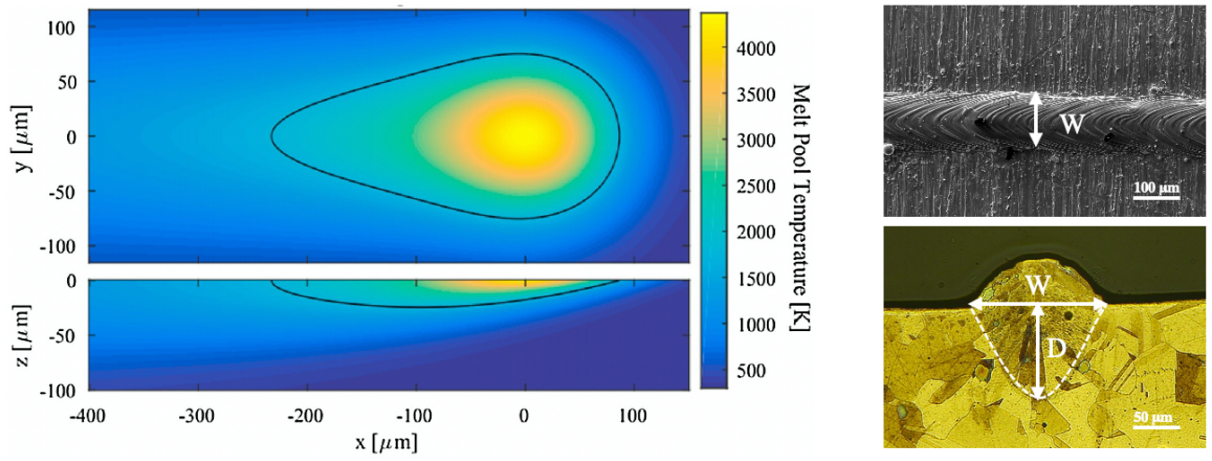


Figure 4.2: Left: A sample output of the E-T melt pool model showing the dimensions of a melt pool, where x, y, and z mean the length, width and depth of the melt region. Right: The representative single track top view SEM image and cross-section view OM image.

pool formation process. To further improve the performance of E-T model, statistical calibration is conducted to have the model predictions agree with experiments.

To calibrate the E-T model in the case of "unobservable" experimental data, we utilize melt pool geometry measurements of LPBF fabricated 52 $NiNb_5$ single tracks. Where we have both controllable inputs (processing parameters) and calibration parameters (unknown material properties) as model inputs, and melt pool width and depth as model outputs. We assume that all the 52 $NiNb_5$ melt pool width of the as-fabricated single tracks are measured, while only a few depth data were measured (in reality, all depth are measured). The melt pool width and depth are from the same melt pool geometry fabricated by the same manufacturing parameters. The melt pool is generated by the same thermal process.

Gas atomized Nickel-Niobium (Ni-5wt.%Nb) powder was provided by Nanoval GmbH & Co. KG and used to additively manufacture LPBF $NiNb_5$. Single tracks were printed using a 3D Systems ProX200 equipped with a fiber laser with a Gaussian profile $\lambda$ = 1070 nm, and beam size = 80 $\mu$m. Argon was used as inert protective atmosphere during fabrication. 52 tracks with 10mm length and spaced 1mm apart were printed on a $NiNb_5$ base plate with a layer thickness = 30$\mu$m. Three melt pool width measurements were taken from the top of as-fabricated tracks by SEM.

Three cross sections of the single tracks were wire cut using EDM, and these specimens were polished down to 0.25 $\mu$m with water-based diamond suspension polishing solutions. Kalling's Solution No.2 was used to etch the $NiNb_5$ single tracks to obtain optical micrographs. OM was carried out using a Keyence VH-X digital microscope equipped with a VH-Z100 wide range zoom lens. One depth measurement was taken using the VHX software from each cross section. The width and depth values are averaged from these measurements.

### 4.3 Hierarchical Gaussian Process (HGP) method

The hierarchical Gaussian process (HGP) method is developed to predict "unobservable" melt pool depth data. In the case of E-T model with two outputs, two levels of modeling structure is developed. The first level is a Gaussian process regression model (GPRM) which is the predictive model of melt pool width by inputs (laser power, scan speed, layer thickness, and laser beam size). In the first level of model, we have no missing data. In the second level, a hierarchical Gaussian process model (HGPM) is developed by leveraging the strong correlation of melt pool width and depth. The second level model is built on the paired width and depth data. Different amount of depth data is assumed "unobservable" which results in five different case studies.

#### 4.3.1 Gaussian Process Regression Model (GPRM)

GPR algorithm, also known as Kriging, is a powerful non-parametric approach whose flexibility and performance can handle huge amount of data [89, 90, 91]. In GPR, our goal is to calculate the covariance term given a training dataset $\mathbf{O} = (\boldsymbol{X}, \boldsymbol{y}^W)$ of $n$ training samples, where $\boldsymbol{x}_j$ are the input variables and $y_j^W$ is the corresponding continuous response variable. We model the response variable $y_j^W$ as a noise-version of the function value $f(\boldsymbol{x}_j)$ [92].

$$y_i^W \sim \mathcal{GP}(f(\boldsymbol{x}_j), \sigma_1^2) \tag{4.5}$$

where the distribution of noise is Gaussian $N(0, \sigma_1^2)$ with zero mean and variance $\sigma_1^2$.

$$\boldsymbol{f} = [f(\boldsymbol{x}_1), f(\boldsymbol{x}_2), ..., f(\boldsymbol{x}_n)]^T \tag{4.6}$$

$$\boldsymbol{f} \sim \mathcal{GP}(\boldsymbol{\mu}_1, \boldsymbol{K}) \tag{4.7}$$

$\boldsymbol{f}$ is modeled as a joint Gaussian distribution with mean $\boldsymbol{\mu}_1$ and covariance $\boldsymbol{K}$ (which is a kernel function over observations with hyperparameters). From the above definition, we can get the joint probability of the response variables and latent function variable $p(\boldsymbol{y^W}, \boldsymbol{f}) = p(\boldsymbol{y^W}|\boldsymbol{f})p(\boldsymbol{f})$ [93, 94]. The distribution of the latent function value $f(\boldsymbol{x^*})$ given $\boldsymbol{x^*}$ and training data $\mathbf{O}$ is also a Gaussian distribution, with mean and covariance given by:

$$mean(f(\boldsymbol{x^*})|\mathbf{O}) = \boldsymbol{k_{x^*X}}(\sigma_1^2\boldsymbol{I} + \boldsymbol{K_{XX}})^{-1}\boldsymbol{y}^W \tag{4.8}$$

$$Cov(f(\boldsymbol{x^*})|\mathbf{O}) = k_{x^*x^*} - \boldsymbol{k_{x^*X}}(\sigma_1^2\boldsymbol{I} + \boldsymbol{K_{XX}})^{-1}\boldsymbol{k_{Xx^*}} \tag{4.9}$$

where $\boldsymbol{k_{x^*X}} = k(\boldsymbol{x^*}, \boldsymbol{X})$ is a n-dimensional row vector of the covariance between $\boldsymbol{x^*}$ and the $n$ training samples. $\boldsymbol{K_{XX}} = k(\boldsymbol{X}, \boldsymbol{X})$ denotes the kernel function of training samples which are used to estimate the covariance function. Since $\boldsymbol{y}^{W*}$ is the related output, its predictive distribution is also Gaussian with mean mean($\boldsymbol{x^*}$) and covariance Cov($\boldsymbol{x^*}$) + $\sigma_1^2\boldsymbol{I}$.

Clearly, these recipes for prediction involve hyperparameters denoted as $\boldsymbol{\theta}$. In Bayesian approach, prior information about the unknown parameter $\theta$ is summarized in the form of a prior density $p(\boldsymbol{\theta})$. Then the posterior density for $\boldsymbol{\theta}$ given the training data is

$$p(\boldsymbol{\theta}|\boldsymbol{X}, \boldsymbol{Y^W}) \sim p(\boldsymbol{\theta})p(\boldsymbol{Y^W}|\boldsymbol{X}, \boldsymbol{\theta}) \tag{4.10}$$

where $p(\boldsymbol{Y^W}|\boldsymbol{X}, \boldsymbol{\theta})$ is the density function of an $n$-dimensional multivariate normal distribution

with zero mean and covariance matrix $(\sigma^2 \boldsymbol{I} + \boldsymbol{K_{XX}})$. Since the form of the covariance function is complicated in terms of $\boldsymbol{\theta}$, it is not feasible to carry out analytically inference based on the above posterior distribution. The most common Markov Chain Monte Carlo (MCMC) algorithm, Gibbs sampling, is used to estimate $\boldsymbol{\theta}$ [95, 96].

### 4.3.2 Hierarchical Gaussian Process Model (HGPM)

Next, we generate a HGPM to $\boldsymbol{Y}^W$ and $\boldsymbol{Y}^D$. $\boldsymbol{Y}^D$ is a continuous longitudinal response variable follows a Gaussian distribution in Equation 4.11.

$$y^L{}_i \sim \mathcal{GP}(g(y_i^W), \sigma_2^2) \tag{4.11}$$

$$\boldsymbol{g} = [g(y_1^W), g(y_2^W), ..., g(y_n^W)]^T \tag{4.12}$$

$$\boldsymbol{g} \sim \mathcal{GP}(\boldsymbol{\mu}_2, \boldsymbol{C}) \tag{4.13}$$

$g(y_i^W)$ follows a GP model with mean $\boldsymbol{\mu}_2$ and covariance $\boldsymbol{C}$. Therefore, the mean of posterior distribution for $\boldsymbol{y}^D$ given $\boldsymbol{Q} = (\boldsymbol{X}, \boldsymbol{y}^W, \boldsymbol{y}^D)$ is

$$E(\boldsymbol{y}^{D*}|\boldsymbol{Q}) = \boldsymbol{c_{y^{W*}y^{W*}}}(\sigma_2^2 \boldsymbol{I} + \boldsymbol{C})^{-1} \boldsymbol{y}^D \tag{4.14}$$

where $\boldsymbol{c_{y^{W*}y^{W*}}} = Cov(\boldsymbol{x^*}) + \sigma_1^2 \boldsymbol{I}$ that is observed from GPRM. $\boldsymbol{C} = k(\boldsymbol{y}^W, \boldsymbol{y}^W)$ is the kernel function of training inputs. These terms can also estimated by Gibbs sampling method. So far, we have implemented the relationship or dependence between system inputs and width data into the prediction of depth data. This hierarchical structure allows us to fully model the correlation of system inputs and sensor data with no missing values [97].

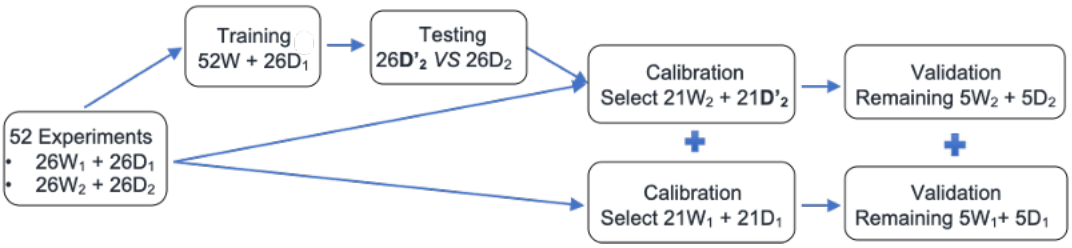


Figure 4.3: The splitting strategy of overall melt pool data for case 1.

### 4.3.3 Results and Discussion

#### *4.3.3.1 Prediction Results*

In case 1, we assume observed 26 melt pool depth data. These amount of data is split following Figure 4.3 to train and test the HGP method, then to calibrate and validate the surrogate model of E-T. The data used for Bayesian calibration is 80% of all the observed melt pool width data, and the 80% of partially observed melt pool depth data combining the 80% of depth predictions in model testing step. The 26 melt pool depth data are selected completely random. The cross validation results are shown in Figure 4.4 [98], and the model performance is shown in Figure 4.5. In addition, two different errors are computed, mean absolute error (MAE) is 6.3$\mu$m and mean absolute percentage error (MAPE) is 12.52%.

With the same amount of 26 melt pool depth data selected, case 1.1 select these data with low measurement variability to test which selection method is better: random selection or by the data property. The model performance is shown in Figure 4.6. The mean absolute error (MAE) is 8.14$\mu$m and mean absolute percentage error (MAPE) is 12.89%. Other cases were also processed by the HGP method with randomly selected depth data, the testing results of different cases are summarized as below:

- Case 1: Melt pool depth training data size is 26, testing data size = 26, MAPE = 12.52%.
- Case 2: Melt pool depth training data size is 13, testing data size = 39, MAPE = 17.45%.
- Case 3: Melt pool depth training data size is 7, testing data size = 45, MAPE = 24.82%.

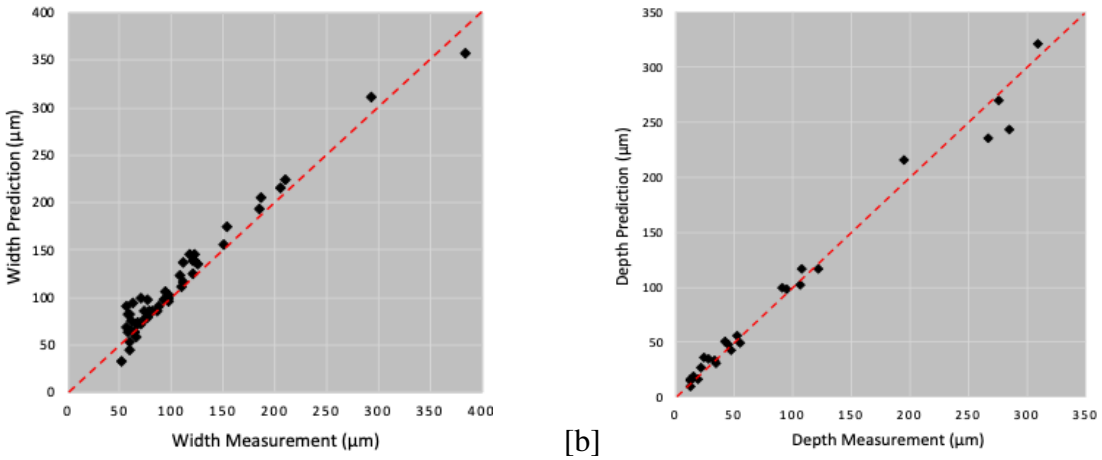


[a] [b]

Figure 4.4: (a) Cross validation results of the $Y^W$ training dataset for 1st level HGPM. (b) Prediction of the $Y^D$ testing dataset for the 2nd level HGPM.

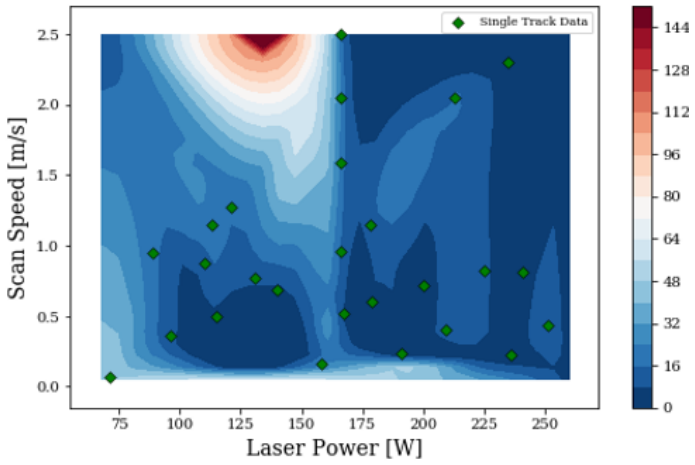


Figure 4.5: The absolute percentage error for the case where the 26 melt pool depth data are randomly selected.

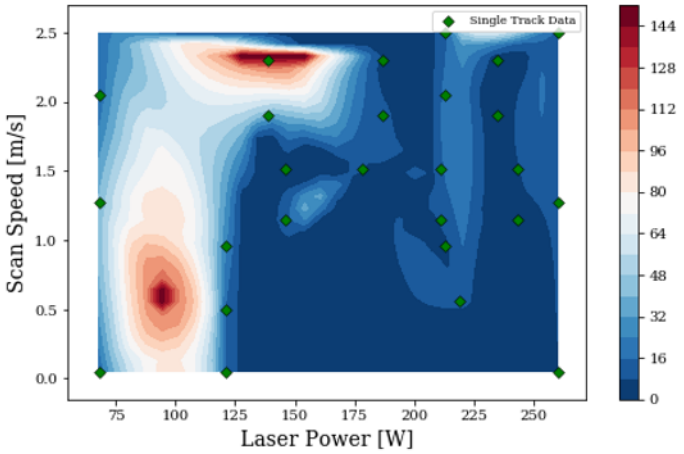


Figure 4.6: The absolute percentage error the case where the 26 depth data are in low measurement variability

- Case 4: Melt pool depth training data size is 20, testing data size = 32, MAPE = 15.83%.
- Case 5: Melt pool depth training data size is 32, testing data size = 20, MAPE = 10.42%.

#### *4.3.3.2 Calibration Results*

Here, the predicted melt pool depths are combined with experimental observations to conduct statistical calibration following the MVCalib method. The above five cases have different calibration and validation data size. For each case, MAPE of 52 depth predictions by the calibrated model are 11.83%, 14.75%, 16.21%, 13.42%, 11.05%.

The comparison of the multivariate Bayesian calibration by full melt pool width observations, 26 melt pool depth observations and 26 depth predictions to (1) univariate Bayesian calibration using only melt pool width observations; (2) multivariate Bayesian calibration by full melt pool observations was conducted. The 3D heat maps of calibrated melt pool width and depth predictions are shown below [99]. Figure 4.7 shows the prediction results of multivariate model calibration by partial melt pool depth predictions. Figure 4.8 shows the prediction results of univariate model calibration. This univariate calibration was conducted separately for melt pool width and depth. The width calibration is straight forward by following Kennedy and O'Hagan's Bayesian calibration framework [51]. The melt pool width prediction if derived from $W_{pred} = \hat{y_W} + \sigma_W + \epsilon_W$. When

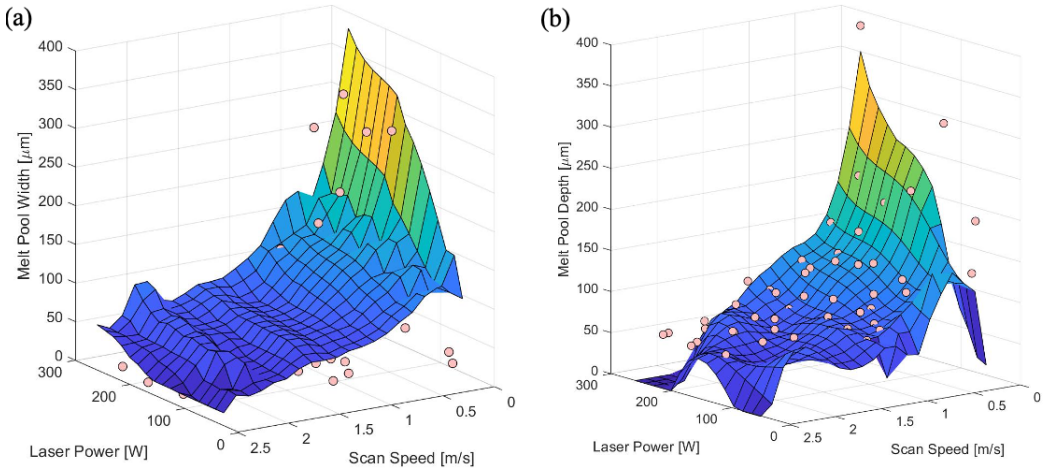


Figure 4.7: The prediction results of multivariate model calibration by partial melt pool depth predictions for (a) melt pool width, MAPE = 7.98% (b) melt pool depth, MAPE = 11.83%. The experimental observations are given by the dots in each map.

making depth predictions with the univariate calibrated model, we borrowed the model discrepancy function and measurement error term from melt pool width, where we have $D_{pred} = \hat{y_D} + \sigma_W + \epsilon_W$. $\hat{y_D}$ is the posterior mean estimates of melt pool depth from surrogate model. Figure 4.9 shows the prediction results of multivariate model calibration by full melt pool observations.

By looking at the comparison results, the two-stage model calibration system proposed by us provide promising calibration results. The MAPE of calibrated model prediction by our method is 11.83% which is a little bit larger than the general multivariate calibration MAPE 8.05%. While, we saved about $2000 (cost for preparing the sample, machine, material, etc) and one week of labor time for conducting the melt pool characterization [100, 101]. The earning from measuring 26 instead of 52 melt pool depth data is greatly huge than the sacrifice in calibration accuracy. Besides, all the five cases processed by our two-stage model calibration system perform much better than the univariate calibration on predicting melt pool depth.

### 4.4 Calibrated Bayesian Multiple Imputation (CBMI) Method

In the statistics world, Bayesian methodology models the data and prior distribution for unknown parameters and base inferences for unknowns on posterior distributions. There is no prescription for choosing the model and prior distribution. However, certain "reference" prior distri-

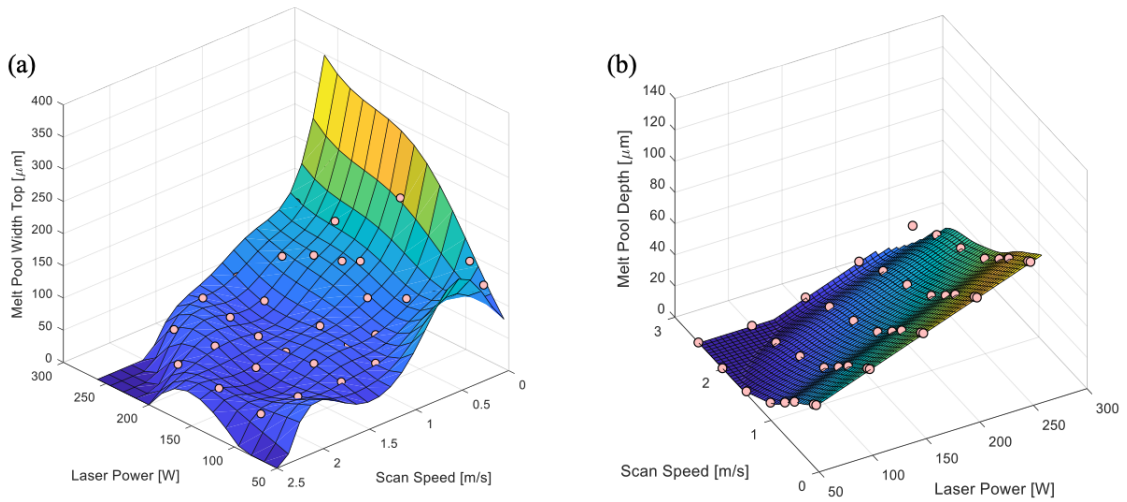


Figure 4.8: The prediction results of univariate model calibration for (a) melt pool width, MAPE = 1.6% (b) melt pool depth, MAPE = 48.35%. The experimental observations are given by the dots in each map.

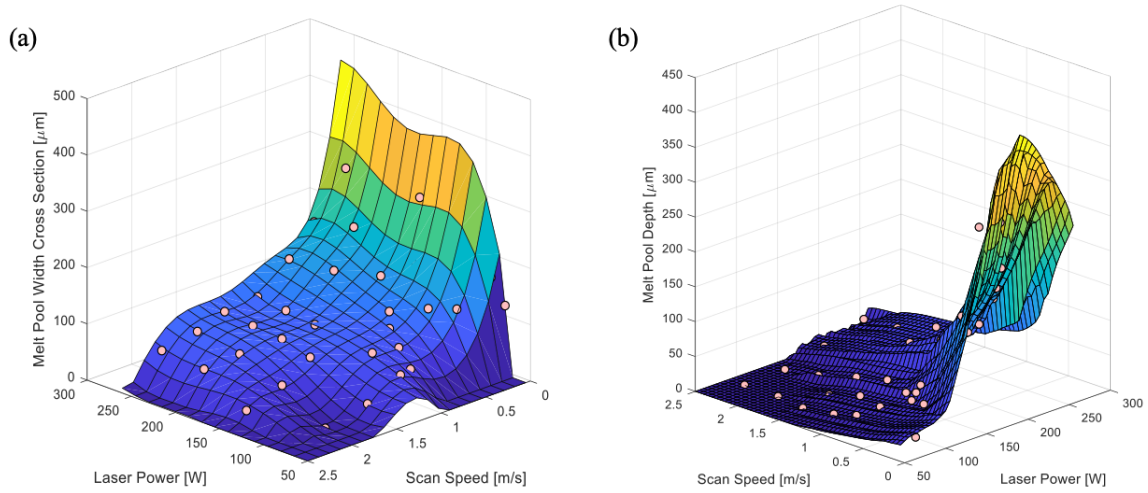


Figure 4.9: The prediction results of multivariate model calibration by full melt pool observations for (a) melt pool width, MAPE = 6.73%. (b) melt pool depth, MAPE = 8.05%. The experimental observations are given by the dots in each map.

butions for complete data problems can be expected to produce good frequency properties when applied to missing data problems [102, 103]. Therefore, the proposed method aims to deal with the missing data problems in the second stage of MVCalib method. Such that the assumptions of model and prior distributions are referred by the calibration case with full data. Our target is to estimate the calibration parameters and hyperparameters through the calibrated Bayesian multiple imputation (CBMI) method for the MVN calibration model.

### 4.4.1 Expectation–maximization (EM) Algorithm

In missing data problems, let $\boldsymbol{Y}_{n\times q} = [\boldsymbol{Y}_{obs}, \boldsymbol{Y}_{mis}]$ represents a data matrix with n rows (cases) and q columns (output variables). And $\boldsymbol{M} = (m_{i,j})_{n\times q}$ is the missing-data indicator matrix. $m_{i,j} = 0$, if $y_{i,j}$ is observed; $m_{i,j} = 1$, if $y_{i,j}$ is missing. A full parametric model factors the distribution of $(\boldsymbol{Y}, \boldsymbol{M})$ into distribution $f(\boldsymbol{Y}|\boldsymbol{\phi})$ for $\boldsymbol{Y}$ indexed by unknown parameters $\boldsymbol{\phi}$, and a distribution $f(\boldsymbol{M}|\boldsymbol{Y}, \boldsymbol{\xi})$ for $\boldsymbol{M}$ given $\boldsymbol{Y}$ indexed by unknown parameter $\boldsymbol{\xi}$. Likelihood methods can be directly applied to missing data problems [104, 105]. Maximum likelihood (ML) method is a likelihood method, with associated large sample standard errors based on the information; to add a prior distribution and compute the posterior distribution of the parameters. However, ML algorithm for complex problems is computationally expensive given limits of computation resources due to the huge amount of iterative runs. Although progress was made for normal models. The development of expectation–maximization (EM) algorithm enables dealing with several important multivariate models, including the multivariate normal model with missing values [106, 107, 108, 109].

In the ML method, expectation–maximization (EM) algorithm establishes a connection between the complex observed data likelihood and the simpler complete data likelihood, thereby facilitating this computational task. The main idea is to iterate between the draws of missing values and the draws of unknown parameters. The draws of missing values replace expected values of functions of the missing values in Expectation-step (E-step); and the draws of unknown parameters replace maximization over the parameters $\boldsymbol{\phi}$ the Maximization-step (M-step). Here, the estimate of $\boldsymbol{Y}_{mis}$ is to find the best $\boldsymbol{\phi}$. Therefore, it is not the best $\boldsymbol{Y}_{mis}$ estimation, but the best fitted value for $\boldsymbol{\phi}$ imputation.

In our case, for $\boldsymbol{\phi}^{d,t}$, the initial calibration parameters $\boldsymbol{\theta}$ are taking by the middle values of suggested upper and lower boundaries of sampling to avoid bias. Other hyperparameters take 1 as initial values. Initial $\boldsymbol{Y}_{mis}^{d,t}$ are taking the half of paired melt pool width values. By the initial estimation $(\boldsymbol{\phi}^{d,t}, \boldsymbol{Y}_{mis}^{d,t})$, the E-step is to draw new values of the missing data from loglikelihood distribution shown as the following;

$$\boldsymbol{Y}_{mis}^{d,t+1} \sim P(\boldsymbol{Y}_{mis}|\boldsymbol{Y}_{obs}, \boldsymbol{\phi}^{d,t}) \tag{4.15}$$

E-step is mainly to compute the expected complete-data loglikelihood with estimated $\boldsymbol{Y}_{mis}$ in iterations.

$$Q(\boldsymbol{\phi}|\boldsymbol{Y}_{obs}, \boldsymbol{\phi}^{d,t}) = \int log f(\boldsymbol{Y}_{obs}, \boldsymbol{Y}_{mis}; \boldsymbol{\phi}) f(\boldsymbol{Y}_{mis}|\boldsymbol{Y}_{obs}, \boldsymbol{\phi} = \boldsymbol{\phi}^{t}) d\boldsymbol{Y}_{mis} \tag{4.16}$$

The M-step determines $\boldsymbol{\phi}^{d,t+1}$ by maximizing this expected "complete-data" loglikelihood as the following;

$$Q(\boldsymbol{\phi}^{t+1}|\boldsymbol{Y}_{obs}, \boldsymbol{\phi}^{t}) \geq Q(\boldsymbol{\phi}|\boldsymbol{Y}_{obs}, \boldsymbol{\phi}^{t}) \tag{4.17}$$

From this, we observe the best estimated $\phi$ in iteration t+1. It means that when t tends to infinity, this sequence converges to a draw from joint posterior distribution of $\boldsymbol{\phi}$ and $\boldsymbol{Y}_{mis}$.

$$\boldsymbol{\phi}^{d,t+1} \sim P(\boldsymbol{\phi}|\boldsymbol{Y}_{obs}, \boldsymbol{Y}_{mis}^{d,t+1}) \tag{4.18}$$

The imputed $\boldsymbol{Y}_{mis}$ aims to find the best fitted $\boldsymbol{\phi}$. Hence, its value is not accurate that can not be used as the estimation of missing data. The Gibbs' sampling method and other MCMC methods gains the computing power to simulate direct draws from a target distribution using iterative algorithms.

### 4.4.2 Bayesian Multiple Imputation (BMI)

Instead of filling in a single value for each missing value, a multiple imputation (MI) procedure replaces each missing value with a set of plausible values that represent the uncertainty about the right value to impute [110, 111, 112]. MI does not attempt to estimate each missing value through simulated values but rather to represent a random sample of the missing values. This process results in valid statistical inferences that properly reflect the uncertainty due to missing values; for example, valid confidence intervals for parameters.

Because of multiple draws of $\boldsymbol{Y}_{mis}^{d}$ to achieve the best imputation of $\boldsymbol{\phi}$ , when it converges after large enough iterations, there will be more than one multiply-imputed data sets, $D > 1$. Because of the multiple imputations, we will use combining rules for inferences that propagate imputation uncertainty [113]. This idea is related to the posterior distribution of observed data.

$$P_{full}(\boldsymbol{\phi}, \boldsymbol{\xi}|\boldsymbol{Y}_{obs}, \boldsymbol{M}) \propto \pi(\boldsymbol{\phi}, \boldsymbol{\xi}) \times L(\boldsymbol{\phi}, \boldsymbol{\xi}|\boldsymbol{Y}_{obs}, \boldsymbol{M}) \tag{4.19}$$

$L(\boldsymbol{\phi}, \boldsymbol{\xi}|\boldsymbol{Y}_{obs}, \boldsymbol{M})$ is the likelihood of the observed data, obtained by integrating out the missing values of the complete-data likelihood:

$$f(\boldsymbol{Y}_{obs}, \boldsymbol{M}|\boldsymbol{\phi}, \boldsymbol{\xi}) = \int f(\boldsymbol{Y}_{obs}, \boldsymbol{Y}_{mis}|\boldsymbol{\phi}) f(\boldsymbol{M}|\boldsymbol{Y}_{obs}, \boldsymbol{Y}_{mis}, \boldsymbol{\xi}) d\boldsymbol{Y}_{mis}$$

The above equations is the "complete-data" posterior distribution. That would have been obtained if we had observed the missing data $Y_{mis}$, namely,

$$P(\boldsymbol{\phi}, \boldsymbol{\xi}|\boldsymbol{Y}_{obs}, \boldsymbol{Y}_{mis}) \propto \pi(\boldsymbol{\phi}, \boldsymbol{\xi}) \times L(\boldsymbol{\phi}, \boldsymbol{\xi}|\boldsymbol{Y}_{obs}, \boldsymbol{Y}_{mis}) \tag{4.20}$$

Relate the above equation to a simpler posterior distribution $\boldsymbol{\phi}$ ignores the missing data, and utilize

the likelihood given the observed data $\boldsymbol{Y}_{obs}$:

$$\begin{aligned} P_{ign}(\boldsymbol{\phi}|\boldsymbol{Y}_{obs}) &\propto \pi(\boldsymbol{\phi}) \times L(\boldsymbol{\phi}|\boldsymbol{Y}_{obs}), \\ L(\boldsymbol{\phi}|\boldsymbol{Y}_{obs}) &= \int f(\boldsymbol{Y}_{obs}, \boldsymbol{Y}_{mis}|\boldsymbol{\phi}) dY_{mis} \end{aligned} \tag{4.21}$$

By the standard probability theory, we get:

$$P_{ign}(\boldsymbol{\phi}|\boldsymbol{Y}_{obs}) = \int P(\boldsymbol{\phi}|\boldsymbol{Y}_{obs}, \boldsymbol{Y}_{mis}) P(\boldsymbol{Y}_{mis}|\boldsymbol{Y}_{obs}) d\boldsymbol{Y}_{mis} \tag{4.22}$$

The above equation implies that the posterior distribution $P_{ign}(\boldsymbol{\phi}|\boldsymbol{Y}_{obs})$ can be simulated by first drawing the missing values $\boldsymbol{Y}_{mis}^{d}$, from the posterior distribution, $P(\boldsymbol{Y}_{mis}, \boldsymbol{Y}_{obs})$. The $\boldsymbol{Y}_{mis}^{d}$ is imputed to complete the data set, and then drawing $\boldsymbol{\phi}$ from its "completed-data" posterior distribution, $P(\boldsymbol{\phi}|\boldsymbol{Y}_{obs}, \boldsymbol{Y}_{mis}^{d})$. That is,

$$P_{ign}(\boldsymbol{\phi}|\boldsymbol{Y}_{obs}) \approx \frac{1}{D} \sum_{d=1}^{D} P(\boldsymbol{\phi}|\boldsymbol{Y}_{obs}, \boldsymbol{Y}_{mis}^{(d)}) \tag{4.23}$$

The above can be replaced when its mean and variance are adequate summaries of the posterior distribution. By the equations:

$$E(\boldsymbol{\phi}|\boldsymbol{Y}_{obs}) = E[E(\boldsymbol{\phi}|\boldsymbol{Y}_{obs}, \boldsymbol{Y}_{mis})|\boldsymbol{Y}_{obs}] \tag{4.24}$$

and

$$Var(\boldsymbol{\phi}|\boldsymbol{Y}_{obs}) = E[Var(\boldsymbol{\phi}|\boldsymbol{Y}_{obs}, \boldsymbol{Y}_{mis})|\boldsymbol{Y}_{obs}] + Var[E(\phi|\boldsymbol{Y}_{obs}, \boldsymbol{Y}_{mis})|\boldsymbol{Y}_{obs}] \tag{4.25}$$

Also, we can approximate the above equations by using draws of $\boldsymbol{Y}_{mis}$ yields,

$$E(\boldsymbol{\phi}|\boldsymbol{Y}_{obs}) \approx \overline{\boldsymbol{\phi}} = \frac{1}{D} \sum_{d=1}^{D} \overline{\boldsymbol{\phi}}^{(d)} \tag{4.26}$$

where $\overline{\boldsymbol{\phi}}^{(d)} = E(\boldsymbol{\phi}|\boldsymbol{Y}_{obs}, \boldsymbol{Y}_{mis}^{(d)})$ is the posterior mean of $\boldsymbol{\phi}$ from the $d$th completed data set, and

$$Var(\boldsymbol{\phi}|\boldsymbol{Y}_{obs}) \approx \overline{V} + (1 + \frac{1}{D})B \tag{4.27}$$

where $\overline{V} = D^{-1}\sum_{d=1}^{D} Var(\phi|\boldsymbol{Y}_{obs}, \boldsymbol{Y}_{mis}^{(d)})$ is the average of the complete-data posterior covariance matrix of $\boldsymbol{\phi}$ calculated for the $d$th data set $(\boldsymbol{Y}_{obs}, \boldsymbol{Y}_{mis}^{(d)})$, $B = \sum_{d=1}^{D}(\overline{\boldsymbol{\phi}}^{(d)} - \overline{\boldsymbol{\phi}})(\overline{\boldsymbol{\phi}}^{(d)} - \overline{\boldsymbol{\phi}})^T/(D-1)$ is a covariance matrix (called between-imputation covariance) to improve the approximation for small $D$. $(1+1/D)B$ in Equation 4.27 estimates the variance by single imputation methods from imputation uncertainty.

### 4.4.3 Calibrated Bayesian Multiple Imputation (CBMI) method

After sketched the ME and BMI theory for the analysis of data with missing values that underlies the method, I now describe the application for the MVN calibration model [114, 115]. In our case, it is to estimate the unknown parameters in the calibration model of Equation 4.2 in the MVCalib method. $\boldsymbol{Y}^E$ is the melt pool geometry measurements, following a MVN distribution [116]. So,

$$\boldsymbol{Y}_{n\times 2}^{E} = [\boldsymbol{Y}_{obs}, \boldsymbol{Y}_{mis}] \tag{4.28}$$

represents a two-output variable matrix with n rows. A full parametric model factors the distribution of $(\boldsymbol{Y}_{n\times 2}^{E}, \boldsymbol{M}_{n\times 2})$ into distribution $f(\boldsymbol{Y}^E|\boldsymbol{\phi})$ for $\boldsymbol{Y}^E$ indexed by unknown parameters $\boldsymbol{\phi}$.

Given the current draw $\boldsymbol{\phi}^{d,t} = (\boldsymbol{\mu}^{d,t}, \boldsymbol{\Sigma}^{d,t})$ ($d$: draw from distribution, $t$: $t^{th}$ iterations) of the parameters, missing values are drawn as

$$\begin{aligned} \boldsymbol{y}_{mis,i}^{d,t+1} &\sim P(\boldsymbol{y}_{mis,i}|\boldsymbol{y}_{obs,i}, \boldsymbol{\phi}^{d,t}) \\ \boldsymbol{\phi}^{d,t+1} &\sim P(\boldsymbol{\phi}|\boldsymbol{y}_{obs,i}, \boldsymbol{y}_{mis,i}^{d,t+1}) \\ i &= 1, 2, ..., n \end{aligned} \tag{4.29}$$

which is the multivariate normal distribution of the missing variables given the observed variables in observation $i$, with parameters that are functions of $\boldsymbol{\phi}^{dt}$. New parameters $\boldsymbol{\phi}^{d,t+1}$ are drawn from

the posterior distribution given the filled-in data, which is a standard Bayesian problem, namely,

$$\boldsymbol{\Sigma}^{d,t+1} \sim P(\boldsymbol{\Sigma}|P(\boldsymbol{y}_{obs}, \boldsymbol{y}_{mis}^{d,t+1}) \tag{4.30}$$

$$(\boldsymbol{\mu}^{d,t+1}|\boldsymbol{\Sigma}^{d,t+1}) \sim P(\boldsymbol{\mu}|\boldsymbol{\Sigma}^{d,t+1}, P(\boldsymbol{y}_{obs}, \boldsymbol{y}_{mis}^{d,t+1}) \tag{4.31}$$

where the Equation 4.30 is a draw from an inverse Wishart distribution [117], and the Equation 4.31 is a draw from MVN distribution. Equations 4.29 to 4.31 are closely related to the EM algorithm for ML estimation, except that they lead to draws from the posterior distribution. First, EM is programmed in Python, and corrected by checking the increased likelihood with each iteration, and then the EM algorithm is converted into the Gibbs sampling by replacing the conditional means of the missing data in draws of Equation 4.29 by E-step, and the complete-data ML parameters in draws of Equation 4.30 and Equation 4.31 by M-step.

When the posterior mean and variance are adequate summaries of the posterior distribution, $\boldsymbol{\phi}^{d,t+1}$ can be replaced by $(\boldsymbol{\mu}^{d,t+1}, \boldsymbol{\Sigma}^{d,t+1})$. Therefore, as the iteration goes to infinity, we will have a stable estimation of $(\boldsymbol{\mu}^{d,t}, \boldsymbol{\Sigma}^{d,t}) \rightarrow \boldsymbol{\phi}^{d,t} \rightarrow \boldsymbol{y}_{mis,i}^{d,t+1} \rightarrow \boldsymbol{\phi}^{d,t+1}$. Then, the estimated $\boldsymbol{\phi}_{cal} = (\boldsymbol{\theta}^*, \boldsymbol{r}_{\boldsymbol{\delta}}^*, \boldsymbol{\sigma}_{\boldsymbol{\delta}}^*, \boldsymbol{\psi}^*)$ from CBMI will be applied to the predictive distribution model Equation 4.3.

### 4.4.4 Results and Discussion

For this case study, we apply the presented CBMI method to a real-world problem related to the analytical melt pool model of LPBF processes, where only 26 of the melt pool depth data is observed. Systematic calibration and uncertainty quantification of model parameters is a vital task for robust predictions and usability of the models to guide the design and optimization [118]. The current case study demonstrates how our method is effective when one seeks to calibrate a multivariate model that has unobservable experimental data.

We employed the CBMI method to estimate the calibration parameters (absorptivity, thermal conductivity, and specific heat capacity) $\boldsymbol{\theta}$ in the two-stage multivariate calibration method. The calibration model Equation 4.2 follows a MVN distribution with calibration parameter $\boldsymbol{\theta}$ and hyper-parameters $\boldsymbol{r}_{\boldsymbol{\delta}}, \boldsymbol{\sigma}_{\boldsymbol{\delta}}, \boldsymbol{\psi}$. Instead of estimating the values of these parameters $\boldsymbol{\phi}_{\boldsymbol{cal}}$ through statistical

calibration, an imputation approach that can handle the case of missing data used to estimate their value. The following prior distributions were used:

$$\theta_i \sim Uniform(\alpha_i, \beta_i) \tag{4.32}$$

$$r_{\delta_i} \sim Log - Normal(\alpha = 0, \beta = 1/4) \tag{4.33}$$

$$\sigma_{\delta_i}, \psi_i \sim Inverse - Gamma(\alpha = 2, \beta = 1) \tag{4.34}$$

where $(\alpha_i, \beta_i)$ indicate the lower and upper bounds for the uniform distributions as recommended by the domain expert. For the roughness parameters, $r_{\delta_i}$ log-normal priors were used to ensure positive. For the variance terms $\sigma_{\delta_i}$ and $\psi_i$, inverse gamma priors were selected because they represent conjugate priors for the multivariate normal likelihood function in our model. Note that the priors for the calibration parameters $\boldsymbol{\theta}$ are all uniform and hence non-informative to avoid any bias in estimation. Using Gibbs Sampling, the posterior distributions of calibration parameters and hyperparameters $\boldsymbol{\phi_{cal}}$ were generated after 25000 iterations with 25% burn-in period and thinning every fifth sample. Figure 4.10 shows the histograms and kernel density estimates of the truncated posterior distributions for the parameters $\boldsymbol{\phi_{cal}}$.

By the posterior estimates of the truncated distribution, we can compute the posterior mean and variance estimates for $\boldsymbol{\phi_{cal}}$. The posterior mean is a sufficient estimation of the calibration parameters as shown in Figure 4.11. Using the estimation of the calibration parameters, we can predict the melt pool width and depth for the entire printability map. To compare the imputed and calibrated parameter values, we conduct MVCalib method with the full 52 experimental data. The value of calibration parameters by MVCalib are absorptivity = 0.51, thermal conductivity = 70.4 W/m*K, and specific heat capacity = 636.19 J/kg*K. In conclusion, the imputed values are in small errors of the MVCalib method.

Next, 2-fold cross-validation (CV) is conducted to evaluate the accuracy of MVN distributed calibration model with imputed parameter values. The CV results of the 26 observed melt pool depth and paired width are shown in Figure 4.12. In the plots, the horizontal axes represent the

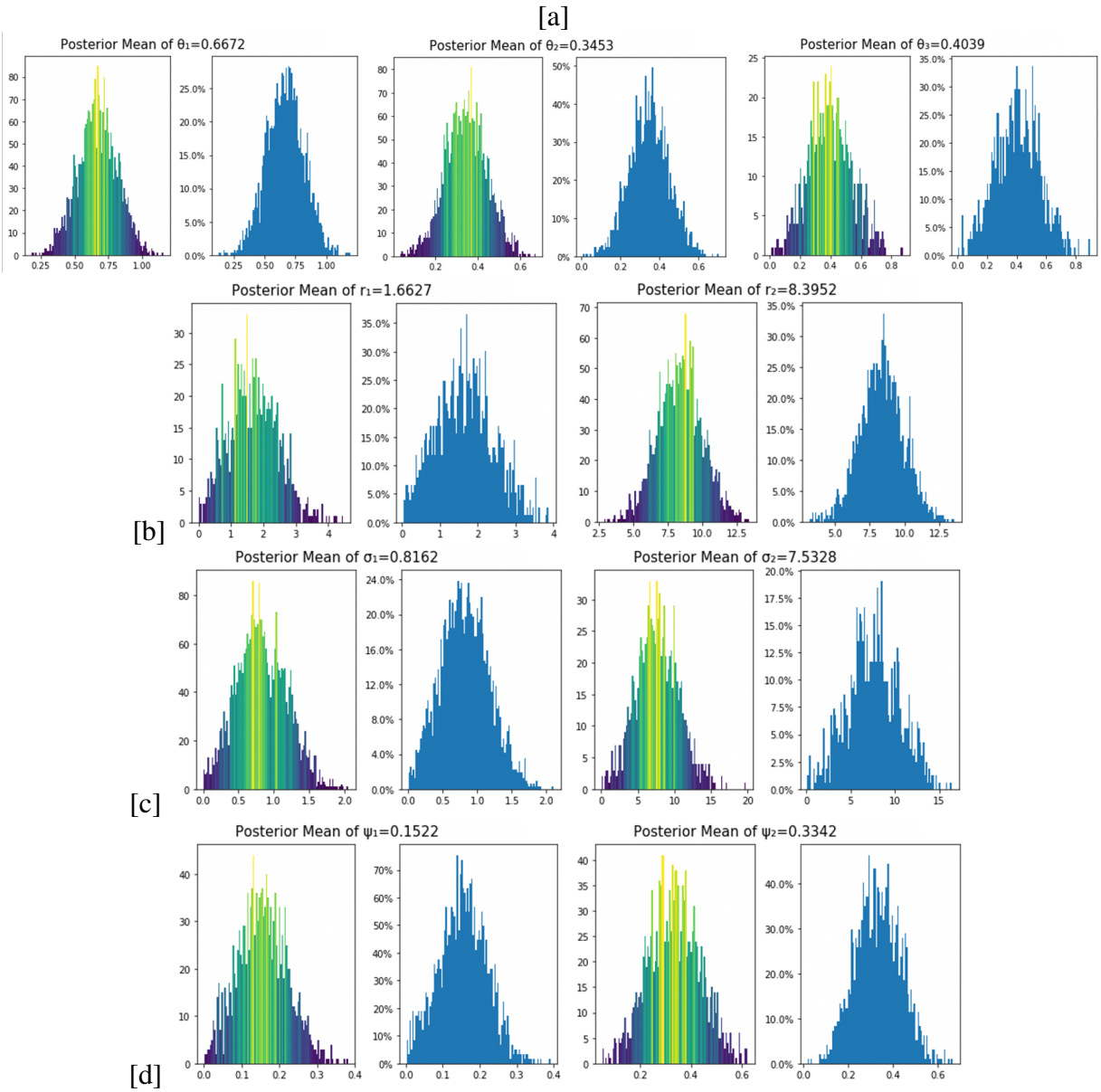


Figure 4.10: The histograms and kernel density estimates of the truncated posterior distributions for the calibration parameters and hyperparameters.

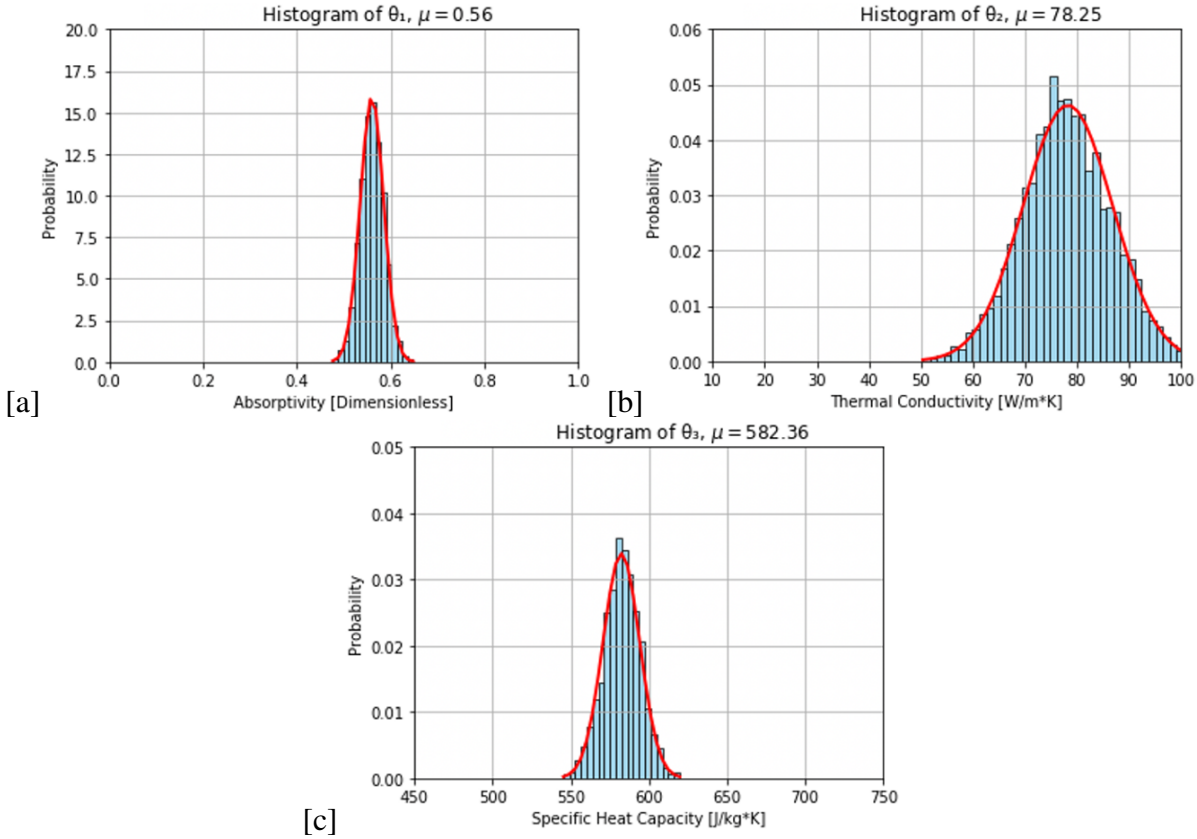


Figure 4.11: The histograms and kernel density estimates of the posterior distributions for the calibration parameters $\boldsymbol{\theta}$.

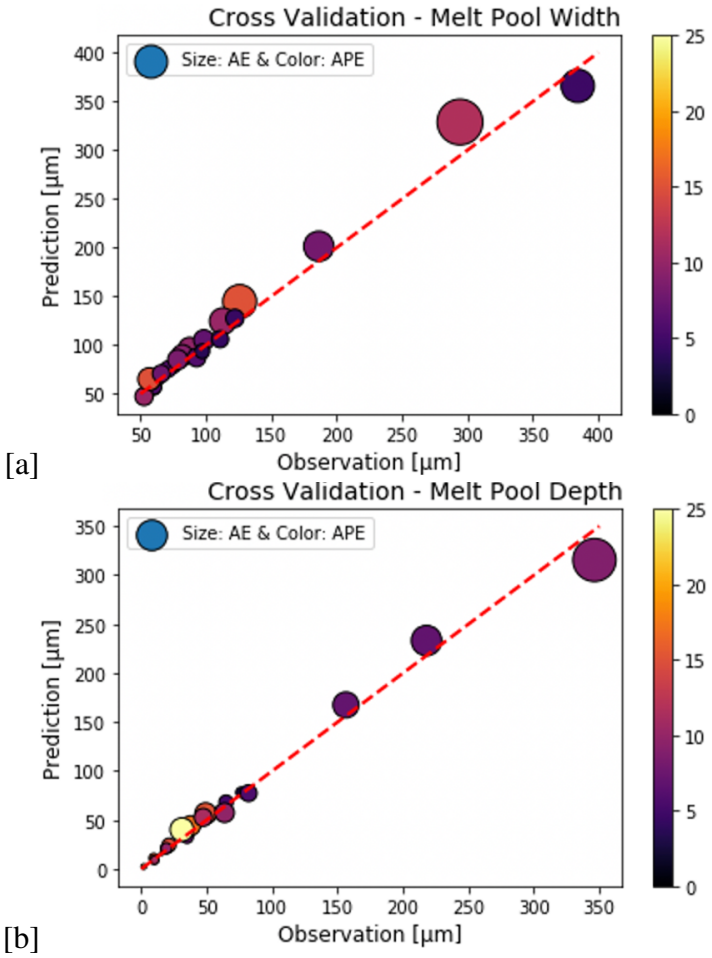


Figure 4.12: The cross-validation result of the calibration model for (a) melt pool width, and (b) melt pool depth. In the plot, the horizontal and vertical axes represent the experimental observation and predicted melt pool data separately. The size and color of the dots represent AE and APE of each prediction.

experimental observation of melt pool geometry, while the vertical axes show the predicted outputs using the calibration model. The size and color of the dots represent the absolute error (AE) and absolute percentage error (APE) of each prediction. The red dash line represents the ideal case with model predictions are in full agreement with experimental results. It can be seen that the predictive performance of the surrogate models are satisfactory. Also, the MAPE of width and depth are 9.77% and 7.34% which indicate satisfactory performance.

To test the predictive model, the assumed "unobserved" 26 melt pool depth and paired width values are predicted. The test results are shown in Figure 4.13. The MAPE are also calculated

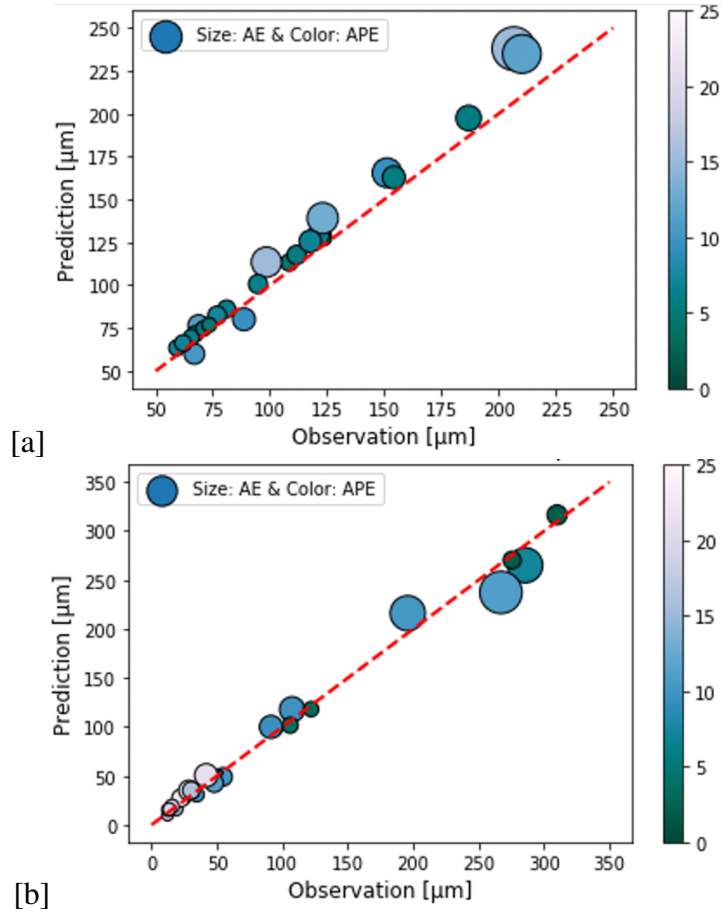


Figure 4.13: The test results of the calibrated E-T model for (a) melt pool width, and (b) melt pool depth. In the plot, the horizontal and vertical axes represent the experimental observation and predicted melt pool data separately. The size and color of the dots represent AE and APE of each prediction.

and displayed in Table 4.1 to compare with the benchmark MVCalib method by full 52 width and depth observations. By then, we have validated that the CBMI method is an efficient and effective in calibrating computer model with missing experimental observations. The predictive model will then substitute the original E-T model for melt pool width and depth simulations, named as calibrated E-T model. The heat maps represent the APE of the 52 experimental width and depth observations by the calibrated E-T model are plotted in Figure 4.14.

In addition to the case of missing 26 depth data, another four cases under different assumptions of "unobservable" melt pool depth measurements are also computed by the CBMI method. Case 1

Table 4.1: The comparison of CBMI and MVCalib method in the MAPE of testing results.

| MAPE | Melt Pool Width | Melt Pool Depth |
|---|---|---|
| MVCalib Method | 7.03% | 9.28% |
| CBMI Method | 7.71% | 11.36% |

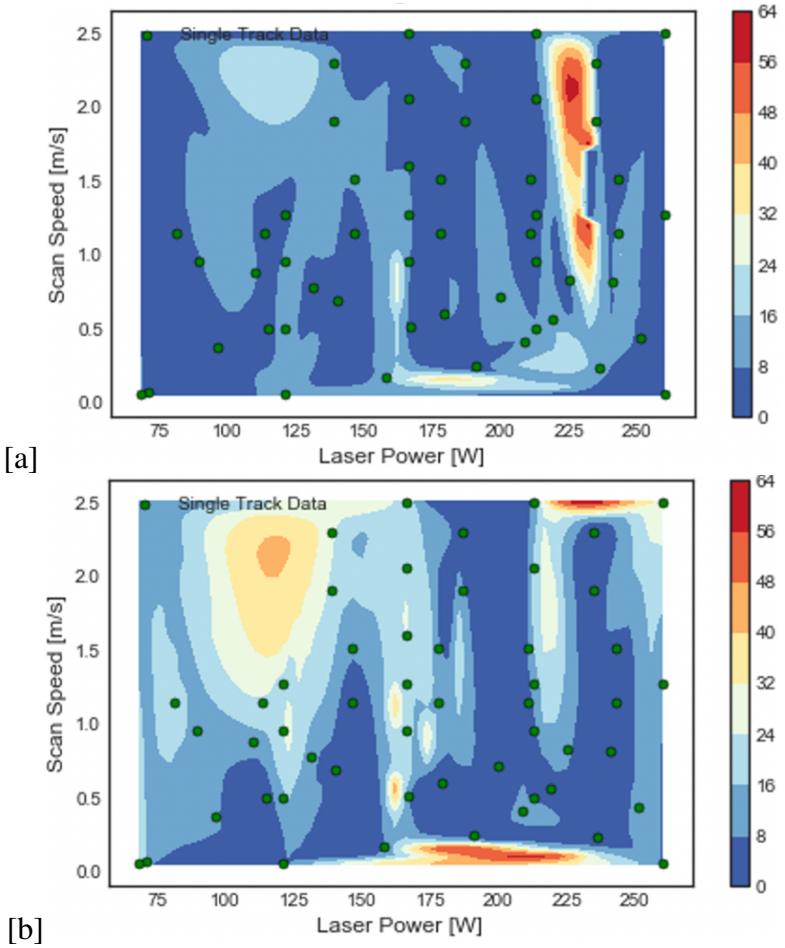


[a]

[b]

Figure 4.14: The heat maps represent the APE of the 52 experimental observations by the calibrated E-T model in (a) melt pool width, and (b) melt pool depth.

represents the MVCalib method on full 52 width and depth experimental data. Case 2-6 represents the CBMI method on full width and missing depth data.

- Case 1: The amount of observable melt pool width and depth data is 52 and 52.
- Case 2: The amount of observable melt pool width and depth data is 52 and 32.
- Case 3: The amount of observable melt pool width and depth data is 52 and 26.
- Case 4: The amount of observable melt pool width and depth data is 52 and 20.
- Case 5: The amount of observable melt pool width and depth data is 52 and 13.
- Case 6: The amount of observable melt pool dwidth and depth data is 52 and 7.

The MAPE of CV results and testing results are plotted in Figure 4.15 to compare how the amount of missingness in depth influences the calibrated E-T model performance. Overall, the less the missingness the better the calibration results. Because the more information is employed in the EM algorithm for estimating the mean and variance of calibration parameters and hyperparameters, the more accurate these parameters are imputed in Bayesian method.

The purpose of conducting statistical calibration is to make sure the melt pool model predictions are in the agreement with experimental results to accelerate the study of printability. Therefore, we plotted the finalized printability maps by (a) MVCalib method with full melt pool data, (b) CBMI method with full width data and half depth data, and (c) CBMI method with full width data and 1/4 depth data in Figure 4.16. As we see, Figure 4.16(a) has the most conservative sub-regions. The two plots generated by the calibrated E-T model of CBMI method also reasonably present the defects and good regions in the map.

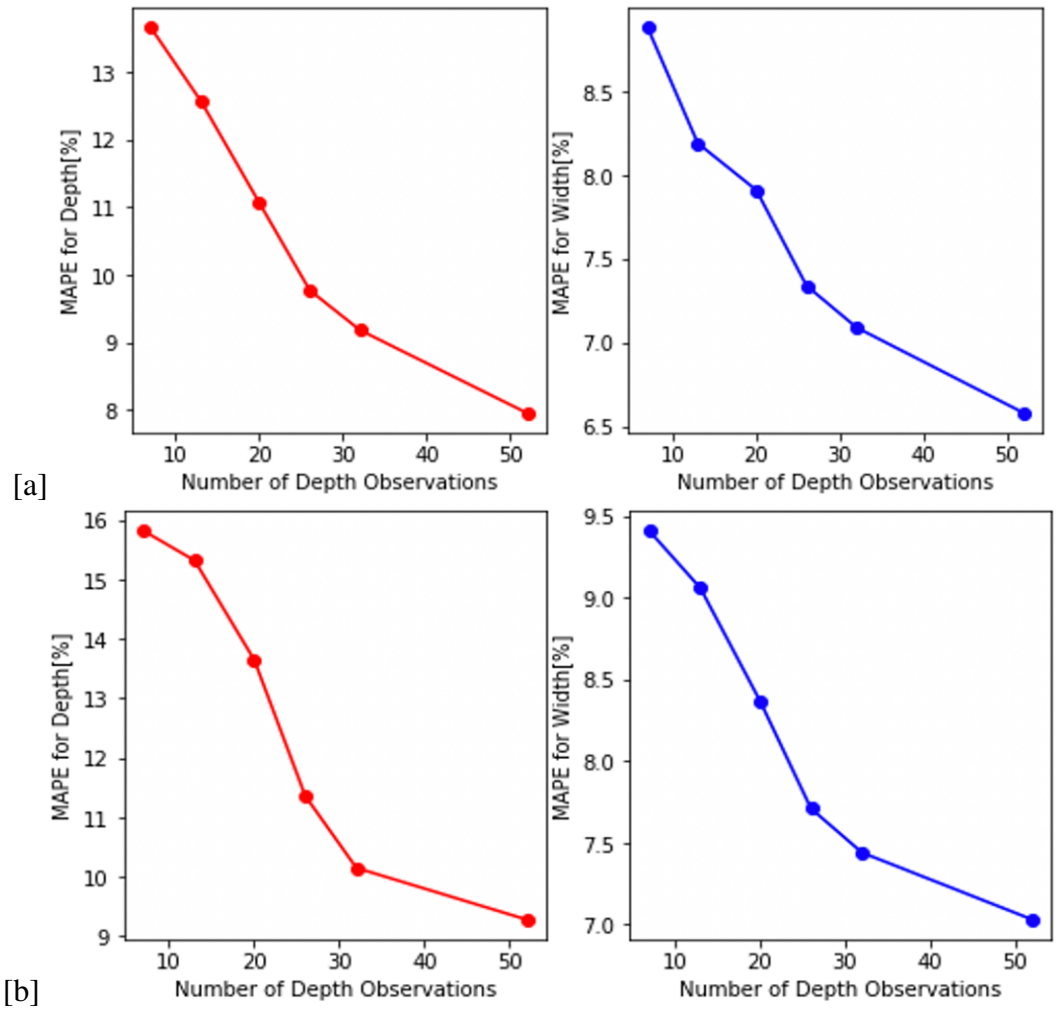


Figure 4.15: The comparison of 6 cases in the MAPE of (a) CV, and (b) testing results.

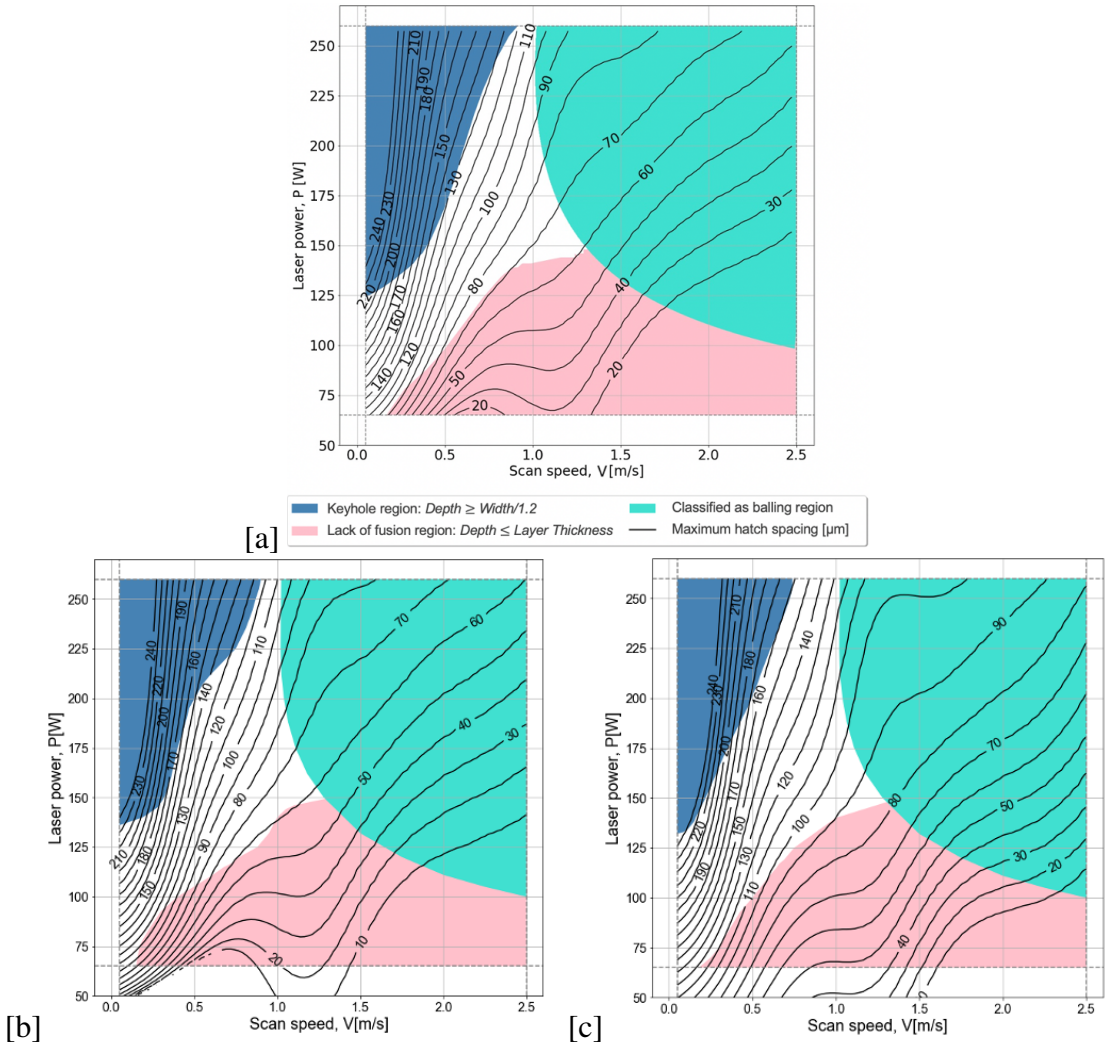


Figure 4.16: The cosssmparison of calibrated printability maps by (a) MVCalib method with 52 full melt pool data, (b) CBMI method with 52 melt pool width data and 26 melt pool depth data, and (c) CBMI method with 52 melt pool width data and 13 melt pool depth data.

# 5. SUMMARY

## 5.1 Contributions of The Dissertation

In this chapter, I will summarize the contributions of each part of the dissertation.

### 5.1.1 Contributions of Process Optimization

In chapter 2, we investigated the effects of LPBF processing parameters on as-fabricated and electropolished surface roughness of interior channels in NiTi. This work specifically characterized the overhanging surfaces of horizontal channels and the walls of vertical channels. In this work, we find that the processing parameters with lower laser energy density would result in less partial particle fusion and/or stalactite formation in as-fabricated interior channels; further, subsequent electropolishing would result in a higher reduction of surface roughness with the lower laser energy density parameter sets. In practice, lower energy density parameter sets (that still provide appropriate melting) can provide a more facile route to reduce channel surface roughness via a post-fabrication electropolishing.

The contribution of this current work is two-fold. First, it represents the first systematic effort to understand the relationships between these parameters and the surface roughness of as-fabricated NiTi parts, with an application emphasis on interior channels. Second, it presents one of the first effort on post-processing LPBF NiTi parts using electropolishing to improve surface quality and further establishes a relationship between processing parameters and electropolished surface roughness.

### 5.1.2 Contributions of Printability Framework

A unified framework was developed to enable printing defect-free parts for new AM materials and alloys in chapter 3. The proposed framework integrates an analytical thermal model, experimental characterization of single tracks, and UQ to determine windows of processing parameters that correspond to different regimes (keyholing, lack of fusion, and balling). Parameter combinations that result in parts with low porosity and low variability in mechanical properties can then

be identified. The framework was experimentally validated using three material systems. Results indicate that parts fabricated using the generated printability maps were nearly fully-dense and exhibited good repeatability of mechanical properties.

The contribution of the proposed framework can be summarized as follows: first, through effectively integrating physics-based modeling, experimental characterization, and UQ, we can construct printability maps in a systematic and accelerated fashion. This is in contrast to previous trial-and-error approaches or other systematic approaches that require large amounts of expensive and time-consuming experiments or model runs. Second, for the modeling step we make use of a well-established analytical model that is readily accessible to any user, eliminating the need for proprietary computational codes for the thermal model utilized. Furthermore, this analytical model is computationally tractable which enhances the accelerated aspect of the proposed framework. It is important to point out that enabling the use of this simple analytical, and relatively low fidelity, model is only made possible through an UQ step. In addition to constructing a printability map for a given new material, the proposed framework guides the microstructural and mechanical characterization of specimens that are printed according to that map. Porosity free parts are successfully printed with great mechanical properties in low variability.

### 5.1.3 Contributions of Uncertainty Quantification

In chapter 4, we developed methodologies in solving a special case of multivariate calibration problem in the absence of experimental data. For example, the analytical thermal model of melt pool. The outputs of this model that were considered by our framework are melt pool width and depth. However, the measurement of melt pool depth is time-consuming and costly. So that we only characterize some of the sample cross-sections to measure melt pool depth. In statistics, this is a missing value problem. In UQ, especially in the area of Bayesian multivariate calibration, there is no previous art of solving this problem. At first, we developed the hierarchical Gaussian process method to predict the missing data in our QoIs. This is a non-parametric approach with a hierarchical covariance structure among model inputs, fully observed outputs, and partially observed outputs. The correlation between outputs is the key fact enables more accurate prediction

than other approaches. Then the predicted data is combined with experimental observations to conduction model calibration as ground truth.

Another method which is different than making predictions, is to directly estimate the unknown parameters (called as calibration parameters in UQ problem) by the Bayesian multiple imputation methodology. In the multivariate Bayesian calibration framework, we took out the Bayesian calibration model which is the equation of surrogate model, model discrepancy, and error term that will be calibrate by experimental data through tuning the value of calibration parameters. Then the Bayesian multiple imputation methodology is applied to deal with missing data by expectation–maximization algorithm. Through creating a tie between the complicated partially-observed data likelihood and the simpler complete-data likelihood, we could calculate the posterior mean and variance of calibration parameters. In turn, the mean of these values are put back to a multivariate Gaussian process model to predict our QoIs given a new sets of inputs.

Both methods have been validated by a melt pool model in AM. The calibration results of melt pool width and depth ware about 10% of MAPE, which is greatly improved comparing with the MVCalib method using only the observed data. The Bayesian multiple imputation calibration method performs even better than the hierarchical Gaussian process method by avoiding an extra error term from the predictive model. Besides, we saved about $4000 (cost for preparing the sample, machine, material, etc) and one week of labor time for conducting the "unobserved" melt pool characterization.

## 5.2 Future Work

In the area of building AM specific standards and pathways, I have some future research directions that originated from the NiTi optimization project. In addition to surface roughness, the shape memory effect is mainly relevant to transformation temperatures between martensite and austenite phase. However, the control of transformation temperatures is difficult mainly due to evaporation of Ni and is thus strongly controlled by the processing parameters. A model that simulates the relationship between transformation temperatures and processing parameters is beneficial so that the temperatures are predictable and controllable. Due to its phase transformation

properties, NiTi is difficult to print complex structures. Therefore, the accuracy and variability of as-fabricated parts need to be compared and analysed. In-situ monitoring or optical profilometers (e.g., KEYENCE VR5000) are capable to capture and analyse the difference of as-fabricated parts and 3D models. On the other hand, such as electropolishing, AM requires issue guidelines for consistent post-processing techniques in various materials and AM processes.

In the proposed printability framework, a track level analytical model is used to help accelerate the printing process. Furthermore, a layer level model is expected to simulate the effect of hatch spacing parameter on thermal history. Such that heat conduction and heat accumulation can be directly studied. Fabricating fully-dense parts is only an initial step towards further objectives that necessitate future work. For example, an immediate next step involves correlating the processing parameter combinations in the printability map with microstructural features (e.g., grain size or segregation), evolution of secondary phases, and evaporative control of alloy composition. In addition, other defects like residual stress should be involved in the printability map to further improve the quality of as-printed metal parts. Developing standards identifying the means to establish the statically validated minimum mechanical properties for metals made using a given set of parameters for a given design is another essential work in developing the qualification and certification of AM.

Another area for future research is conducting statistical calibration for LPBF model when the output has a specific condition. For example, one or more of the outputs are completely unobservable (e.g. there is no experimental measurement of melt pool length). Or calibration of simulation models with high-dimensional output. Another example can be models with binary or categorical outputs, e.g. when a model predicts the types of defect for a set of processing parameters if it would be porosity, balling, or residue stress.

# REFERENCES


[1] T. Wohlers and T. Gornet, "History of additive manufacturing," *Wohlers report*, vol. 24, no. 2014, p. 118, 2014.

[2] I. Campbell, O. Diegel, J. Kowen, and T. Wohlers, *Wohlers report 2018: 3D printing and additive manufacturing state of the industry: annual worldwide progress report*. Wohlers Associates, 2018.

[3] N. Guo and M. C. Leu, "Additive manufacturing: technology, applications and research needs," *Frontiers of Mechanical Engineering*, vol. 8, no. 3, pp. 215–243, 2013.

[4] R. Liu, Z. Wang, T. Sparks, F. Liou, and J. Newkirk, "Aerospace applications of laser additive manufacturing," in *Laser additive manufacturing*, pp. 351–371, Elsevier, 2017.

[5] M. Schneck, M. Gollnau, M. Lutter-Günther, B. Haller, G. Schlick, M. Lakomiec, and G. Reinhart, "Evaluating the use of additive manufacturing in industry applications," *Procedia CIRP*, vol. 81, pp. 19–23, 2019.

[6] V. Bhavar, P. Kattire, V. Patil, S. Khot, K. Gujar, and R. Singh, "A review on powder bed fusion technology of metal additive manufacturing," *Additive manufacturing handbook*, pp. 251–253, 2017.

[7] I. Gibson, D. W. Rosen, B. Stucker, *et al.*, *Additive manufacturing technologies*, vol. 17. Springer, 2014.

[8] J. P. Oliveira, A. LaLonde, and J. Ma, "Processing parameters in laser powder bed fusion metal additive manufacturing," *Materials & Design*, vol. 193, p. 108762, 2020.

[9] P. A. Hooper, "Melt pool temperature and cooling rates in laser powder bed fusion," *Additive Manufacturing*, vol. 22, pp. 548–559, 2018.

[10] M. Agarwala, D. Bourell, J. Beaman, H. Marcus, and J. Barlow, "Direct selective laser sintering of metals," *Rapid Prototyping Journal*, 1995.

[11] M. Van Elsen, "Complexity of selective laser melting: a new optimisation approach," 2007.

[12] P. Edwards, A. O'conner, and M. Ramulu, "Electron beam additive manufacturing of titanium components: properties and performance," *Journal of Manufacturing Science and Engineering*, vol. 135, no. 6, 2013.

[13] J. D. Madison and L. K. Aagesen, "Quantitative characterization of porosity in laser welds of stainless steel," *Scripta Materialia*, vol. 67, no. 9, pp. 783–786, 2012.

[14] T. DebRoy, H. Wei, J. Zuback, T. Mukherjee, J. Elmer, J. Milewski, A. M. Beese, A. Wilson-Heid, A. De, and W. Zhang, "Additive manufacturing of metallic components–process, structure and properties," *Progress in Materials Science*, vol. 92, pp. 112–224, 2018.

[15] P. Mercelis and J.-P. Kruth, "Residual stresses in selective laser sintering and selective laser melting," *Rapid prototyping journal*, 2006.

[16] N. J. Harrison, I. Todd, and K. Mumtaz, "Reduction of micro-cracking in nickel superalloys processed by selective laser melting: A fundamental alloy design approach," *Acta Materialia*, vol. 94, pp. 59–68, 2015.

[17] M. F. Zäh and S. Lutzmann, "Modelling and simulation of electron beam melting," *Production Engineering*, vol. 4, no. 1, pp. 15–23, 2010.

[18] H. KYOGOKU and T.-T. IKESHOJI, "A review of metal additive manufacturing technologies: Mechanism of defects formation and simulation of melting and solidification phenomena in laser powder bed fusion process," *Mechanical Engineering Reviews*, vol. 7, no. 1, pp. 19–00182, 2020.

[19] D. Pal, N. Patil, K. Zeng, and B. Stucker, "An integrated approach to additive manufacturing simulations using physics based, coupled multiscale process modeling," *Journal of Manufacturing Science and Engineering*, vol. 136, no. 6, 2014.

[20] E. Yasa, J. Deckers, T. Craeghs, M. Badrossamay, and J.-P. Kruth, "Investigation on occurrence of elevated edges in selective laser melting," in *International Solid Freeform Fabrication Symposium, Austin, TX, USA*, pp. 673–85, 2009.

[21] A. Triantaphyllou, C. L. Giusca, G. D. Macaulay, F. Roerig, M. Hoebel, R. K. Leach, B. Tomita, and K. A. Milne, "Surface texture measurement for additive manufacturing," *Surface topography: metrology and properties*, vol. 3, no. 2, p. 024002, 2015.

[22] H. A. Hegab, "Design for additive manufacturing of composite materials and potential alloys: a review," *Manufacturing Review*, vol. 3, p. 11, 2016.

[23] D. L. Bourell, M. C. Leu, and D. W. Rosen, "Roadmap for additive manufacturing: identifying the future of freeform processing," *The University of Texas at Austin, Austin, TX*, pp. 11–15, 2009.

[24] K. Kempen, L. Thijs, E. Yasa, M. Badrossamay, W. Verheecke, and J. Kruth, "Process optimization and microstructural analysis for selective laser melting of alsi10mg," in *Solid Freeform Fabrication Symposium*, vol. 22, pp. 484–495, 2011.

[25] W. M. Tucho, V. H. Lysne, H. Austbø, A. Sjolyst-Kverneland, and V. Hansen, "Investigation of effects of process parameters on microstructure and hardness of slm manufactured ss316l," *Journal of Alloys and Compounds*, vol. 740, pp. 910–925, 2018.

[26] M. Averyanova, E. Cicala, P. Bertrand, and D. Grevey, "Experimental design approach to optimize selective laser melting of martensitic 17-4 ph powder: part i–single laser tracks and first layer," *Rapid Prototyping Journal*, 2012.

[27] J. Mingear, B. Zhang, D. Hartl, and A. Elwany, "Effect of process parameters and electropolishing on the surface roughness of interior channels in additively manufactured nickel-titanium shape memory alloy actuators," *Additive Manufacturing*, vol. 27, pp. 565–575, 2019.

[28] F. Bosio, A. Aversa, M. Lorusso, S. Marola, D. Gianoglio, L. Battezzati, P. Fino, D. Manfredi, and M. Lombardi, "A time-saving and cost-effective method to process alloys by laser powder bed fusion," *Materials & Design*, vol. 181, p. 107949, 2019.

[29] A. M. Aboutaleb, L. Bian, A. Elwany, N. Shamsaei, S. M. Thompson, and G. Tapia, "Accelerated process optimization for laser-based additive manufacturing by leveraging similar prior studies," *IISE Transactions*, vol. 49, no. 1, pp. 31–44, 2017.

[30] M. Yakout, A. Cadamuro, M. Elbestawi, and S. C. Veldhuis, "The selection of process parameters in additive manufacturing for aerospace alloys," *The International Journal of Advanced Manufacturing Technology*, vol. 92, no. 5-8, pp. 2081–2098, 2017.

[31] X. Wang, X. Gong, and K. Chou, "Review on powder-bed laser additive manufacturing of inconel 718 parts," *Proceedings of the Institution of Mechanical Engineers, Part B: Journal of Engineering Manufacture*, vol. 231, no. 11, pp. 1890–1903, 2017.

[32] J. Gonzalez, J. Mireles, S. Stafford, M. Perez, C. Terrazas, and R. Wicker, "Characterization of inconel 625 fabricated using powder-bed-based additive manufacturing technologies," *Journal of Materials Processing Technology*, vol. 264, pp. 200–210, 2019.

[33] L. Johnson, M. Mahmoudi, B. Zhang, R. Seede, X. Huang, J. T. Maier, H. J. Maier, I. Karaman, A. Elwany, and R. Arróyave, "Assessing printability maps in additive manufacturing of metal alloys," *Acta Materialia*, vol. 176, pp. 199–210, 2019.

[34] M. Letenneur, A. Kreitcberg, and V. Brailovski, "Optimization of laser powder bed fusion processing using a combination of melt pool modeling and design of experiment approaches: Density control," *Journal of Manufacturing and Materials Processing*, vol. 3, no. 1, p. 21, 2019.

[35] K. Dietrich, J. Diller, S. Dubiez-Le Goff, D. Bauer, P. Forêt, and G. Witt, "The influence of oxygen on the chemical composition and mechanical properties of ti-6al-4v during laser powder bed fusion (l-pbf)," *Additive Manufacturing*, vol. 32, p. 100980, 2020.

[36] A. T. Sutton, C. S. Kriewall, S. Karnati, M. C. Leu, and J. W. Newkirk, "Characterization of aisi 304l stainless steel powder recycled in the laser powder-bed fusion process," *Additive Manufacturing*, vol. 32, p. 100981, 2020.

[37] M. Skalon, B. Meier, T. Leitner, S. Arneitz, S. T. Amancio-Filho, and C. Sommitsch, "Reuse of ti6al4v powder and its impact on surface tension, melt pool behavior and mechanical properties of additively manufactured components," *Materials*, vol. 14, no. 5, p. 1251, 2021.

[38] C. Zhao, K. Fezzaa, R. W. Cunningham, H. Wen, F. De Carlo, L. Chen, A. D. Rollett, and T. Sun, "Real-time monitoring of laser powder bed fusion process using high-speed x-ray imaging and diffraction," *Scientific reports*, vol. 7, no. 1, pp. 1–11, 2017.

[39] M. Mani, B. M. Lane, M. A. Donmez, S. C. Feng, and S. P. Moylan, "A review on measurement science needs for real-time control of additive manufacturing metal powder bed fusion processes," *International Journal of Production Research*, vol. 55, no. 5, pp. 1400–1418, 2017.

[40] R. Acharya, J. A. Sharon, and A. Staroselsky, "Prediction of microstructure in laser powder bed fusion process," *Acta Materialia*, vol. 124, pp. 360–371, 2017.

[41] A. J. Dunbar, "Analysis of the laser powder bed fusion additive manufacturing process through experimental measurement and finite element modeling," 2016.

[42] A. J. Dunbar, E. R. Denlinger, M. F. Gouge, and P. Michaleris, "Experimental validation of finite element modeling for laser powder bed fusion deformation," *Additive Manufacturing*, vol. 12, pp. 108–120, 2016.

[43] F. Lopez, P. Witherell, and B. Lane, "Identifying uncertainty in laser powder bed fusion additive manufacturing models," *Journal of Mechanical Design*, vol. 138, no. 11, 2016.

[44] A. Chernatynskiy, S. R. Phillpot, and R. LeSar, "Uncertainty quantification in multiscale simulation of materials: A prospective," *Annual Review of Materials Research*, vol. 43, pp. 157–182, 2013.

[45] A. O'Hagan, "Bayesian analysis of computer code outputs: A tutorial," *Reliability Engineering & System Safety*, vol. 91, no. 10-11, pp. 1290–1300, 2006.

[46] T. Moges, G. Ameta, and P. Witherell, "A review of model inaccuracy and parameter uncertainty in laser powder bed fusion models and simulations," *Journal of manufacturing science and engineering*, vol. 141, no. 4, 2019.

[47] Z. Hu, S. Mahadevan, and X. Du, "Uncertainty quantification of time-dependent reliability analysis in the presence of parametric uncertainty," *ASCE-ASME Journal of risk and uncertainty in Engineering systems, Part B: Mechanical Engineering*, vol. 2, no. 3, 2016.

[48] D. Xiu and G. E. Karniadakis, "The wiener–askey polynomial chaos for stochastic differential equations," *SIAM journal on scientific computing*, vol. 24, no. 2, pp. 619–644, 2002.

[49] C. Kamath, "Data mining and statistical inference in selective laser melting," *The International Journal of Advanced Manufacturing Technology*, vol. 86, no. 5-8, pp. 1659–1677, 2016.

[50] J. A. Turner, S. S. Babu, and C. Blue, "Advanced simulation for additive manufacturing: meeting challenges through collaboration," *ORNL/TM-2015/324*, 2015.

[51] M. C. Kennedy and A. O'Hagan, "Bayesian calibration of computer models," *Journal of the Royal Statistical Society: Series B (Statistical Methodology)*, vol. 63, no. 3, pp. 425–464, 2001.

[52] G. Tapia, W. King, L. Johnson, R. Arroyave, I. Karaman, and A. Elwany, "Uncertainty propagation analysis of computational models in laser powder bed fusion additive manufacturing using polynomial chaos expansions," *Journal of Manufacturing Science and Engineering*, vol. 140, no. 12, 2018.

[53] M. Mahmoudi, G. Tapia, K. Karayagiz, B. Franco, J. Ma, R. Arroyave, I. Karaman, and A. Elwany, "Multivariate calibration and experimental validation of a 3d finite element thermal model for laser powder bed fusion metal additive manufacturing," *Integrating Materials and Manufacturing Innovation*, vol. 7, no. 3, pp. 116–135, 2018.

[54] J. M. Walker, C. Haberland, M. Taheri Andani, H. E. Karaca, D. Dean, and M. Elahinia, "Process development and characterization of additively manufactured nickel–titanium

shape memory parts," *Journal of Intelligent Material Systems and Structures*, vol. 27, no. 19, pp. 2653–2660, 2016.

[55] M. Pohl, C. Hessing, and J. Frenzel, "Electrolytic processing of NiTi shape memory alloys," *Materials Science and Engineering: A*, vol. 378, no. 1, pp. 191–199, 2004.

[56] A. P. Charles, A. Elkaseer, T. Muller, L. Thijs, M. Torge, V. Hagenmeyer, and S. Scholz, "A study of the factors influencing generated surface roughness of down-facing surfaces in selective laser melting," in *World Congress on Micro and Nano Manufacturing*, Sep 2018.

[57] J. P. Davim and others, *Surface integrity in machining*, vol. 1848828742. Springer, 2010.

[58] G. Strano, L. Hao, R. M. Everson, and K. E. Evans, "Surface roughness analysis, modelling and prediction in selective laser melting," *Journal of Materials Processing Technology*, vol. 213, no. 4, pp. 589–597, 2013.

[59] M. Cotteleer and J. Joyce, "3d opportunity: Additive manufacturing paths to performance, innovation, and growth," *Deloitte Review*, vol. 14, pp. 5–19, 2014.

[60] T. D. Ngo, A. Kashani, G. Imbalzano, K. T. Nguyen, and D. Hui, "Additive manufacturing (3d printing): A review of materials, methods, applications and challenges," *Composites Part B: Engineering*, vol. 143, pp. 172–196, 2018.

[61] H. Fayazfar, M. Salarian, A. Rogalsky, D. Sarker, P. Russo, V. Paserin, and E. Toyserkani, "A critical review of powder-based additive manufacturing of ferrous alloys: Process parameters, microstructure and mechanical properties," *Materials & Design*, vol. 144, pp. 98–128, 2018.

[62] Y. M. Arısoy, L. E. Criales, T. Özel, B. Lane, S. Moylan, and A. Donmez, "Influence of scan strategy and process parameters on microstructure and its optimization in additively manufactured nickel alloy 625 via laser powder bed fusion," *The International Journal of Advanced Manufacturing Technology*, vol. 90, no. 5-8, pp. 1393–1417, 2017.

[63] B. Song, S. Dong, B. Zhang, H. Liao, and C. Coddet, "Effects of processing parameters on microstructure and mechanical property of selective laser melted ti6al4v," *Materials & Design*, vol. 35, pp. 120–125, 2012.

[64] W. E. King, A. T. Anderson, R. M. Ferencz, N. E. Hodge, C. Kamath, S. A. Khairallah, and A. M. Rubenchik, "Laser powder bed fusion additive manufacturing of metals; physics, computational, and materials challenges," *Applied Physics Reviews*, vol. 2, no. 4, p. 041304, 2015.

[65] N. Read, W. Wang, K. Essa, and M. M. Attallah, "Selective laser melting of alsi10mg alloy: Process optimisation and mechanical properties development," *Materials & Design (1980-2015)*, vol. 65, pp. 417–424, 2015.

[66] H. Gong, H. Gu, K. Zeng, J. Dilip, D. Pal, B. Stucker, D. Christiansen, J. Beuth, and J. J. Lewandowski, "Melt pool characterization for selective laser melting of ti-6al-4v pre-alloyed powder," in *Solid freeform fabrication symposium*, pp. 256–267, 2014.

[67] A. M. Khorasani, I. Gibson, M. Goldberg, and G. Littlefair, "A survey on mechanisms and critical parameters on solidification of selective laser melting during fabrication of ti-6al-4v prosthetic acetabular cup," *Materials & Design*, vol. 103, pp. 348–355, 2016.

[68] W. E. King, H. D. Barth, V. M. Castillo, G. F. Gallegos, J. W. Gibbs, D. E. Hahn, C. Kamath, and A. M. Rubenchik, "Observation of keyhole-mode laser melting in laser powder-bed fusion additive manufacturing," *Journal of Materials Processing Technology*, vol. 214, no. 12, pp. 2915–2925, 2014.

[69] R. Cunningham, S. P. Narra, C. Montgomery, J. Beuth, and A. Rollett, "Synchrotron-based x-ray microtomography characterization of the effect of processing variables on porosity formation in laser power-bed additive manufacturing of ti-6al-4v," *Jom*, vol. 69, no. 3, pp. 479–484, 2017.

[70] C. Kamath, B. El-Dasher, G. F. Gallegos, W. E. King, and A. Sisto, "Density of additively-manufactured, 316l ss parts using laser powder-bed fusion at powers up to 400 w," *The*

*International Journal of Advanced Manufacturing Technology*, vol. 74, no. 1, pp. 65–78, 2014.

[71] M. Tang, P. C. Pistorius, and J. L. Beuth, "Prediction of lack-of-fusion porosity for powder bed fusion," *Additive Manufacturing*, vol. 14, pp. 39–48, 2017.

[72] T. Mukherjee, J. Zuback, A. De, and T. DebRoy, "Printability of alloys for additive manufacturing," *Scientific reports*, vol. 6, no. 1, pp. 1–8, 2016.

[73] X. Zhou, X. Liu, D. Zhang, Z. Shen, and W. Liu, "Balling phenomena in selective laser melted tungsten," *Journal of Materials Processing Technology*, vol. 222, pp. 33–42, 2015.

[74] R. Li, J. Liu, Y. Shi, L. Wang, and W. Jiang, "Balling behavior of stainless steel and nickel powder during selective laser melting process," *The International Journal of Advanced Manufacturing Technology*, vol. 59, no. 9, pp. 1025–1035, 2012.

[75] D. Gu and Y. Shen, "Balling phenomena during direct laser sintering of multi-component cu-based metal powder," *Journal of Alloys and Compounds*, vol. 432, no. 1-2, pp. 163–166, 2007.

[76] J. J. Lewandowski and M. Seifi, "Metal additive manufacturing: a review of mechanical properties," *Annual review of materials research*, vol. 46, pp. 151–186, 2016.

[77] K. Karayagiz, L. Johnson, R. Seede, V. Attari, B. Zhang, X. Huang, S. Ghosh, T. Duong, I. Karaman, A. Elwany, *et al.*, "Finite interface dissipation phase field modeling of ni–nb under additive manufacturing conditions," *Acta Materialia*, vol. 185, pp. 320–339, 2020.

[78] M. Chase Jr, "Nist-janaf thermochemical tables fourth edition," *J. Phys. Chem. Ref. Data, Monograph*, vol. 9, 1998.

[79] J. J. Valencia and P. N. Quested, "Thermophysical properties," 2013.

[80] Y. Zhang, J. R. Evans, and S. Yang, "Corrected values for boiling points and enthalpies of vaporization of elements in handbooks," *Journal of Chemical & Engineering Data*, vol. 56, no. 2, pp. 328–337, 2011.

[81] C. Boley, S. Mitchell, A. Rubenchik, and S. Wu, "Metal powder absorptivity: modeling and experiment," *Applied optics*, vol. 55, no. 23, pp. 6496–6500, 2016.

[82] T. Eagar, N. Tsai, *et al.*, "Temperature fields produced by traveling distributed heat sources," *Welding journal*, vol. 62, no. 12, pp. 346–355, 1983.

[83] G. Kasperovich, J. Haubrich, J. Gussone, and G. Requena, "Correlation between porosity and processing parameters in tial6v4 produced by selective laser melting," *Materials & Design*, vol. 105, pp. 160–170, 2016.

[84] N. H. Paulson, B. Gould, S. J. Wolff, M. Stan, and A. C. Greco, "Correlations between thermal history and keyhole porosity in laser powder bed fusion," *Additive Manufacturing*, vol. 34, p. 101213, 2020.

[85] M. Brandt, *Laser additive manufacturing: materials, design, technologies, and applications*. Woodhead Publishing, 2016.

[86] I. Yadroitsev, P. Krakhmalev, I. Yadroitsava, S. Johansson, and I. Smurov, "Energy input effect on morphology and microstructure of selective laser melting single track from metallic powder," *Journal of Materials Processing Technology*, vol. 213, no. 4, pp. 606–613, 2013.

[87] K. Campbell, "Statistical calibration of computer simulations," *Reliability Engineering & System Safety*, vol. 91, no. 10-11, pp. 1358–1363, 2006.

[88] C. Y. Yap, H. K. Tan, Z. Du, C. K. Chua, and Z. Dong, "Selective laser melting of nickel powder," *Rapid Prototyping Journal*, 2017.

[89] J. Q. Shi and T. Choi, *Gaussian process regression analysis for functional data*. CRC Press, 2011.

[90] C. K. Williams, "Prediction with gaussian processes: From linear regression to linear prediction and beyond," in *Learning in graphical models*, pp. 599–621, Springer, 1998.

[91] Z.-H. Han and S. Görtz, "Hierarchical kriging model for variable-fidelity surrogate modeling," *AIAA journal*, vol. 50, no. 9, pp. 1885–1896, 2012.

[92] P. Li and S. Chen, "A review on gaussian process latent variable models," *CAAI Transactions on Intelligence Technology*, vol. 1, no. 4, pp. 366–376, 2016.

[93] M. Titsias and N. D. Lawrence, "Bayesian gaussian process latent variable model," in *Proceedings of the Thirteenth International Conference on Artificial Intelligence and Statistics*, pp. 844–851, JMLR Workshop and Conference Proceedings, 2010.

[94] N. D. Lawrence and A. J. Moore, "Hierarchical gaussian process latent variable models," in *Proceedings of the 24th international conference on Machine learning*, pp. 481–488, 2007.

[95] A. E. Raftery and S. M. Lewis, "Implementing mcmc," *Markov chain Monte Carlo in practice*, pp. 115–130, 1996.

[96] I. Yildirim, "Bayesian inference: Gibbs sampling," *Technical Note, University of Rochester*, 2012.

[97] P. Li and S. Chen, "Hierarchical gaussian processes model for multi-task learning," *Pattern Recognition*, vol. 74, pp. 134–144, 2018.

[98] D. Berrar, "Cross-validation," *Encyclopedia of bioinformatics and computational biology*, vol. 1, pp. 542–545, 2019.

[99] S. Babicki, D. Arndt, A. Marcu, Y. Liang, J. R. Grant, A. Maciejewski, and D. S. Wishart, "Heatmapper: web-enabled heat mapping for all," *Nucleic acids research*, vol. 44, no. W1, pp. W147–W153, 2016.

[100] M. Baumers, P. Dickens, C. Tuck, and R. Hague, "The cost of additive manufacturing: machine productivity, economies of scale and technology-push," *Technological forecasting and social change*, vol. 102, pp. 193–201, 2016.

[101] H. Piili, A. Happonen, T. Väistö, V. Venkataramanan, J. Partanen, and A. Salminen, "Cost estimation of laser additive manufacturing of stainless steel," *Physics Procedia*, vol. 78, pp. 388–396, 2015.

[102] G. E. Box, "Sampling and bayes' inference in scientific modelling and robustness," *Journal of the Royal Statistical Society: Series A (General)*, vol. 143, no. 4, pp. 383–404, 1980.

[103] M. J. Daniels and J. W. Hogan, *Missing data in longitudinal studies: Strategies for Bayesian modeling and sensitivity analysis*. CRC press, 2008.

[104] C. K. Enders, "A primer on maximum likelihood algorithms available for use with missing data," *Structural Equation Modeling*, vol. 8, no. 1, pp. 128–141, 2001.

[105] C. L. O. Peters and C. Enders, "A primer for the estimation of structural equation models in the presence of missing data: Maximum likelihood algorithms," *Journal of Targeting, Measurement and Analysis for Marketing*, vol. 11, no. 1, pp. 81–95, 2002.

[106] T. K. Moon, "The expectation-maximization algorithm," *IEEE Signal processing magazine*, vol. 13, no. 6, pp. 47–60, 1996.

[107] J. V. Graça, K. Ganchev, and B. Taskar, "Expectation maximization and posterior constraints," 2007.

[108] K. R. Koch, "Robust estimation by expectation maximization algorithm," *Journal of Geodesy*, vol. 87, no. 2, pp. 107–116, 2013.

[109] S. L. Lauritzen, "The em algorithm for graphical association models with missing data," *Computational Statistics & Data Analysis*, vol. 19, no. 2, pp. 191–201, 1995.

[110] R. Little *et al.*, "Calibrated bayes, for statistics in general, and missing data in particular," *Statistical Science*, vol. 26, no. 2, pp. 162–174, 2011.

[111] A. Gelman, I. Van Mechelen, G. Verbeke, D. F. Heitjan, and M. Meulders, "Multiple imputation for model checking: completed-data plots with missing and latent data," *Biometrics*, vol. 61, no. 1, pp. 74–85, 2005.

[112] A. Gelman, D. B. Rubin, *et al.*, "Inference from iterative simulation using multiple sequences," *Statistical science*, vol. 7, no. 4, pp. 457–472, 1992.

[113] D. Kaplan and S. Yavuz, "An approach to addressing multiple imputation model uncertainty using bayesian model averaging," *Multivariate behavioral research*, vol. 55, no. 4, pp. 553–567, 2020.

[114] K. J. Lee and J. B. Carlin, "Multiple imputation for missing data: fully conditional specification versus multivariate normal imputation," *American journal of epidemiology*, vol. 171, no. 5, pp. 624–632, 2010.

[115] T. E. Raghunathan, J. M. Lepkowski, J. Van Hoewyk, P. Solenberger, *et al.*, "A multivariate technique for multiply imputing missing values using a sequence of regression models," *Survey methodology*, vol. 27, no. 1, pp. 85–96, 2001.

[116] J. L. Schafer, *Analysis of incomplete multivariate data*. CRC press, 1997.

[117] I. Alvarez, J. Niemi, and M. Simpson, "Bayesian inference for a covariance matrix," *arXiv preprint arXiv:1408.4050*, 2014.

[118] Z. Hu and S. Mahadevan, "Uncertainty quantification and management in additive manufacturing: current status, needs, and opportunities," *The International Journal of Advanced Manufacturing Technology*, vol. 93, no. 5-8, pp. 2855–2874, 2017.

[119] S. Conti and A. O'Hagan, "Bayesian emulation of complex multi-output and dynamic computer models," *Journal of statistical planning and inference*, vol. 140, no. 3, pp. 640–651, 2010.

[120] S. Zhu, K. Yu, and Y. Gong, "Predictive matrix-variate t models.," in *NIPS*, vol. 7, pp. 1721–1728, 2007.

[121] M. Strand, "Metropolis-hastings markov chain monte carlo," *Chapman University. Copyright Date: May*, 2009.

[122] K. S. Bhat, M. Haran, M. Goes, and M. Chen, "Computer model calibration with multivariate spatial output: A case study," *Frontiers of statistical decision making and Bayesian analysis*, pp. 168–184, 2010.

[123] C. Andrieu, N. De Freitas, A. Doucet, and M. I. Jordan, "An introduction to mcmc for machine learning," *Machine learning*, vol. 50, no. 1, pp. 5–43, 2003.

[124] P. D. Hoff, "Simulation of the matrix bingham–von mises–fisher distribution, with applications to multivariate and relational data," *Journal of Computational and Graphical Statistics*, vol. 18, no. 2, pp. 438–456, 2009.

APPENDIX A

# THE TWO-STAGE MULTIVARIATE CALIBRATION METHOD

The multivariate calibration method is based on the famous two-stage approach developed by Conti O'Hagan [119]. First stage is to build a multivariate Gaussian process surrogate model to output. Second stage is connecting the calibration parameters to the observations using the built surrogate model while allowing for model discrepancy and measurement errors. The final goal is to have the posterior distributions for the calibration parameters. Then the mean or mode of the posterior distributions will be used as estimations of calibration parameters.

Table A.1: Notations from Conti and O'Hagan

| | | | |
|---|---|---|---|
| $\boldsymbol{x}$ | $\triangleq$ | Input vector | $p \times 1$ |
| $\boldsymbol{y}$ | $\triangleq$ | Simulation output | $q \times 1$ |
| $B$ | $\triangleq$ | Matrix of regression coefficients | $m \times q$ |
| $\hat{B}_{GLS}$ | $\triangleq$ | Generalized lease squares (GLS) estimator of $B$ | $m \times q$ |
| $\Sigma$ | $\triangleq$ | Covariance matrix | $q \times q$ |
| $\hat{\Sigma}_{GLS}$ | $\triangleq$ | GLS estimator of the covariance matrix | $q \times q$ |
| $\boldsymbol{r}$ | $\triangleq$ | Vector of positive roughness parameters | $p \times 1$ |
| $\boldsymbol{m}(\cdot)$ | $\triangleq$ | Mean function | $q \times 1$ |
| $c(\cdot,\cdot)$ | $\triangleq$ | Correlation function | $1 \times 1$ |
| $\boldsymbol{h}(\boldsymbol{x})$ | $\triangleq$ | Arbitrary vector of $m$ regression functions | $m \times 1$ |
| $D$ | $\triangleq$ | Output matrix | $n \times q$ |
| $R$ | $\triangleq$ | Diagonal matrix of $p$ positive roughness parameters | $p \times p$ |
| $H$ | $\triangleq$ | Design matrix | $n \times m$ |
| $A$ | $\triangleq$ | Correlation matrix | $n \times n$ |

## A.1 Surrogate Model

This stage aims to find the multivariate Gaussian predictive distribution for the computer model output $\boldsymbol{f}(\cdot)$. There are two steps in building the emulator. First, roughness parameters $r_i$ need to be found by generating the posterior distribution of $\boldsymbol{r}$ given the data, $\pi_{\boldsymbol{R}}(\boldsymbol{r}|D)$. That is explained

in Section A.1.1. Then, they are used to generate samples from a matrix-variate $\mathcal{T}$ distribution to numerically generate $\boldsymbol{f}(\cdot)$.

#### *A.1.0.1 Matrix-variate $\mathcal{T}$ distribution*

Assume the simulation training set is $\mathcal{S} = \{\boldsymbol{s}_1 ... \boldsymbol{s}_n\}$. We denote the output matrix $D = [f_j(\boldsymbol{s}_r)] \in \mathbb{R}^{n,q}$. Conditional posterior distribution of $\boldsymbol{f}(\cdot)$ given $\boldsymbol{r}$ is a $q$-variate $\mathcal{T}$ process [120]. This means the distribution of an arbitrary collection of vectors is matrix-variate $\mathcal{T}$.

$$\boldsymbol{f}(\cdot)|\boldsymbol{r}, D \sim MVT(\boldsymbol{m^{**}}(\cdot), c^{**}(\cdot,\cdot)\hat{\Sigma}_{GLS}); n-m) \tag{A.1}$$

Where:

$$\boldsymbol{m^{**}}(\boldsymbol{x_1}) = \hat{B}^T_{GLS}\boldsymbol{h}(\boldsymbol{x_1}) + (D - H\hat{B}_{GLS})^T A^{-1}\boldsymbol{t}(\boldsymbol{x_1}) \tag{A.2}$$

$$c^{**}(\boldsymbol{x_1}, \boldsymbol{x_2}) = c(\boldsymbol{x_1}, \boldsymbol{x_2}) - \boldsymbol{t}^T(\boldsymbol{x_1})A^{-1}\boldsymbol{t}(\boldsymbol{x_2}) + \tag{A.3}$$

$$[\boldsymbol{h}(\boldsymbol{x_1}) - H^T A^{-1}\boldsymbol{t}(\boldsymbol{x_1})]^T \cdot (H^T A^{-1} H)^{-1} \cdot [\boldsymbol{h}(\boldsymbol{x_2}) - H^T A^{-1}\boldsymbol{t}(\boldsymbol{x_2})] \tag{A.4}$$

$$\hat{\Sigma}_{GLS} = (n-m)^{-1}(D - H\hat{B}^T_{GLS})^T A^{-1}(D - H\hat{B}^T_{GLS}) \tag{A.5}$$

where:

$$\boldsymbol{h}^T(\boldsymbol{x}) = (1, \boldsymbol{x}^T) \tag{A.6}$$

$$H^T = [\boldsymbol{h}(\boldsymbol{s}_1), ..., \boldsymbol{h}(\boldsymbol{s}_n)] \in \mathbb{R}^{m,n} \tag{A.7}$$

$$c(\boldsymbol{x}_1, \boldsymbol{x}_2) = \exp\left\{-(\boldsymbol{x}_1 - \boldsymbol{x}_2)^T R(\boldsymbol{x}_1 - \boldsymbol{x}_2)\right\} \tag{A.8}$$

$$A = [c(\boldsymbol{s}_r, \boldsymbol{s}_l)] \in \mathbb{R}^{n,n} \tag{A.9}$$

$$\hat{B}_{GLS} = (H^T A^{-1} H)^{-1} H^T A^{-1} D \tag{A.10}$$

$$\boldsymbol{t}^T(\cdot) = [c(\cdot, \boldsymbol{s}_1), ..., c(\cdot, \boldsymbol{s}_n)] \in \mathbb{R}^n \tag{A.11}$$

### A.1.1 Monte Carlo-based marginalization

First, the priors for the smoothness parameters vector $\boldsymbol{r}$ are decided. One suggestion can be normalized scale product of i.i.d. vague (albeit proper) Log-Logistic priors $\pi_{\boldsymbol{R}}(\boldsymbol{r}) = \prod_{i=1}^{p}(1 + r_i^2)^{-1}$. Next, the posterior distribution of $\boldsymbol{r}$ would be:

$$\pi_{\boldsymbol{R}}(\boldsymbol{r}|D) \propto \pi_{\boldsymbol{R}}(\boldsymbol{r})|A|^{-q/2}|H^T A^{-1} H|^{-q/2}|D^T G D|^{-(n-m)/2} \tag{A.12}$$

where,

$$G = A^{-1} - A^{-1} H (H^T A^{-1} H)^{-1} H^T A^{-1} \tag{A.13}$$

At this point Conti and O'Hagan suggest taking a fully Bayesian approach by sampling from Eq. A.12, for example by Metropolis-Hastings Markov Chain Monte Carlo (MCMC), in order to average the conditional posterior Eq. A.1 with respect to $\boldsymbol{r}$ [121]. In practice, it is simpler and adequate just to plug estimates of the $r_i$'s into Eq. A.1. These estimates may be obtained by maximizing Eq. A.12 with respect to the $r_i$'s, or by taking mean or median values from a MCMC run. As with a single output, this is typically the most demanding part of building an emulator. Even maximizing Eq. A.12 is not straightforward; there may be several local maxima or ridges, and the computations can be numerically ill-conditioned. Then the surrogate model is validated using cross-validation method.

The following steps for decomposing the matrices are used in computing the posterior distribution of $\boldsymbol{r}$:

$$Q_1 = chol(A) \rightarrow Q_1^T Q_1 = A \tag{A.14}$$

$$W_1 = Q_1^T \backslash H = Q_1^{-T} H \tag{A.15}$$

$$\rightarrow Z_1 = W_1^T W_1 = H^T Q_1^{-1} Q_1^{-T} H = H^T (Q_1^T Q_1)^{-1} H = H^T A^{-1} H \tag{A.16}$$

Similarly:

$$Q_2 = chol(Z_1) \rightarrow Q_2^T Q_2 = Z_1 \tag{A.17}$$

$$Z_2 = (A \backslash H)^T = (A^{-1} H)^T \tag{A.18}$$

$$W_2 = Q_2^T \backslash Z_2 = Q_2^{-T} Z_2 \tag{A.19}$$

$$\rightarrow Z_3 = W_2^T W_2 = Z_2^T Q_2^{-1} Q_2^{-T} Z_2 = (A^{-1} H)(Q_2^T Q_2)^{-1} (A^{-1} H)^T \tag{A.20}$$

$$= (A^{-1} H) Z_1^{-1} (H^T A^{-1}) = (A^{-1} H)(H^T A^{-1} H)^{-1} (H^T A^{-1}) \tag{A.21}$$

$$\rightarrow G = A^{-1} - Z_3 \tag{A.22}$$

Hence, the Cholesky decomposition and matrices $Q_1$, $Q_2$, $W_1$, $W_2$, $Z_1$, $Z_2$, $Z_3$ are introduced to compute $G$. Since $Q_1$ and $Q_2$ are triangular matrices,

$$|A| = (\prod_i diag_{Q_1,i})^2 \tag{A.23}$$

$$|H^T A^{-1} H| = |Z_2| = (\prod_i diag_{Q_2,i})^2 \tag{A.24}$$

It is also necessary to compute the logarithm of the probability in Eq. A.12 than the actual

value. It follows:

$$\log \pi_{\boldsymbol{R}}(\boldsymbol{r}|D) = \log \pi_{\boldsymbol{R}}(\boldsymbol{r}) + (-q/2) \cdot 2 \sum_i \log diag_{Q_1,i} + \tag{A.25}$$

$$(-q/2) \cdot 2 \sum_i \log diag_{Q_2,i} + (\frac{m-n}{2}) \log |D^T G D| \tag{A.26}$$

## A.2 Calibration

The probability model for calibration is provided below [122]:

$$\boldsymbol{y}^E(\boldsymbol{x}) = \boldsymbol{y}^S(\boldsymbol{x}, \boldsymbol{\theta}) + \boldsymbol{\delta}(\boldsymbol{x}) + \boldsymbol{\epsilon} = \boldsymbol{f}(\boldsymbol{x}, \boldsymbol{\theta}) + \boldsymbol{\delta}(\boldsymbol{x}) + \boldsymbol{\epsilon} \tag{A.27}$$

Using the normal distribution approximation to get:

$$\boldsymbol{f}(\boldsymbol{x}, \boldsymbol{\theta}) \sim \mathcal{GP}(\boldsymbol{m}^{**}(\cdot), c^{**}(\cdot,\cdot)\hat{\Sigma}_{GLS}). \tag{A.28}$$

The values of $\boldsymbol{m}^{**}(\cdot)$, $c^{**}(\cdot,\cdot)$, and $\hat{\Sigma}_{GLS}$ were determined after the emulator was trained. As in [122], the discrepancy function $\boldsymbol{\delta}(\boldsymbol{x})$ is assumed:

$$\boldsymbol{\delta}(\boldsymbol{x}) \sim \mathcal{GP}(\boldsymbol{0}, c_\delta(\cdot,\cdot)\Sigma_\delta) \tag{A.29}$$

where:

$$c_\delta(\boldsymbol{x}_1, \boldsymbol{x}_2) = \exp\left\{-(\boldsymbol{x}_1 - \boldsymbol{x}_2)^T R_\delta (\boldsymbol{x}_1 - \boldsymbol{x}_2)\right\} \tag{A.30}$$

$$R_\delta = \begin{pmatrix} r_{\delta_1} & \cdots & 0 \\ \vdots & \ddots & \vdots \\ 0 & \cdots & r_{\delta_\kappa} \end{pmatrix} \tag{A.31}$$

$$\Sigma_\delta = \begin{pmatrix} \sigma_{11} & \cdots & \sigma_{1q} \\ \vdots & \ddots & \vdots \\ \sigma_{q1} & \cdots & \sigma_{qq} \end{pmatrix}. \tag{A.32}$$

For the roughness parameters for $c_\delta(\cdot,\cdot)$, the vector $\boldsymbol{r}_\delta = (r_{\delta_1}, \cdots, r_{\delta_\kappa})$ where $\kappa$is the number of input variables. The priors for $r_{\delta_\kappa}$ are log-logistic. $\boldsymbol{\psi}_\delta$ consists of diagonal elements and upper/lower diagonal elements of $\Sigma_\delta$, for which uses an inverse Wishart distribution. A simpler covariance structure for the error term $\boldsymbol{\epsilon}$ is:

$$\boldsymbol{\epsilon} \sim \mathcal{GP}(\mathbf{0}, \Sigma_\epsilon) \tag{A.33}$$

$$\Sigma_\epsilon = \begin{pmatrix} \psi_1 & \cdots & 0 \\ \vdots & \ddots & \vdots \\ 0 & \cdots & \psi_q \end{pmatrix}. \tag{A.34}$$

Similarly, the vector $\boldsymbol{\psi}_\epsilon = (\psi_1, \cdots, \psi_q)$ is defined. Inverse gamma priors are used for the element of $\boldsymbol{\psi}_\epsilon$. Eventually,

$$\boldsymbol{y}^E(\boldsymbol{x})|\boldsymbol{\theta}, \boldsymbol{r}_\delta, \boldsymbol{\psi}_\delta, \boldsymbol{\psi}_\epsilon \sim \mathcal{GP}(\boldsymbol{m}^{**}(\cdot), c^{**}(\cdot,\cdot)\hat{\Sigma}_{GLS} + c_\delta(\cdot,\cdot)\Sigma_\delta + \Sigma_\epsilon), \tag{A.35}$$

where $\boldsymbol{\theta}$ is the vector of calibration parameters, $\boldsymbol{r}_\delta$ is the vector of roughness parameters for covariance function $c_\delta$, and $\boldsymbol{\psi}_\delta$ and $\boldsymbol{\psi}_\epsilon$ are the vectors of covariance parameters for the discrepancy and error, respectively.

Table A.2: Summary of the calibration parameters

| | | | |
|---|---|---|---|
| $\boldsymbol{X}^S$ | $\triangleq$ | Input matrix of numerical observations | $n \times p$ |
| $\boldsymbol{D}$ | $\triangleq$ | Output matrix of numerical observations | $n \times q$ |
| $\boldsymbol{X}^E$ | $\triangleq$ | Input matrix of physical observations | $N \times \kappa$ |
| $\boldsymbol{Y}^E$ | $\triangleq$ | Output matrix of physical observations | $N \times q$ |
| $\boldsymbol{\theta}$ | $\triangleq$ | Vector of calibration parameters | $(p-\kappa) \times 1$ |
| $\boldsymbol{r}_\delta$ | $\triangleq$ | Roughness parameters for the discrepancy function | $\kappa \times 1$ |
| $\boldsymbol{\Sigma}_\delta$ | $\triangleq$ | Covariance matrix for the discrepancy function | $q \times q$ |
| $\boldsymbol{\psi}_\delta$ | $\triangleq$ | Covariance parameters for the discrepancy function | $(q \cdot \frac{q+1}{2}) \times 1$ |
| $\boldsymbol{\psi}_\epsilon$ | $\triangleq$ | Covariance parameters for the error | $q \times 1$ |

### A.2.1 Prediction

Kriging technique is used for final predictions after the parameters are calibrated. Consider about predicting the output of $S$ new inputs; hence $\boldsymbol{X}^P$ is of size $S \times \kappa$. For computing the output $\boldsymbol{Y}^P$, the experimental values in addition to running the simulation with calibrated set of parameters $\boldsymbol{\theta}^*$ are used.

$$\mathbb{E}[\boldsymbol{Y}^P|\boldsymbol{Y}^E] = \boldsymbol{m}^{**}(\boldsymbol{X}^P) + \boldsymbol{\Sigma}^{PE}(\boldsymbol{\Sigma}^{EE})^{-1}(\boldsymbol{Y}^E - \boldsymbol{m}^{**}(\boldsymbol{X}^E)), \tag{A.36}$$

where:

$$\boldsymbol{\Sigma}^{PE} = \boldsymbol{C}_{em}^{PE} \otimes \hat{\boldsymbol{\Sigma}}_{GLS} + \boldsymbol{C}_{\delta}^{PE} \otimes \boldsymbol{\Sigma}_\delta, \tag{A.37}$$

$$\boldsymbol{C}_{em}^{PE} = [c^{**}(\boldsymbol{x}_i^P, \boldsymbol{x}_j^E; \boldsymbol{\theta}^*)]_{\substack{i=1\ldots S \\ j=1\ldots N}}, \tag{A.38}$$

$$\boldsymbol{C}_{\delta}^{PE} = [c(\boldsymbol{x}_i^P, \boldsymbol{x}_j^E)]_{\substack{i=1\ldots S \\ j=1\ldots N}}, \tag{A.39}$$

$$\boldsymbol{\Sigma}^{EE} = \boldsymbol{C}_{em} \otimes \hat{\boldsymbol{\Sigma}}_{GLS} + \boldsymbol{C}_{\delta} \otimes \boldsymbol{\Sigma}_\delta + \boldsymbol{I}_{NN} \otimes \boldsymbol{\Sigma}_\epsilon. \tag{A.40}$$

Note that $\boldsymbol{\Sigma}^{EE}$ is the covariance matrix for $\boldsymbol{y}^E(\boldsymbol{x})|\boldsymbol{\Phi}^*$ as previously mentioned in Eq. **??**. Refer to Table A.3 for dimensionality check for matrices in Eq. A.36.

Table A.3: Dimensionality check for Eq. A.36

| | |
|---|---|
| $\mathbb{E}[\boldsymbol{Y}^P \vert \boldsymbol{Y}^E]$ | $Sq \times 1$ |
| $\boldsymbol{m}^{**}(\boldsymbol{X}^P)$ | $Sq \times 1$ |
| $\boldsymbol{\Sigma}^{PE}$ | $Sq \times Nq$ |
| $\boldsymbol{\Sigma}^{EE}$ | $Nq \times Nq$ |
| $\boldsymbol{Y}^E$ | $Nq \times 1$ |
| $\boldsymbol{m}^{**}(\boldsymbol{X}^E)$ | $Nq \times 1$ |

# APPENDIX B

## MARKOV CHAIN MONTE CARLO ALGORITHMS

Monte Carlo methods are a broad class of computational algorithms that rely on repeated random sampling to provide approximate solutions to a variety of problems (physical or mathematical with or without any probabilistic structure) fishman2013monte. Several different algorithms have been developed to solve different problems, however in this dissertation we will only focus on those that are needed for general numerical estimation and Bayesian statistical inference.

The Monte Carlo (MC) principle is one of the most popular methods to numerically approximate probability distributions as well as integrals. The idea is based on the random drawing of N independent and identically distributed (i.i.d.) samples from a target distribution $p(\mathbf{x})$ defined on a $q$-dimensional space $\mathcal{X} \in \mathbb{R}^q$. The empirical distribution of $\left\{\mathbf{x}^{(1)}, \ldots, \mathbf{x}^{(N)}\right\}$ is known as a Monte Carlo approximation to $p(\mathbf{x})$, with

$$p_{\mathrm{MC}}(\mathbf{x}) = \frac{1}{N} \sum_{i=1}^{N} 1_{\left\{\mathbf{x}=\mathbf{x}^{(i)}\right\}}\left(\mathbf{x}^{(i)}\right) \tag{B.1}$$

where $1_{\left\{\mathbf{x}=\mathbf{x}^{(i)}\right\}}\left(\mathbf{x}^{(i)}\right)$ is the indicator function that equals to 1 if x = x(i) and 0 otherwise [123].

Additionally, MC can be used to approximate expectations (or integrals) with N i.i.d. random samples, since the Law of Large Numbers describe that for (almost) any function $g(\mathbf{x})$, we have that

$$\begin{aligned} \frac{1}{N} \sum_{i=1}^{N} g\left(\mathbf{x}^{(i)}\right) &\overset{N\to\infty}{\longrightarrow} \mathbb{E}\left[g(\mathbf{x})\right] \\ &\overset{N\to\infty}{\longrightarrow} \int_{\mathcal{X}} g(\mathbf{x})\, p(\mathbf{x})\, d\mathbf{x} \end{aligned}$$

since $\mathbb{E}\left[g(\mathbf{x})\right] = \int_{\mathcal{X}} g(\mathbf{x})\, p(\mathbf{x})\, d\mathbf{x}$, with $p(\mathbf{x})$ known or estimated from eq:MC-estimate-p(x) [124].

## B.1 Gibbs Sampler

In this widely used algorithm, the objective is to approximate multivariate probability distributions from which only the full conditional distributions for each element are known. In other words, for a random vector $\mathbf{x} = \{x_1, \ldots, x_q\}$, the interest is to approximate its joint probability distribution, $p(\mathbf{x}) = p(x_1, \ldots, x_q)$, with only knowledge and ability to sample from full conditional distributions of the form $p(x_k | x_1, \ldots, x_{k-1}, x_{k+1}, \ldots, x_q)\ \forall k \in \{1, \ldots, q\}$ Hoff2009.

## B.2 Metropolis-Hastings Algorithm

The Metropolis-Hastings (MH) algorithm is the most popular MCMC method. The objective of this algorithm is to approximate a joint probability distribution $p(\mathbf{x}) = p(x_1, \ldots, x_q)$ by indirect random samples when direct sampling is not feasible (which is usually the case for Bayesian posterior distributions). The main idea is to propose samples from a another distribution and then accept or reject them one element at a time.

Consequently, a proposal distribution needs to be defined for every component of the random vector **x**. These proposal distributions can be symmetric distributions, full conditional distributions, or something else entirely. The interested reader can refer to Hoff2009,andrieu2003introduction for more detailed explanations about this algorithm and the requirements that proposal distributions need to follow in order to ensure sequence with Markov Chain properties.

Here, the proposal distribution for the *j*th element of vector **x** and at the *i*th MH iteration is denoted as $J_j\left(x_j \middle| x_1^{(i)}, \ldots, x_{j-1}^{(i)}, x_j^{(i-1)}, x_{j+1}^{(i-1)}, \ldots, x_q^{(i-1)}\right)$.